

# University of St Andrews

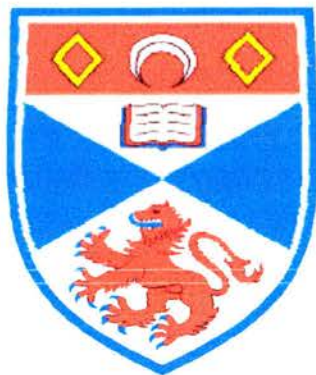


Full metadata for this thesis is available in  
St Andrews Research Repository  
at:

<http://research-repository.st-andrews.ac.uk/>

This thesis is protected by original copyright

# Structure and Magnetism in the Spinel $\text{ZnV}_2\text{O}_4$ and related studies



A thesis presented for examination for the title of Ph.D

By

Martin J. Smith

University of St. Andrews

September 2003



## 1.0 Declaration

I, Martin John Smith, hereby certify that this thesis, which is approximately 41 000 words in length, has been written by myself, that it is a record of work carried out by myself and that it has not been submitted in any previous application for a higher degree.

Date *25th January 2005* Signature of candidate

I was admitted as a research student in September 1999 and as a candidate for the degree of Doctor of Philosophy in September 2000, the higher study for which this is a record of, was carried out in the University of St. Andrews between 1999 and 2003.

Date *25th January 2005* Signature of candidate

I hereby certify that the candidate has fulfilled the conditions of the Resolution and Regulations appropriate for the degree of Doctor of Philosophy in the University of St. Andrews and that the candidate is qualified to submit this thesis in application for that degree.

Date *25th January 2005* Signature of Supervisor

In submitting this thesis to the University of St. Andrews I understand that I am giving permission for it to be made available for use in accordance with the regulations of the University Library for the time being, subject to any copyright vested in the work not being affected thereby. I understand that the title and abstract will be published, and that a copy of the work may be made and supplied to any bona fide library or research worker.

Date *25th January 2005* Signature of candidate

## 2.0 Abstract

This work explored magnetism and structure in  $\text{ZnV}_2\text{O}_4$  and a range of related vanadate spinels.

$\text{ZnV}_2\text{O}_4$  was studied in detail. Its peculiar magnetic properties and unusual structural deformation were considered both experimentally and theoretically. Extant published work on this material was contradicted in part and confirmed in others. Spin-orbit coupling effects were considered in detail for the first time in this material. These considerations resulted in a thesis which succeeds in offering a complete explanation of the observed structural and magnetic properties of the material. In the course of this, a previously unpredicted and unreported orbital ice-like state was proposed.

Compositions in the  $\text{Li}_x\text{Zn}_{(1-x)}\text{V}_2\text{O}_4$  solid solution series were synthesised and compared with the parent phase. Additionally, several members of the unreported  $\text{ZnGa}_x\text{V}_{(2-x)}\text{O}_4$  solid solution series were synthesised, lattice parameters were extracted from XRD and neutron diffraction and magnetic susceptibilities measured. These were used to assess the effect of compositional chemical and electronic disorder on the parent zinc vanadate spinel.

## 3.0 Contents

1.0	Declaration.....	1
2.0	Abstract.....	2
3.0	Contents.....	3
4.0	Thanks and Acknowledgements.....	6
5.0	General Introduction.....	7
6.0	Spinel ~ General.....	10
6.1	Vanadate Spinel.....	15
7.0	Theory.....	22
7.1	Structural.....	22
7.1.1	Crystal field theory – Structural implications.....	22
7.1.2	Spin orbit coupling – structural implications.....	24
7.2	Magnetism.....	28
7.2.1	General.....	28
7.2.2	Diamagnetism.....	32
7.2.3	Paramagnetism.....	32
7.2.4	Magnetic order.....	33
7.2.5	Ferromagnetism.....	36
7.2.6	Antiferromagnets.....	37
7.2.7	Spin Glasses.....	38
7.2.8	Geometric Frustration to Antiferromagnetic Ordering.....	40
8.0	Experimental Techniques.....	42
8.1	Synthesis.....	42
8.1.1	General.....	42
8.1.2	Temperature profiles of tube furnaces used.....	42
8.1.3	Precursors.....	43
8.1.4	Synthesis of Vanadate Spinel.....	46
8.2	Diffraction.....	47
8.2.1	General.....	47
8.2.2	Constant wavelength Techniques.....	57
8.2.3	White Beam techniques.....	58
8.3	Magnetic Measurements.....	62
8.3.1	dc Measurements.....	63

8.3.2	Corrections and conversions applied to data .....	67
8.4	$\mu$ SR .....	67
8.4.1	Muons .....	68
8.4.2	Muon Production .....	68
8.4.3	Muons in the sample .....	72
8.4.4	Positron emission & depolarisation .....	74
8.4.5	Modelling Muon Behaviour.....	80
8.4.6	Muons – a local probe.....	83
9.1	ZnV <sub>2</sub> O <sub>4</sub> Structural Studies .....	85
9.2	Ambient Structure.....	85
9.3	Structure at 4K.....	88
9.4	Transition .....	90
9.5	c < a Distortion – A Thesis .....	91
9.6	c < a Distortion – Evidence of dynamic effects? .....	95
9.7	Structure on Gallium / Lithium Doping.....	110
9.8	Structural: Discussion and Conclusions.....	110
10.0	ZnV <sub>2</sub> O <sub>4</sub> : Magnetism.....	115
10.2	Magnetic Measurements .....	118
10.3	Zero field cooled susceptibility.....	119
10.4	“Diamagnetic” Measurements .....	128
10.5	M/H sweeps .....	130
10.6	Field cooled Susceptibility in ZnV <sub>2</sub> O <sub>4</sub> .....	132
10.7	Remnant Magnetisation .....	137
10.8	Magnetic Neutron scattering.....	141
10.9	Zero Field-Cooled Magnetic Scattering.....	142
10.10	ZnV <sub>2</sub> O <sub>4</sub> 4K magnetic structure .....	146
10.11	Thesis expanded.....	150
10.12	Field-Cooled Magnetic scattering .....	154
10.13	MuSR .....	158
10.14	Fitting ZnV <sub>2</sub> O <sub>4</sub> MuSR Data .....	162
11.0	Doped Vanadate spinels - Introduction.....	169
11.1	Experimental.....	171
11.2	XRD studies at Ambient Temperature.....	172
11.3	Magnetic susceptibility data .....	175
11.4	Neutron Scattering .....	180

11.5	$\mu$ SR doped samples.....	183
12	Zinc vanadate spinel: Conclusions.....	190

## 4.0 Thanks and Acknowledgements

During the course of this work I have met, and received help from, a great many people. Doubtless, I will have inadvertently omitted some of those from the following list. To those, I apologise ~ your omission was not intentional.

Locally:

School of Chemistry: Prof. J.T.S. Irvine, for too many things to recount.

Dr. J. Tolchard (now at Surrey), Dr. J. Bradley, Dr. J. Dobson, Dr. P. Connor, Dr. F. Belliard, Dr. S. Tiwaryy, Dr. W. Mackrodt, Mr. D. Middlemass, R. Cathcart.

School of Physics : Prof. S. Lee, Prof. R. Cywinski (now at Leeds), Dr. P. Manuel (now at ISIS), Dr. J. Armitage, Dr. D. Tunstall.

Dr. A. Wills , ILL, Grenoble, France/ RI, UCL, London.

At ISIS, RAL : Dr. R. Smith, Dr. R. Ibberson, Dr. K. Andersen, Dr. A Hillier, Dr. F. Pratt.

At ILL, France: Dr. R Stewart, Dr. Amir Murani.

Elsewhere: Prof. J. B. Goodenough (Austin, Texas), Dr. R. Gover and Prof. J. Evans (Chem., Durham), Prof. A. Harrison (Chem., Edin.), Prof. S. Blundell (Phys., Oxford)

I would also thank, in general, other members of the School of Chemistry at St-Andrews. RSC and Salter's who funded many of the school children's workshops and activities, which I enjoyed being involved with. EPSRC / IOP / BCA / ISIS who funded/organised training courses on superconductivity, theory of condensed matter physics, low temperature experimental techniques, magnetic structure and refinement workshop and the ISIS neutron training course which I attended during the course of this work.

EPSRC and The University of St. Andrews for funding this work and ESF/OSSEP in the dying days.

Kirriemuir Angling Club and Newton Country Sports for providing an occasional escape to tranquillity and even the odd fish for the pot!

My family. If they weren't, I doubt they'd have put up with me.

## 5.0 General Introduction

It is a relatively simple matter to classify historical ages of human development in terms of the materials used by people during those times. Stone age, Bronze Age and Iron Age are familiar terms that describe themselves satisfactorily. One might then note that underpinning much of the industrial revolution were newly discovered techniques of extracting, forming and working metals on a previously unprecedented scale – without which the railways and machinery that were the driving force behind that age would not have been possible.

In the mid 1800's we see the start of the electrical materials age, in which relatively simple devices such as lighting systems and telegraphy utilise the ability of conductive materials to move both power and information around. One hundred years later and we are very much in the electronic (rather than electrical) materials age – semi-conducting devices proliferate, logical processing of binary instructions and information become common-place - development tends towards making these devices increasingly powerful and sees them become progressively smaller. Some understanding of how electrons behave in materials has allowed us to develop all of these electronic devices. We have also come to understand how many of the features that give rise to useful electronic properties also give rise to a material's optical and other physical properties.

In the 1980s we begin to see the widespread use of optical fibres to carry information – much in the same way that electrically conductive wires began to be used in telephony just over hundred years earlier. At around the time of writing this, it would seem that we are approaching a fundamental limit to what we can do with

conventional electronic devices – resistive heat generated in the now microscopic processing devices is a major obstacle to further miniaturisation. Further, components are beginning to approach the size where quantum uncertainty becomes significant and a problem. One can perhaps foresee the future development of optical devices, which generate no heat, ultimately replacing the current electronic ones. Nevertheless, in the interim there is still much technological potential in making improvements to the electrical materials currently used. Additionally, there are myriad as yet unknown materials whose properties can only be guessed at.

Of great importance amongst the electronic materials have been those that exhibit magnetic properties. Discovering that magnetism has an inherent directionality, it was recognised that if an array of magnetic particles could have their individual magnetic directions patterned, then such an array could be used for binary data storage. Earlier means of storing binary information had involved punched cards or tapes. These were single use media however, and hence wasteful as well as bulky. The ability to switch the direction of a material's magnetic properties would allow data stored in a magnetic array to be overwritten at will. Such magnetic data storage would be one of the pivotal technologies in the development of smaller computing and other portable media devices. Whilst this would give a great financial impetus to the understanding of magnetism for practical applications, this would also necessarily feed into the area of research into magnetism in general.

It is without doubt that the electronic age, beginning towards the middle of the 20<sup>th</sup> century, has heralded amongst the most significant and fastest period of development in human history. The number of individuals contributing to this progress is enormous, however the group of Shockley, Bardeen and Brittain, who are regarded as

the inventors of the transistor should probably be singled out for particular note. Their invention was no fortuitous discovery however. It was a direct descendent of earlier work carried out to investigate how electrons behave in materials.

Although much is now known in this subject area, there is far more which is either poorly understood, or just not understood at all. At a time when there are huge research efforts in trying to unravel the immense complexities of human genetics, we are forced to admit that we cannot even infallibly predict, *ab initio*, the exact physical, electrical and magnetic properties of many *simple* binary metal oxide materials.

With the above thoughts in mind, recognising the impact an understanding of how electrons behave in materials has had on recent, current and foreseeable technologies, it is surely then a simple task to justify further basic research in this area.

## 6.0 Spinel ~ General

The spinel gemstone ( $\text{MgAl}_2\text{O}_4$ ) gives its name to a range of minerals sharing the same chemical structure.

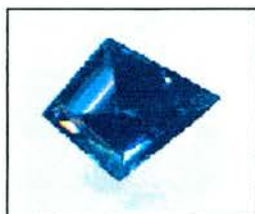


**Figure 6. 1 (left) shows a blue spinel gemstone ( $\text{MgAl}_2\text{O}_4$ ). Such stones are most commonly red and are commonly mistaken for rubies, but are also found in many colours, e.g. rose, violet, blue, yellow, orange..., the colour arises from the presence of particular trace metallic impurities.**

The table below gives a list of some natural and man-made spinels along with some of their more notable properties. A quick survey of the table notes that in most cases the property mentioned is in some way electrical (or magnetic).

The general formula for spinels is  $\text{XY}_2\text{O}_4$ , and they come in three main varieties. In the first type, both X and Y are the same cation, examples being  $\text{Fe}_3\text{S}_4$  and  $\text{Fe}_3\text{O}_4$ . A and B designations are used to describe two different the positions the cation(s) can occupy in the crystallographic structure. The A-sites correspond to tetrahedral holes and the B-sites to octahedral holes in a closed packed array of anions. The spinel structure has twice the number of occupied octahedral holes as it does tetrahedral. In a *normal spinel*, the A-sites are occupied by one cation type and the B-sites by another. An *inverse spinel* shows a mixture of both cations on the B-site and one type on the A. A completely inverse spinel would have a 50/50 mixture of cation types on the B-site, often written as  $\text{A}(\text{AB})_2\text{O}_4$ .

The anion is most commonly oxygen, however a range of sulphide and fluoride spinels are also known. Less commonly perhaps, a few selenides have been reported.<sup>1</sup> The sulphides (and to a greater degree selenides), being larger anions

should accommodate larger cations in the holes in their respective close packed arrays. Partial substitution of the oxygen anions using chlorine or fluorine ions has been carried out in a number of cases.<sup>2</sup>

$\text{MgAl}_2\text{O}_4$	The original spinel, base for natural gemstones.
$\text{ZnAl}_2\text{O}_4$	Gahnite, a transparent diamagnetic spinel.
$\text{Fe}_{(1-x)}\text{Cu}_x\text{Cr}_2\text{S}_4^*$	A chalcogenide with colossal magnetoresistive properties.
$\text{CuCo}_2\text{S}_4$	Carrollite, a natural metallic spinel.
$\text{Fe}_2\text{TiO}_4$	Ulvöspinel, with giant magnetoresistive properties .
$\text{ZnFe}_2\text{O}_4$	Franklinite, a paramagnetic ferrite.
$\Gamma\text{-Fe}_2\text{O}_3$	Maghemite, a natural material for magnetic recording.
$\text{Fe}_3\text{O}_4$	Magnetite, the ancient navigator's lodestone.
$\text{Fe}_3\text{S}_4$	Greigite, a ferrimagnetic semimetal.
$\text{FeCr}_2\text{O}_4$	Chromite, the chrome ore of Rhodesia.
$\text{Mn}_3\text{O}_4$	Hausmannite, a natural tetragonal spinel.
$\text{Mg}_2\text{SiO}_4$	The high-pressure spinel polymorph of Forsterite (olivine), thought
$\text{NiFe}_2\text{O}_4$	Trevorite, a ferrimagnetic semiconductor.
$\text{LiV}_2\text{O}_4^*$	A heavy fermion transition metal oxide.

**Table 6. 1** mostly taken from N. W. Grimes, "The Spinel: Versatile Materials",<sup>3</sup> except for \*'d entries which are from more recent work.

There are many prescriptions for predicting cation distribution in spinels, but sufficient exceptions to these *rules* that it is wise to treat such prediction with some caution. Even where thermodynamics would predict that a given distribution is

preferable, reaction kinetics in the spinel synthesis often prevent the ideal distribution being realised. Typically however, crystal field stabilisation energies play a critical role in determining site occupancies.

Structurally, a typical oxide spinel has a cubic unit cell, with a lattice parameter of around 8-9Å. The figure below shows a representation of the normal spinel structure

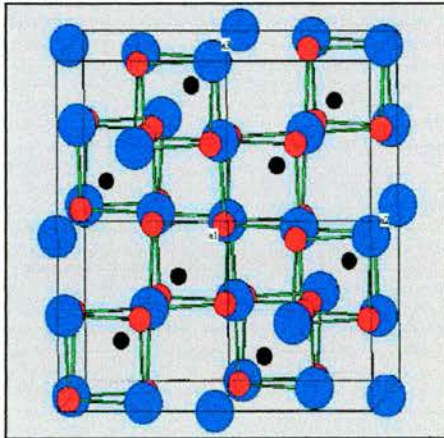


Figure 6. 2, the black atoms represent the A-site cations, the blue atoms the B-site cations and the red atoms form the closed packed anion sub-lattice. Green bonds indicate the B-site cation – anion coordination. The atom sizes are of no significance in this diagram.

Some spinels are distorted off the ideal cubic structure and many tetragonal spinel variants are known. Jahn-Teller effects can occur in suitable cations giving tetragonal spinel variants, well-known examples are the manganate spinels.

From the cubic spinel's unit cell ( $a' \times a' \times a'$ ), a  $\sqrt{2}a' \times \sqrt{2}a' \times a'$  sub unit is extracted which becomes an  $a'' \times a'' \times c$  tetragonal unit cell (where  $a'' = \sqrt{2}a'$  and  $c = a'$ ).

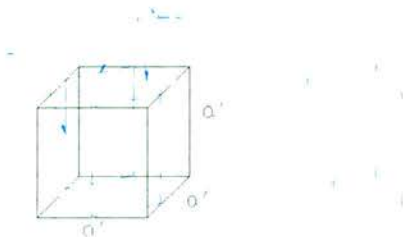


Figure 6. 3 shows the extraction of the tetragonal spinel unit cell from its cubic counterpart.

Elongation, or compression, of this sub-cell along the  $c$  axis gives the crystallographic unit cell for the common tetragonal spinels. The cubic spinel takes the space group  $Fd-3m$  (#227) whilst the tetragonal variant takes space group  $I_{41}/amd$  (#141). Where ordering of mixed B-site cations occurs, the crystallography can become much more complex. Distortion is usually  $c > a$ , but in rare instances including  $ZnV_2O_4$ , a  $c < a$  variant is observed.<sup>4</sup>

Table 6.1 above gives some idea of the wide range of properties that spinels can show. Perhaps the most important spinel historically was magnetite ( $Fe_3O_4$ ), the ancient navigator's lodestone. Not recorded in Europe until c.12<sup>th</sup> century, the first practical use of magnetism (and very probably magnetite) in the form of the compass was described by the Chinese scientist and scholar Shen Kua around 1086.<sup>5</sup>

The electrical and / or magnetic properties of spinels arise from the presence of unpaired electrons on one or both of the cations. As described above, these *electric* cations are typically first row transition elements. Other elements such as lithium, zinc, magnesium, aluminium and silicon are common in such spinels, however these tend to influence the electrical / magnetic properties of the materials by modifying / controlling the oxidation state of other transition metal cations rather than being directly involved. Where the anions and A-site cations have no electrical or magnetic properties of their own and the B-sites are occupied by suitable cations the nature of the materials electrical and magnetic properties are determined solely by the B-site sub-lattice occupants.

In such a situation, which is met by all of the spinels examined in this work, direct overlap, or lack thereof, of the B-site cation d-orbitals becomes important – as this determines whether a band model is valid or whether we are dealing with completely

localised electrons.

Describing the above in this introductory section is to emphasise the importance of the structural arrangement of the B-site cation sub-lattice ~ aspects like thermal expansion/contraction will obviously influence the degree of overlap as will structural distortions. The figure below looks at the B-site cation sub-lattice in isolation for the other species :

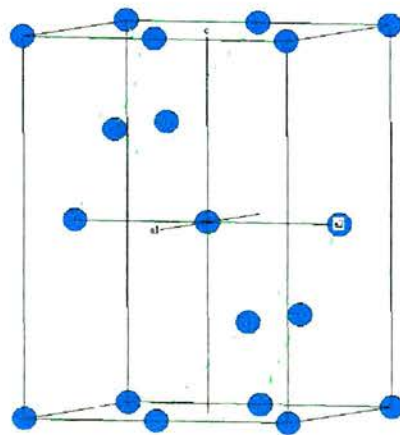


**Figure 6. 4 shows the spinel B-site sub-lattice ~ in this case from a tetragonal sub-cell extracted from the cubic form.**

B-site cations are seen to form a three dimensional network of corner sharing tetrahedra. The edges of these tetrahedra form the shortest B-site m-m distances. Although it is not seen in figure 6.4, no other species lie along these tetrahedral edges and so orbitals pointing in this direction have the potential for direct overlap. The triangular nature of this B-site sub-lattice and the m-m distances will become important latter in this work.

As will be described in more detail later, this beautiful tetrahedral B-site sub-lattice cannot readily support antiferromagnetic ordering – the geometry of this lattice prohibits simple alternating collinear spin arrangements. Where magnetic interactions

between spinel B-site cations are predominantly antiferromagnetic a range of exotic magnetic phenomena may be found.

To provide a succinct summary of spinels is a difficult task due to their wide-ranging properties, compositional variety and abundance.

## **6.1 Vanadate Spinel**

A number of vanadate spinels are known. Vanadium usually occupies the B-site and is not commonly found on the A-site. This is due to the increased crystal field stabilisation energy experienced by the V(III) cation in octahedral coordination relative to tetrahedral.

A large number of mixed B-site spinels exist, where the element can be doped in place of other 1<sup>st</sup> row transition metals that form spinels, such as Mn, Fe, Co and Ni. (Probably scandium also, but no reports of Sc/V spinels were found).<sup>6,7</sup>

Occupy the B-site with vanadium only however, and relatively few spinels are known. Those that are known, include a solid solution series from  $\text{LiV}_2\text{O}_4$  to  $\text{ZnV}_2\text{O}_4$  and  $\text{AlV}_2\text{O}_4$ . The latter is an interesting material, in which the vanadium cations are in a mixed (II)/(III) oxidation state and have been reported to show charge ordering – a cation in an oxidation state of (II) on a spinel B-site is unusual in itself.<sup>8</sup> Best known of these vanadate spinels is  $\text{LiV}_2\text{O}_4$ . It's fame stemming from the recent discovery that it shows low temperature behaviour akin to that of the f-series heavy fermion materials it being the only material not containing lanthanide, or actinide, element(s) to do so.<sup>9</sup>

Work in the late 1960's and early 1970's described  $\text{ZnV}_2\text{O}_4$  as a Mott insulator, undergoing a metal insulator transition which coincided with the onset of long range antiferromagnetic order.<sup>10,11</sup> The magnetic susceptibility data obtained on this material was however described as being anomalous. It was thought that the material might show a transition from ferromagnetic to antiferromagnetic states. No conclusive evidence was found for such a transition, however the large field cooled magnetic susceptibility looked to have more in common with a ferromagnet than an antiferromagnet, possibly the applied field was flipping an antiferromagnetic phase into a an FM one in a spin flop transition.<sup>12</sup> However this effect is observed even with small applied fields, suggesting that were the material to undergo such a transition, then the energy difference between the two states might be very small, it is metamagnetic or possibly close to a quantum critical point.<sup>13</sup>

In 1973, a neutron scattering experiment on  $\text{ZnV}_2\text{O}_4$  showed the presence of additional crystallographic Bragg peaks at very low temperature.<sup>11</sup> Those peaks were attributed to the chemical structure's symmetry being broken by an antiferromagnetic superstructure. As can be seen in the plot taken from Niziol's paper below (figure 6.5) however, the number of data points above background corresponding to these magnetic Bragg peaks is few, and one might wonder if they are in fact real.

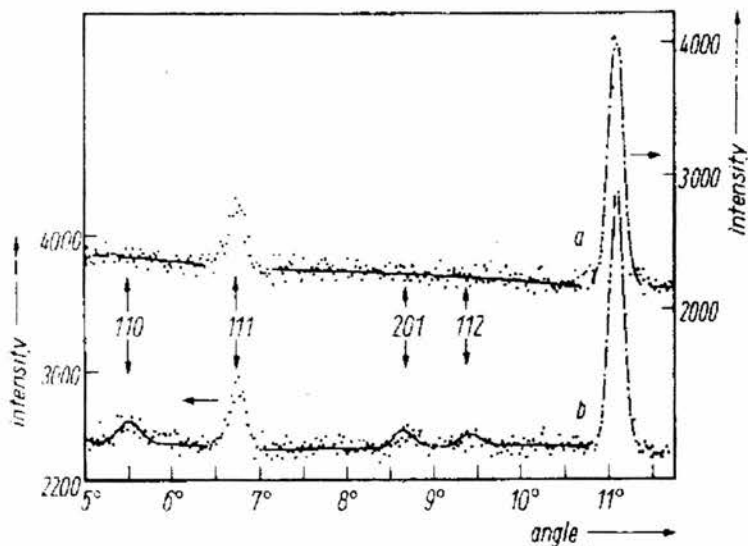


Figure 6. 5 shows the appearance of antiferromagnetic Bragg peaks in  $\text{ZnV}_2\text{O}_4$  at low temperature? (Taken from Niziol).

It was then taken that this material was an antiferromagnet at low temperatures and very little work was done on it until 1997. At this time, Ueda *et. al* set out to determine the magnetic phase diagram for the solid solution series  $\text{Li}_{(x)}\text{Zn}_{(1-x)}(\text{V}_2\text{O}_4)$ .<sup>14</sup> This work stimulated a great deal of interest in the compounds at and close to the lithium end of the series, however, relatively little interest was paid to the zinc end. The majority of compositions in this series showed paramagnetic to spin-glass transitions at low temperatures. The zinc end was *known* to give antiferromagnets, hence the apparent antiferromagnetic transition was re-observed in susceptibility measurements and reported along with other members of the series. At the lithium end, no spin-glass transitions were observed, and the material was seen to remain, broadly speaking, paramagnetic down to the lowest temperatures measured.

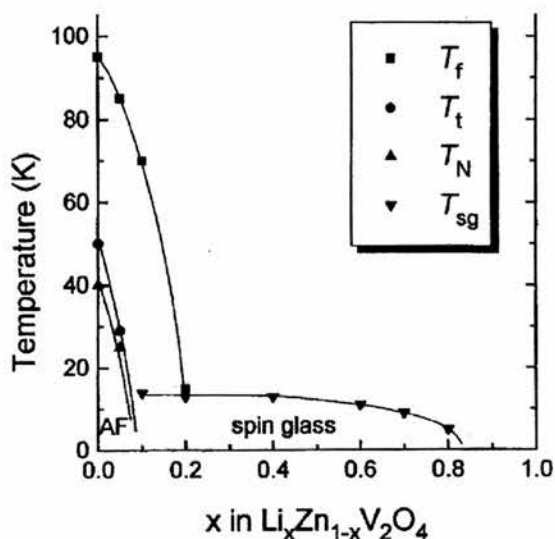
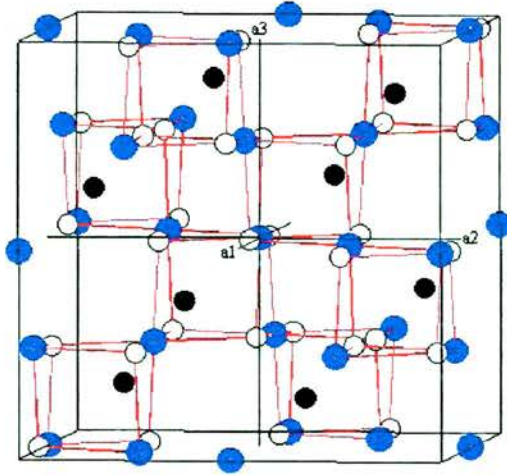


Figure 6. 6 shows the magnetic phase diagram produced and published by Ueda et al. in 1997.

Perhaps ironically, interest in the discovery of the first non f-series heavy fermion-like material has directed attention away from the zinc end member of this solid solution series. Whilst the properties of  $\text{LiV}_2\text{O}_4$  are interesting, finally they are explicable in terms of a combination of well-established phenomena. Conversely, the “anomalous” behaviour  $\text{ZnV}_2\text{O}_4$  would prove very difficult to explain.

Yamashita later published a theoretical paper describing the observed structural transition as being “spin-driven”.<sup>15</sup> This view will be challenged later.

At room temperature the entire  $\text{Li}_{(x)}\text{Zn}_{(1-x)}(\text{V}_2\text{O}_4)$  series adopts the cubic spinel structure, spacegroup - Fd-3m (#227), lattice parameters ranging from  $a = 8.238\text{\AA}$  for  $\text{Li} = 1$ <sup>16</sup> to  $8.406\text{\AA}$  at  $\text{Zn} = 1$  (at ambient temperature).<sup>17</sup> Figure 6.7 below shows the structure of a standard cubic normal spinel. Using  $\text{ZnV}_2\text{O}_4$  as an example, in the figure the black atoms represent zinc, the A-site cation, the blue atoms vanadium ~ B-site cations and the white the oxygen sub-lattice.



**Figure 6. 7 shows the cubic spinel structure, black points indicate A-site cations, blue – B-site cations while the anions are shown as white points.**

Notice from the figure above that the structure appears visually to be slightly off-set to the ideal cubic. This appearance is due to a slight tilting of the V-O octahedra relative to each other, the oxygen ions sitting a little off their ideal  $(1/4, 1/4, 1/4)$  sites. The overall symmetry of the structure is cubic. However, despite this octahedral tilting, all atoms of one type remain crystallographically equivalent to each other, all V-O distances and angles are equal as are V-V distances and angles.

Each cation has 3 nearest neighbour cations to either side of it, which results in a very subtle trigonal crystal field splitting effect on the vanadium  $t_{2g}$  orbitals – in addition to the octahedral splitting due to the anions.<sup>18</sup> At ambient temperature this trigonal splitting is probably trivial, and no effect is seen on the cubic structure.

The main object of interest in these magnetic spinels is the B-site sub-lattice, which contains the magnetic cations. This sub-lattice is shown in figure 6.8 below.

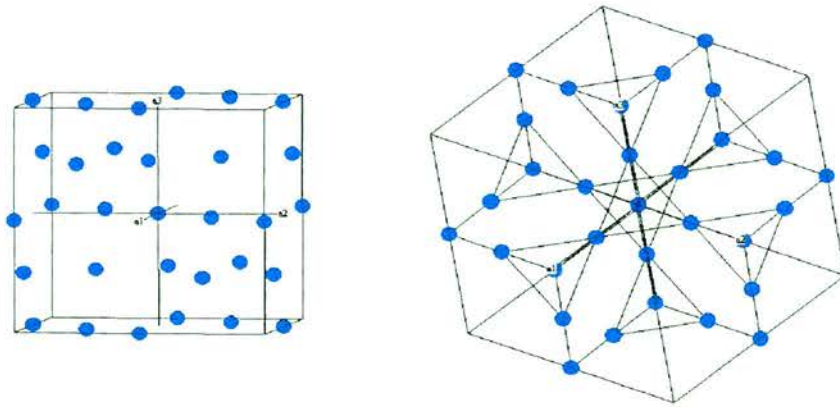


**Figure 6. 8 shows the B-site sub-lattice in isolation, to the left the cations as they appear in a straightforward cubic representation, to the right nearest neighbour cations are joined by “a bond” and the cube is viewed down a 1,1,1 vector to highlight the tetrahedral nature of the B-site sub-lattice.**

As above, with a *bond* drawn from each B-site cation to its nearest neighbours and viewed down a real space 1,1,1 vector, the triangular nature of coordination on the B-site sub-lattice becomes apparent, several tetrahedra are visible in this view.

This is the magnetic sub-lattice in the vanadate spinels. Formed entirely from equilateral triangles, it presents what is probably the ultimate in geometrically frustrated antiferromagnetic lattices. The frustration is fully three dimensional unlike that of the archetypal Kagome lattice found in materials such as the jarosites<sup>19</sup> and spinel derived layered<sup>20</sup> materials.

From about  $Zn = 0.85$  to  $Zn = 1$ , a slight tetragonal distortion is observed at low temperature.<sup>21</sup> This distortion in these vanadates was found in this work to take the  $I4_1/amd$  (#141) space group, similar to that observed in well known Jahn-Teller distorted spinels such as  $LiMn_2O_4$ .<sup>22</sup> In this case however, the direction of the distortion is reversed from that normally seen,  $c < a$  rather than the expected  $c > a$ . This feature alone is extremely interesting and worthy of study in its own right, it is

discussed at length presently. Figure 6.3 above showed the extraction of the tetragonal variant from the cubic unit cell.

In addition to the gross J-T distortions such as those observed in  $3d^4$  manganates or  $3d^9$  cuprates, where the B-site cation has relatively few electrons, e.g.,  $3d^1$  or  $3d^2$ , one might expect dynamic J-T effects. This phenomenon is described in more detail in section 7 below. Amounting to rapid B-O bond length fluctuations these dynamic effects are not visible on the timescale of a diffraction experiment, however as the temperature is reduced these may, at some point, freeze out to give a similar cooperative distortion. Given that the difference in stabilisation energy between the distortion in different directions is very small, the next nearest neighbour trigonal CF effects may become significant in determining the direction of the cooperative distortion.

## 7.0 Theory

### 7.1 Structural

#### 7.1.1 Crystal field theory – Structural implications

Crystal Field Theory is a specialised case of the more general Ligand Field Theory. Bethe (in 1929) considered this initially in the case of the NaCl structure, attempting to ascertain the effect of neighbouring atoms on orbital energies. The ligand, or crystal, field at any point in space is considered to be the sum of electrostatic potentials acting on that point in space. The rearrangement of electrons in orbitals for some central ion, relative to the directions of its neighbours, was seen in some cases to be capable of reducing the total electronic repulsion and hence energy in the structure. Thus, from the Second Law, certain structures are of lower energy and are hence preferred to others. The electronic structure of the central ion is thus important in determining structure; but also, conversely, knowing the crystal structure gives us some insight into the electronic structure of that ion. Crystal field stabilisation of structure is thought to account for as much as 10% of the total lattice energy in some cases. This theory is successful in explaining many molecular shapes and merged well with subsequent molecular orbital theory; the combination of which provides much of our understanding of structures. Under normal circumstances only nearest neighbour ligands are considered to have a significant effect on the orbitals of the central ion.

With respect to the  $\text{ZnV}_2\text{O}_4$  spinel discussed in this work, it is seen that the effectively spherical  $3d^{10}$  Zn(II) cation cannot benefit from crystal field stabilisation.

The V(III) cation however, is of different energies in tetrahedral and octahedral coordination. The crystal field stabilisation of the V(III) cation is of the order of one  $Dq$  unit greater in octahedral coordination than in tetrahedral, thus octahedral sites is preferred. As a result, the V(III) cations are found only on the B-sites and the resultant  $ZnV_2O_4$  spinel is completely normal. Figgis notes that cation distribution in 1<sup>st</sup> row transition metal spinels cannot be completely explained by cation charge or size considerations.<sup>23</sup>

In this work we are primarily interested in the octahedrally co-ordinated V(III)  $3d^2$  ion. The basics of octahedral coordination and the relevant ligand or crystal fields are standard in basic textbooks; however, the  $3d^2$  cation in this case has some interesting peculiarities, requiring a more detailed consideration.

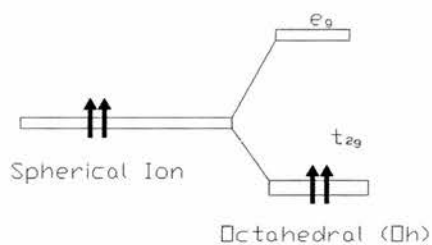


**Figure 7. 1 shows the splitting of the d-orbital manifold energy into  $e_g$  and  $t_{2g}$  components by regular octahedral 6-fold coordination. Please note that this and other energy splitting diagrams are NOT drawn to any particular scale.**

Once in octahedral 6-fold coordination, the d-orbital manifold splits into  $e_g$  and  $t_{2g}$  levels, the 2 d-electrons occupying the lower energy  $t_{2g}$  set. This is our starting place. We note that the 2 d-electrons occupy 3 orbitals and are therefore degenerate in energy. The Jahn-Teller theorem can be stated in the form: *A non-linear molecule possessing degenerate electrons is unstable with respect to geometric distortion; this ion is liable to such an effect.*<sup>24</sup> Trigonal or tetragonal distortions are the most likely; it is found experimentally that a low temperature tetragonal distortion is observed in

ZnV<sub>2</sub>O<sub>4</sub>. There are two possible tetragonal variants, one where  $c > a$  and the converse where  $c < a$ .

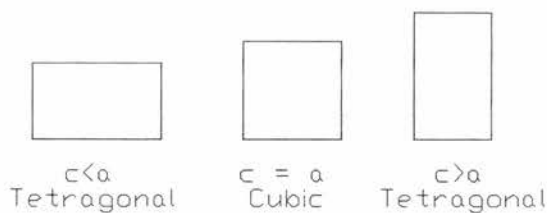


Figure 7.2 Shows the two possible distortions from cubic – note the  $c < a$  looks like the  $c > a$  through 90° here; however for the six ligands, the  $c < a$  distortion results in 4 long bonds and 2 short, while the  $c > a$  yields 2 long bonds and 4 short.

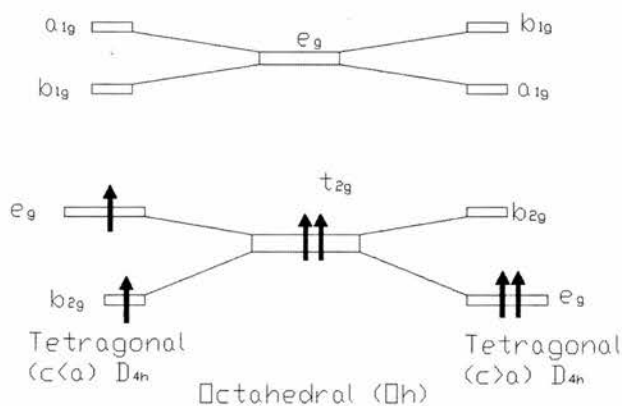


Figure 7.3 shows the splitting of the orbital energy levels for the  $c < a$  and  $c > a$  tetragonal distortions illustrated in figure 7.2.

Intuitively, from the above energy splitting diagrams one would think that the  $c > a$  variant would be observed experimentally, as this appears to offer a lower total energy. In the spinel ZnV<sub>2</sub>O<sub>4</sub> however, it is found that the  $c < a$  variant is preferred. In general this  $c < a$  distortion is unusual and is worthy of additional study.

### 7.1.2 Spin orbit coupling – structural implications

Spin-orbit (L-S) coupling is often described as being completely quenched for 1<sup>st</sup> row transition metal cations. More detailed consideration finds that this is not always so; and is not so in the case of the octahedral 3d<sup>2</sup> cation.<sup>25,26</sup> The 2 d-electron orbitals point into *free* space, away from the electronic potentials of the surrounding ions,

they are thus affected only minimally by these ligand fields. Degeneracy in the  $t_{2g}$  orbitals allows for L-S coupling and hence some L-S effect is anticipated.

If the cubic form is L-S coupled, then the 2 d-electrons are not actually degenerate. The coupling splits the  $t_{2g}$  level threefold. In the absence of that degeneracy a Jahn-Teller type distortion is NOT expected.

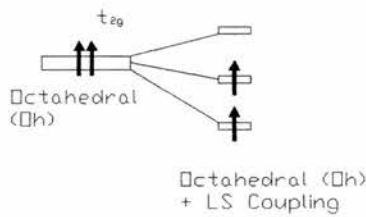


Figure 7. 4 shows the octahedral  $t_{2g}$  energy level split 3 fold by spin-orbit coupling.

Detailed orbital energy splitting diagrams are available for cubic, tetragonal and cubic L-S coupled  $3d^2$  cations.<sup>27,28</sup> It is seen that the observed tetragonally distorted form,  $c < a$  has a single electron occupying an orbital with  $e_g$  symmetry, *prima facie* at least, this electron is still degenerate; so has the potential to retain some element of L-S coupling. A published splitting diagram including both the distortion and L-S coupling could not be found.

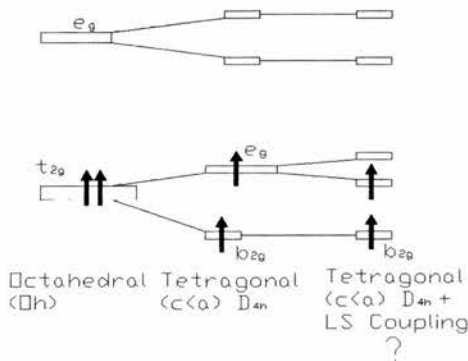


Figure 7. 5 shows a possible energy splitting diagram for the  $c < a$  tetragonal distortion + LS coupling.

If the observed distorted form is not L-S coupled, then the remaining degeneracy may render the tetragonally distorted species liable to yet further distortion (as per the Jahn-Teller theorem). Such a second distortion is not observed experimentally; however, it is recognised that were one to exist, it might simply be too small to observe.

(N.B. The energy stabilisation involved in spin-orbit coupling is termed  $V_{LS}$ , whilst that for the Jahn-Teller stabilisation energy is  $V_t$ .)

That this direction of distortion is also observed in  $\text{CrO}_2$  and  $\text{YVO}_3$ , both of which have the same  $d^2$  cation in octahedral coordination suggests that this type of distortion may be common to the  $3d^2$  cation generally.<sup>29,30</sup>

Figgis notes; “spin-orbit coupling may stabilise a symmetric configuration otherwise expected to distort”, Goodenough makes similar comment (see below).<sup>31,32</sup> Whether or not this symmetric stabilisation occurs will depend on the strength of the relevant potentials, e.g. where  $V_{LS} > V_{CF}$  then the distortion is not expected, and the converse.

As per the non-quenching of L-S coupling argument, the pair of electrons occupying  $t_{2g}$  orbitals are relatively unaffected by the neighbouring ligand fields and thus any distortion will offer little additional crystal field stabilisation. Consequently, the magnitude of such a tetragonal distortion is likely to be small. In the case of  $\text{ZnV}_2\text{O}_4$ , the observed distortion is very slight; implying that relatively small energies separate the cubic and distorted forms. This raises the possibility of another phenomenon, namely the Dynamic Jahn-Teller effect.

Goodenough makes several observations about Jahn-Teller, and Jahn-Teller-like, distortions and the role of spin-orbital coupling in the context of magnetic materials.<sup>33</sup>

These observations may be of great importance in considering  $\text{ZnV}_2\text{O}_4$  and are repeated here for that reason. All notes, as adapted, refer to a cation initially in ideal octahedral coordination. These notes are summarised (almost verbatim in places) below:

Where  $V_{\text{LS}} > V_{\text{t}}$ , the spin-orbit effects may prevent Jahn-Teller distortion. e.g., Jahn-Teller distortion can only be predicted unambiguously if crystal field effects are certainly stronger than the L-S coupling, for example in  $d^4$  and  $d^9$  cations.

Collinear spin order **below** an ordering temperature may also induce a crystal distortion. However this distortion will be in the opposite sense to that predicted on Jahn-Teller arguments. This magnetic distortion requires that L is not completely quenched as it would be in a normal Jahn-Teller effect. This is not a cooperative Jahn-Teller distortion.

A  $d^4$  or  $d^9$  cation can acquire equal stabilisation by either the ( $c > a$ ) or ( $c < a$ ) Jahn-Teller distortion from cubic symmetry. In such a case, the system may show a resonance behaviour between both forms, a coupling between lattice vibrations and low frequency electronic motion. This is termed the dynamic Jahn-Teller effect.

Magnetic phenomena other than long range ordering may be present, which render the  $V_{\text{LS}}$  the dominant factor, yielding the  $c < a$  variant in slightly stabilising one of the resonant forms over another. Additionally, other subtle effects such as next-nearest neighbour crystal field splitting also become more important, these may result in a preferred static distortion at low temperatures. On freezing out, the distortion becomes cooperative.]

Jahn-Teller effects are due only to lattice-orbital interactions and are independent of

spin and hence spin ordering at some ordering temperature. This can be used to distinguish between cooperative Jahn-Teller distortions and magnetic lattice distortions that occur on or below a spin ordering transition.

From the literature the  $3d^2$  cation is found to behave counter-intuitively. Some indications of similar counter-intuitive behaviour are also found for the  $3d^7$  cation.<sup>34</sup>

A pair of d-electrons occupying the  $t_{2g}$  orbital set shows a marked tendency to produce the two short, four long bonds arrangement. Primarily the evidence for this is found in the  $V^{3+}$  cation, however other examples include  $Cr^{4+}$  ( $CrO_2$ ) and  $Co^{2+}$  ( $CoO$ ).<sup>35,36</sup>

From this and the latter sections it is seen that several factors come into play when considering the structure of the solid state V(III) cation. The energy changes involved in these factors are likely to be small. Determining why the structure distorts as it does is not straightforward. Competition between the competing factors seems possible if not probable. As dynamic effects (Dynamic Jahn Teller & thermal contraction/expansion marginally altering crystal field strengths) are usually temperature related, temperature changes may alter the predominant effect and give rise to observable structural changes.

## **7.2 Magnetism**

### **7.2.1 General**

Magnetism can be defined as the relativistic corrections to the electrical fields generated by the motion of charged particles (electrons).<sup>37</sup> In condensed matter, magnetism can be exhibited in several ways. In general however its relativistic nature

implies that it is inextricably related to the motion of the charged particles that comprise that matter. From the superposition principle, magnetic properties due to individual particles of opposing motion will be of an opposite sense and cancel each other – completely if their magnitudes are also equal.

Two main forms of motion among these particles give them their magnetic properties. Firstly, the ordinary form of translational motion we are familiar with (digressing from the quantum nature of these particles for simplicity), linear motion or the orbital motion of an electron perhaps. Secondly, a less intuitive form of motion is termed spin, the physical origins of this motion are unclear; formally, it is perhaps better described as the *intrinsic angular momentum* of the particle. Measurement shows that this spin property is of fixed magnitude for all particles of a given type, thus the term *intrinsic* seems fitting. Otherwise, one might loosely envisage the particle literally spinning about some internal axis but there is no experimental means of testing this view.

We expect that both nucleons and electrons may show magnetic properties that may or may not be cancelled on a time-averaged basis. Neutrons and protons are not fundamental particles, the quarks of which they are composed are charged. A certain combination of quarks can yield the neutron of zero net charge, however in this combination, the quarks' magnetic contributions to the neutron are not cancelled thus the uncharged neutron retains magnetic properties. This work makes little reference to nuclear magnetism and this is left at the extent of noting that nuclear magnetism originates from the net spin of the nuclei.

Electron magnetism dominates this work and is most familiar to us on a macroscopic scale. The induced linear motion of electrons in current carrying wires leads a well-

known means of generating magnetic fields, however this is not relevant in this work. The other motion of interest is mainly the orbital and spin motion. Some different types of electron magnetism are broken into subsections below, however some discussion of the localisation/de-localisation of electrons is given first.

From the notions of basic band theory as referenced in any number of introductory texts, it would appear that any extended molecular orbital that is neither full nor empty should give electrical conductivity to a material. In practise this is not so. The first row transition metal monoxides, where only TiO and VO are metallic, illustrate this nicely. Although delocalisation (and hence a conductive state) may often offer a reduction in the total free energy of a system and is thus expected, other factors may offer greater stabilisation and prevent this state arising.

Where orbital overlap is restricted due to the distance and / or geometry between adjacent cations, the resultant band(s) will be narrow in energy range. This is expected where the orbitals are highly directional; d-orbitals as opposed to isotropic s-orbitals for example. The necessary physical proximity of electrons to each in such a narrow band results in significant electron-electron repulsion effects. This can cause the delocalised state to be higher in overall energy than the localised one. The d-electrons remain on their respective cation sites and can be thought of as occupying atomic orbitals rather than an extended molecular orbital. These inter-electron Coulombic repulsion effects give rise to the so-called Mott-Hubbard insulators.

Another effect of significance is crystal field splitting of orbital energies. The local environment of individual cations produces orbitals of differing energies, these may then combine to form separate bands of different energy. Thus, although the total d-manifold maybe neither full nor empty, a thus formed sub-band may well be full and

the electrons are thus localised.

When Hund's rules and the Pauli exclusion principle are considered, it is also seen that a half-full band may be insulating. Quantum mechanical restrictions on the simultaneous exchange of position and spin may prevent transitory polar states from forming, thus preventing delocalisation.

Magnetic order offers a complication to the latter idea, where antiferromagnetic interactions place additional constraints on the allowed exchange of electrons of given spin. Where the preferred ordering is ferromagnetic however, a double exchange mechanism may support both ordering and delocalisation, each enhancing the other's stabilisation effect. This is aptly illustrated in the magnetoresistant manganate perovskites.

Other effects, such as mean free path restrictions due to crystalline disorder (after P. Anderson), also serve to favour localised  $3d^x$  electrons.

These types of localisation effects can be particularly pronounced in first row transition metal oxide compounds. Compounds formed from 2<sup>nd</sup> and 3<sup>rd</sup> row transition metals are more likely to be metallic due to the more extensive nature of 4d and 5d orbitals. This tends towards the formation of broader bands, reducing the electron-electron repulsion effects within the bands and eliminating at least this one significant tendency towards localisation. Other chalcogenide compounds are also more likely to show metallic behaviour due to the greater polarisability and extent of the 3p, 4p and 5p orbitals. Greater closed shell shielding from their respective nuclei leads to this effect and raises the possibility of conduction via the extended cation-anion bonding/antibonding molecular orbital.

## 7.2.2 Diamagnetism

Although, strictly speaking, it can be shown that diamagnetism cannot exist in a classical model, the simplest interpretation of a diamagnetic effect is that it arises due to the inertial response of electrons to the intrusion of an applied field. The magnetic properties of all electrons will tend to oppose that intrusion. The effect thus yields a tiny negative magnetic susceptibility. To a first approximation diamagnetism is independent of temperature, however where electrons are delocalised, the possibility of a slight (second order) temperature dependency exists.<sup>38</sup>

## 7.2.3 Paramagnetism

Localised electrons that are in a paramagnetic state may be thought of as having the direction of their magnetic moment pointing in random directions and that orientation fluctuating rapidly. Most magnetic materials show this state at a temperature above which any form of ordering or moment freezing has been lost due to thermal fluctuations. The random distribution of moment directions and fluctuations results in the material showing no net magnetic properties, other than in an applied field. The applied field causes some alignment of these relatively free moments and yields a positive magnetic susceptibility. In this state, interaction between adjacent atomic moments is considered to be insignificant. Some materials with unpaired electrons remain paramagnetic at all measurable temperatures, suggesting that magnetic ordering offers no further free energy reduction relative to the random fluctuating state.

The paramagnetic susceptibility of localised electrons is normally temperature dependent. This arises due to the thermal occupation of excited states, the greater the

temperature, the larger number of higher energy electrons, which are less susceptible to an applied field. For delocalised electrons in a metallic or metallic-like state, a second form of paramagnetism is found. The delocalisation implies that there are electrons in bands rather than discrete orbitals. Application of a field to the band lowers the energy of the spin states in the band parallel to the applied field relative to those not parallel. Electrons will then preferentially occupy the lower energy portion of the band, resulting in an excess of electrons in that spin-state relative to the situation without the applied field. This effect is known as Pauli paramagnetism, and it is to a first approximation temperature independent – being related to the band width and number of states available in a given spin state rather than temperature. This temperature independent susceptibility is a characteristic of metals and metal like materials.

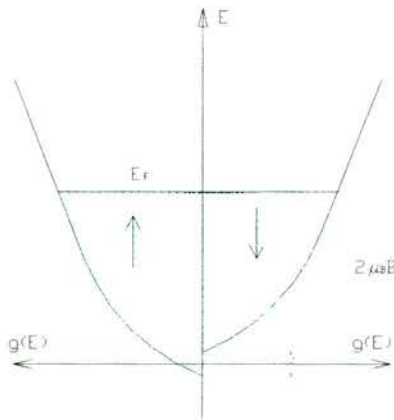


**Figure 7. 6 shows an excess of electrons occupying the spin up portion (left) of a band, where spin-up is parallel to an applied field and hence lower in energy than the spin-down portion. This gives rise to Pauli-paramagnetism.**

### 7.2.4 Magnetic order

Moments within a material can adopt specific ordered patterns where doing so serves to reduce the overall free energy of the material. This can be thought of as resulting from minute relativistic corrections to the energies of the chemical bonds in the material. Where thermal fluctuations become smaller than the reduction of the total

free energy due to such an arrangement of moments an ordering temperature maybe encountered. In general, as temperature is further reduced the degree of ordering will increase. The ordering temperature corresponds to the level of ordering whereby the extent of ordered regions is such to exceed the percolation threshold throughout the material over the long range. Effectively there are regions at great distance from each other throughout the material (on an atomic scale) that are related directly to each other by similar ordering through the intervening atoms. Such a transition is second order, showing a marked asymmetrical spike in heat capacity measurements. As the nature of the ordering directly relates moments at considerable distance from each other, it must also be cooperative. In other words regions at distance from each other have to co-operate, or behave in the same manner, to achieve the net ordering effect.

Magnetic information is passed from one moment centre to the next by means of exchange interactions. Exchange maybe direct or indirect. Quantum mechanical rules on electron exchange immediately constrain which electrons can be exchanged by preventing the simultaneous exchange of charge and spin. Indirect exchange mechanisms involve the exchange of magnetic information from one atom to another via some intermediary.

In the RKKY exchange mechanism, conduction electrons mediate magnetic information. This is typically the exchange mechanism found in rare earth and actinide elemental and alloy magnets, but can be found in other metallic compounds. In these, the magnetic electrons are usually unpaired f-series electrons. Being shielded by more extensive orbital shells, these cannot be involved in bonding or overlap with orbitals belonging to adjacent atoms. Accordingly, direct exchange is not possible. Instead, the moments belonging to these shielded f-series electrons

perturb the moments belonging to adjacent conduction electrons. These in turn effect the moment orientation of the conduction electrons *belonging* to adjacent atoms that in turn influence the moments in their respective f-series orbitals. Thus magnetic information is transferred from one atom to the next.

In chalcogenide compounds, indirect superexchange is generally by means of superexchange. This involves the exchange of electrons via a non-magnetic / metallic intermediate. Filled p-orbitals on the chalcogenide species serve as the intermediaries. Each p-orbital contains 2 electrons, these must have opposite spins. Consider 2 magnetic d-series ions either side of an oxygen in the figure below :

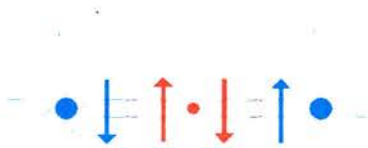


**Figure 7. 7 Shows the  $\sigma$ -type superexchange mechanism. The blue species represent d-series cations and the red oxygen ions.**

Exchange between the d-series cation to the left and the oxygen requires that the electron in the oxygen's overlapping p-orbital adopts the same spin direction as that of the left cation, e.g. down. The other electron in the same p-orbital on the opposite side of the oxygen must have the opposite spin direction, e.g. up. Accordingly, for it to be involve in exchange with the cation to the right, the cation to the right must adopt the spin-up configuration. Thus  $\sigma$ -type superexchange always leads to antiferromagnetic arrangements.

A second form of superexchange arises where say a d-orbital containing an unpaired (magnetic) electron overlaps more than one p-orbital lobe. This  $\pi$ -form of superexchange may give rise to either antiferromagnetic or ferromagnetic arrangements depending on which p-orbitals are overlapped.

### 7.2.5 Ferromagnetism

Ferromagnetism shows an arrangement of moments associated with individual cations such that they are all pointing in the same direction. Such a material thus has a net positive magnetisation below its ordering, or Curie, temperature. This magnetisation has little, or no, *susceptibility* to an applied field and thus susceptibility cannot really be measured below a Curie temperature. The magnetisation of a ferromagnet is normally taken to be positive, however any directionality must be relative to some fixed reference and it is possible that a ferromagnet's actual alignment is opposed to that of an applied field in a measurement.

Although locally, a ferromagnetic state may be the lowest energy configuration, across the bulk of the material it is not. This causes a bulk ferromagnet to break up into smaller ferromagnet *domains*. The *walls* between these domains could be thought of as being analogous to dislocation planes in a rock or a metal's microstructure. Movement of these domain walls is usually relatively slow and serves to pin the directionality of the moment within the domains. Crystalline defects, shear plains, etc can all enhance domain pinning effects. The degree of difficulty of moving these domain walls describes the hardness of the direction of the material's net magnetisation. Formally, the ease with which this direction can be altered by means of an applied field is termed the material's coercivity.

Extremely small ferromagnetic particles may form single domains. In such, the lack of distinct domains and other moment direction pinning features allows the moments in the single domain to act as if they are one large moment. Having nothing to hold this large single like moment in any given direction, it will align readily with an applied field. Such particles are said to be *superparamagnetic*. In some cases at

sufficiently low temperatures point defects may be sufficient to block this easy rotation of the moment. Alternatively, weak interactions between adjacent nanoparticles may have a similar effect.

Electrons whose moments give rise to a ferromagnetic state maybe localised or delocalised. Whilst the former situation is relatively easy to imagine, the latter is not. A delocalised electron ferromagnet is termed an *itinerant ferromagnet*. In the theory, explaining this requires the separation of an electron's magnetic properties and its charge. The magnetic properties remain on the cation whilst the charge is free to move. As the magnetic properties arise from the electrical ones this is impossible in reality. However, a picture may be constructed whereby the electron's magnetic properties are thought to become intrinsic to the chemical bonding of the material (usually metallic bonding). In order to maintain that bonding arrangement, the itinerant electron must adopt appropriate moment directionality even whilst in motion to satisfy this arrangement. Hence on average, the moment and its direction are localised about the cations. With this type of picture, simultaneous delocalisation and magnetic order are rationalised graphically as per the moment/charge separation concept.

A second form of itinerant ferromagnetism is found in compounds such as the manganate perovskites known as double exchange, this is not discussed further here.

### **7.2.6 Antiferromagnets**

These show an ordering temperature as per the ferromagnets, however in this case the ordering temperature is termed the Neèl temperature. On average, the ordering in antiferromagnets results in a net cancellation of bulk magnetisation, the individual

moments are arranged such that they cancel each other out. A simple up-down arrangement of adjacent atomic moments gives rise to such a state, however a large number of more complicated arrangements are possible. Such net cancellation of bulk magnetisation is also possible where the moment directions are distributed randomly. A random distribution however has no discernible symmetry associated with it. In antiferromagnets the adoption of the ordered magnetic state the ordering results in the presence of symmetry elements additional to those belonging to the chemical structure of the material alone.

### **7.2.7 Spin Glasses**

The spin glass state is relatively new in comparisons with better-known magnetic states such as ferromagnets, paramagnets etc.. It was recognised in the 1970s and 1980s and became the subject of much research. It is different from the ordered magnetic states insofar as no long range ordering of moments is observed, however the rapid fluctuations of the direction of the moments associated with a paramagnetic state disappear. In some senses a spin glass may be thought of as a frozen paramagnet. The nature of this spin freezing is intriguing. A defined spin freezing temperature can be seen which appears to indicate a phase transition of some form, but attempts to understand the nature of this transition show that it is quite different from other magnetic transitions and cannot be understood by adapting existing magnetic models. There is still debate as to whether a true spin-glass transition exists *per se.*, in the sense of more conventional types of phase transition.

This state was first recognised in alloys that were a dilute solution of magnetic atoms in an otherwise non-magnetic metal. In these materials, magnetic species interact via RKKY exchange interactions. As the interaction is via itinerant electrons that have

the freedom of the extended solid, this is a long-range interaction. The co-operation of large numbers of such itinerant electrons can cause it to be strong. However as the alloys contain only dilute concentrations of the magnetic species, on random structural sites, the propensity for the material to adopt a regular ordered magnetic structure is severely limited. The concentration of the magnetic species and the randomness of their distribution are key elements of this type of spin-glass. Locally, disorder in the distribution causes each magnetic atom to experience conflicting magnetic exchange signals from its neighbouring magnetic atoms.

It is found that within the *frozen* spin glass state that a range of moment fluctuations exist. This range, rather than a single generic fluctuation rate, results in moments responding differently to AC susceptibility measurements carried out using different applied AC frequencies. The measurement frequency acts almost as a strobe light on a rotating object, the susceptibility appears to be different depending on which frequency is used. This reflects the dynamics of the moment fluctuations, some being more able to respond to a given frequency than others. E.g. if the applied frequency greatly exceeds a particular moment's response time, then that moment response will not be observed by that frequency scale, the field will already have reversed before the moment can respond to the initial stimulus.

Spin glass states can also arise in more concentrated magnetic systems. Again however, the essential elements are found to be competing exchange interactions and a degree of disorder.

It would seem that disorder or some type of frustration prevents these materials from adopting a *normal* ordered magnetic structure. As temperature falls however and energy is removed from such a system, there comes a point where clusters of

moments begin to freeze locally. One can think of disorder preventing proper ordering, but also introducing local defects which serve to stabilise, or pin, frozen moments in small regions locally. Across the material as a whole however, these frozen moment regions are frozen in a random manner and no long range ordering is observed.

### 7.2.8 Geometric Frustration to Antiferromagnetic Ordering

Consider the case where local exchange interactions generally favour an antiferromagnetic ordering, but the moments are placed to form an array of equilateral triangles. As seen for figure 7.3 below, if the moments on the bottom two vertices order in alternative directions, there is no means of ordering the moment on the top vertex so as to satisfy the same alternating order with the moments on both of the other two vertices. Although this is shown for a single triangle, one can see that the general idea can be extended to an extended triangular array and also into a three-dimensional lattice of equilateral tetrahedra. This inability to satisfy all of the magnetic exchange interactions due to the geometrical positioning of the moments is termed Geometrical Frustration.

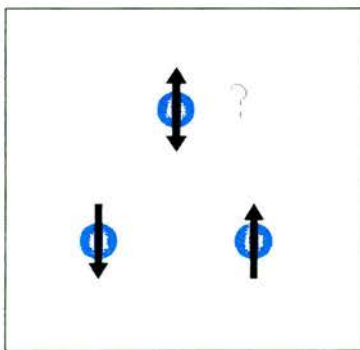


**Figure 7. 8 Illustrates the principle of geometric frustration**

In such a case, long range magnetic ordering cannot readily occur. Moments are expected to continue to fluctuate failing to come to any satisfactory ordering pattern.

If however, we lift the limitation that moments can only point up or down and introduce a fully three dimensional moment; it is seen that by pointing all of the moments towards the centre of the triangle (or directly out) or tetrahedra, the net moment across the structure would cancel out to zero. e.g. an antiferromagnetic array is possible, but necessarily creates a magnetic ordering pattern much more complex than one could do when restricted to the up/down situation. Moments are indeed fully three-dimensional, however ordered arrays of the kind just described are unusual. More commonly the material remains frustrated and unordered unless this geometric frustration is somehow removed. Given that the vanadium sub-lattice of the vanadate spinels examined in this work lie on such a tetrahedral lattice, this form of frustration is important to this work.

## 8.0 Experimental Techniques

### 8.1 Synthesis

#### 8.1.1 General

Synthesis of the polycrystalline materials discussed in this work has followed the standard solid-state *grind, press and react* method. Where appropriate, solid-state reactions were carried out under controlled atmospheres in order to maintain, or to control, oxidation states. The section on  $V_2O_3$  is longer than others reflecting some of the problems with this precursor and also makes some interesting observations on  $V_2O_3$  variants.

#### 8.1.2 Temperature profiles of tube furnaces used

The temperature profile in the tube furnace used for the reaction was determined using a thermocouple and proprietary meter. A long alumina rod, bored through with 4 small holes (<1mm) was used to house the thermocouple wires. These wires were threaded through the alumina rod and welded at a single point to form the thermocouple junction. Using a retort stand, the alumina rod was then placed into the tube furnace, positioning the thermocouple junction at a range of intervals (of approximately 25mm) through the length of the furnace. Measurements of the temperature profile were made with the furnace set to nominal temperatures of 800°C and 850°C. For the two furnaces employed, in the middle of the hot zone, both were found to be consistently c.10°C hotter than the set temperature. This was taken into account during synthesis and allowed for.

### 8.1.3 Precursors

Precursors prepared (as below) were stored in small glass jars inside a vacuum desiccator until required. It was found that  $V_2O_3$  was liable to degrade if stored for long (see below). Accordingly, this precursor had to be used within a few days of being prepared.

#### Vanadium sesquioxide ~ $V_2O_3$

$V_2O_3$  was prepared in-house by the reduction of ammonium metavanadate (Aldrich 99.9%).

Ammonium metavanadate powder was placed into an alumina boat and heated to c.670°C under flowing 5% $H_2$ /Ar, in order to effect the required reduction. After approximately 24 hours, the metavanadate was reduced to a fine black powder of vanadium sesquioxide.  $V_2O_3$  adopts the corundum structure. The structure and composition of this precursor were checked by XRD and TGA. Vanadium fluorescence under the XRD source yielded a large incoherent background in the XRD plots, making it difficult to assess phase purity. However, the principle  $V_2O_3$  peaks were visible above background allowing a lattice parameter determination to be made.

It was found that if this material was stored outside the desiccator or inside for a period of months, that it would initially turn blue (see below) and finally a deep green colour. The dark green variant was found to contain a significant amount of water in a neutron scattering experiment, where the water's protons resulted in so much incoherent scattering that the instrument's detectors became saturated and little other useful information was obtained. The green variant is presumed to be a hydrated

carbonate or hydroxide.

If the reduction was incomplete, the resultant powder could be coloured very dark blue rather than the required black. TGA suggested that this blue variant might have contained a small amount of excess oxygen. Though it proved difficult to gauge whether or not the material was fully oxidised at the end of the experiment.

Vanadium in the  $4^+$  oxidation state is known to produce blue coloured materials, e.g. vanadium dioxide. Curiously, both XRD and an exploratory elastic neutron scattering experiment found that the *blue*  $V_2O_3$  contained only the alumina structure.  $VO_2$  is known to adopt the rutile structure of which no traces could be found in the *blue*  $V_2O_3$ . The neutron data, particularly sensitive to oxides, failed to find other oxides in the sample. It is presumed that this incompletely reduced product is defect variant of  $V_2O_3$ . No reference to a blue coloured vanadium oxide of this structure could be found in the literature. Vanadium is known to produce an enormous number of oxide variants, it seems this blue material is probably yet another unrecorded variant.

It seemed for a while that the blue coloration might have been simply a surface effect, a fine coating of  $VO_2$  on bulk  $V_2O_3$ , however latterly this seems unlikely. Although this may have been the case where  $V_2O_3$  was exposed to the air and turned black to blue with time, on occasion the as-made  $V_2O_3$  showed this blue coloration. In this case, given solid-state diffusion as the likely rate-determining step in the reduction process, it seems very unlikely that the surface – exposed to the  $H_2/Ar$  – would be less oxidised than the bulk.

This difficulty in ensuring that the  $V_2O_3$  was  $V_2O_3$  proved troublesome in synthesis of the  $LiV_2O_4$  sample for the ILL INS experiment. Despite checking the lattice

parameters of batches of prepared  $V_2O_3$ , the synthesis did produce the spinel, but also yielded  $Li_3VO_4$  and  $LiVO_3$  impurity phases (details elsewhere) indicating a shortfall in  $V_2O_3$ . As the quantities were weighed out correctly one can only conclude that the precursor was in fact  $V_2O_{(3+\delta)}$ . This pointed to the likely reason behind the otherwise inexplicable failure of a number of other syntheses, (either out right failure or producing materials which were almost correct ~ spinel lattice parameter slightly off, or odd magnetic behaviour). Though inadvertent, some of these failed synthesis would provide useful data for comparison with good materials, marking the effect of slight deviance from the standard.

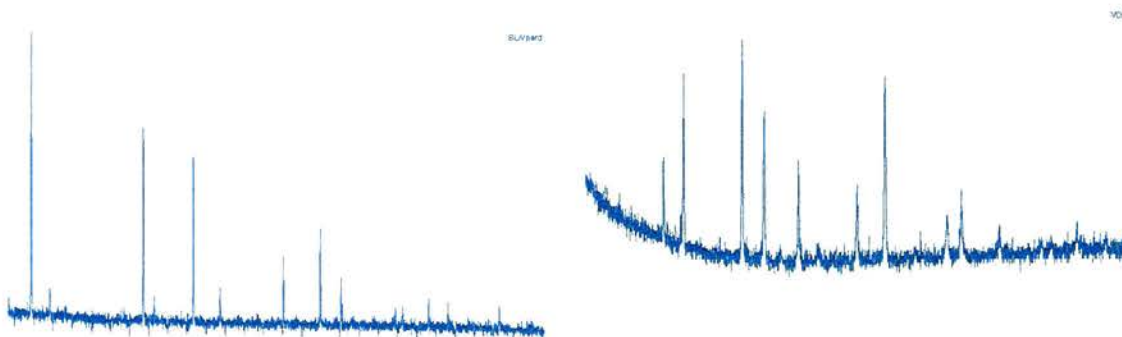


**Figure 8. 1 shows a typical xrd plot clearly demonstrating the fluorescence problem to the left with the principle spinel peaks seen above this incoherent background, to the right a more severe illustration of a  $V_2O_3$  pattern.**

### **Tri-lithium vanadate**

Tri-lithium vanadate was prepared by the reaction of lithium carbonate (Aldrich 99.6+%) with vanadium pentoxide (Aldrich 99.9%). A mixture of white  $Li_2CO_3$  and orange  $V_2O_5$  was heated to  $800^{\circ}C$  in an alumina crucible for c.48 hours. The resulting material  $Li_3VO_4$  was identified by means of XRD. To within the ability of the XRD technique, the material was shown to be phase pure and to contain no apparent impurity phases. Interestingly, the resultant powder would emerge coloured very pale

green or a very pale yellow. Sometimes, volumes of each colour were found in the same crucible/batch. No explanation could be found for this, nor difference found between the differently coloured materials by XRD.

### **Vanadium, zinc, and gallium oxides**

V<sub>2</sub>O<sub>5</sub> (Aldrich 99.9%), ZnO (Analar 99.5+%), Ga<sub>2</sub>O<sub>3</sub> (Alfa Aesar 99.99%) and were used. Suitable amounts were pre-dried prior to usage. V<sub>2</sub>O<sub>5</sub> was checked by TGA to confirm that the vanadium was fully oxidised.

### **8.1.4 Synthesis of Vanadate Spinels**

Appropriate quantities of V<sub>2</sub>O<sub>3</sub>, V<sub>2</sub>O<sub>5</sub>, Li<sub>3</sub>VO<sub>4</sub>, Ga<sub>2</sub>O<sub>3</sub> and ZnO were weighed out in appropriate amounts to achieve the correct stoichiometries and ground into a fine powder under acetone. These powders were then pressed into pellets using a uniaxial press using a pressure of between three and five tonnes. Some samples were also prepared simply as powders without pressing.

In order to maintain oxygen stoichiometry during the reaction, the reaction was carried out in a sealed quartz vessel under a low static vacuum, or under reduced pressure helium or argon. Prior to sealing the reaction vessel, in all cases it was flushed and vacuumed several times to minimise the residual quantity of air (and hence oxygen) present. Thermal expansion of gas in the reaction vessel at elevated temperatures would result in an increase in pressure within the vessel. It was prudent then to partially evacuate the vessel, irrespective of the type of atmosphere used. Crudely, the change in temperature from ambient to reaction temperature (300K-1200K) corresponds to a quadrupling of pressure within the vessel. The pressure (at ambient temperature) used in the reaction was c.  $1 \times 10^{-3}$  atmospheres, several orders

of magnitude lower than required for safety purposes.

The reaction was carried out between 800 and 850°C for roughly a week. Shorter reaction times of around four days were employed on occasion. These shorter periods produced equally good samples; the longer reaction time was simply more convenient. No attempt was made to determine the minimum reaction period required to produce satisfactory samples.

The use of an amorphous quartz glass for the reaction vessel meant that it was wise to avoid direct contact between the vessel and the reagents / products. If lithium or zinc were lost and got into the glass, it was possible that the glass might begin to crystallise and crack. It was also undesirable to lose reagents into the vessel. To minimise such problems, the *green* pellets / powder were carefully wrapped in gold foil prior to being placed in the vessel.

Carbon foil was also tried. Although one apparently good  $ZnV_2O_4$  sample was obtained using carbon foil, on several occasions when the pellets were wrapped in carbon foil, the desired product was not obtained (XRD). Said pellets were visibly damaged and the foil appeared to be *eaten away* in places. It seemed reasonable to deduce that the carbon was partially reducing the reagents / products. Carbon was thus abandoned in favour of gold.

## **8.2 Diffraction**

### **8.2.1 General**

Diffraction as a technique for establishing the arrangement of atoms in a crystalline material was established in the early 20<sup>th</sup> century, (initially employing beams of

electrons by Davisson and Kunsman).<sup>39</sup> The relationship between the observed diffraction patterns and the spatial arrangement of the atoms responsible for the scattering is encapsulated in Bragg's Law of diffraction ( $n\lambda = 2d\sin\theta$ , where  $n$  is an integer,  $\lambda$  is the wavelength of the incident radiation,  $d$  is the inter-planar separation of planes of scattering points and  $\theta$  the observed angle of the diffraction spot relative to the direction of the incident radiation).

The phenomenon was initially understood as the constructive interference of electromagnetic waves, however electrons (and later neutrons) had been shown to be particles, raising some awkward questions. This can be resolved by considering a random spherical scattering of the incident radiation from each atom in the sample and treating this as a probability wave, a probability of finding any scattered particle in a certain direction at a certain time. Significant amounts of radiation can only be scattered at given angles where the time-space relationship between a large numbers of scattered particles accumulates. This is a function of the de Broglie wavelength of the radiation and the geometric arrangement of the atoms in the crystal itself. Thus for radiation of a known wavelength, the observed pattern is a function of the crystal structure and its contents only. Max Von Laue – a German physicist –successfully obtained the first x-ray diffraction (XRD) patterns in 1912.<sup>40</sup>

Rather like the inversion of an image by a single lens, the diffraction pattern obtained by a crystal is related to the inverted structure, or the structure in *reciprocal space*. The repetitive nature of the atomic arrangement in a crystal lends its description to Fourier description where the inter-atomic distances are described by vectors.

Condensing the problem to the one-dimensional case a function  $n(x)$ , can be defined with periodicity  $a$  along some direction  $x$ , this can be expanded into a Fourier  $a\cos\theta+$

$b\sin\theta$  series as,

$$n(x) = n_0 + \sum_{p>0} [C_p \cos(2\pi p x / a) + S_p \sin(2 p x / a)] \quad \text{Equation 8. 1}$$

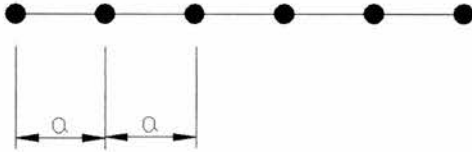


**Figure 8. 2 Shows a 1 dimensional lattice of periodicity “a”.**

Only points corresponding to  $2\pi p/a$  meet this requirement, e.g.  $p$  must be an integer, and are described as being points on the reciprocal or Fourier lattice. From the relationship;  $a e^{i\theta} = a(\sin\theta + i\cos\theta)^{41}$ , the above equation can be exchanged for one of the complex form :

$$n(x) = \sum_p n_p e^{(i2\pi p x / a)} \quad \text{Equation 8. 2}$$

Equations of this form dominate diffraction theory, convenient in that it is the same language that is used to describe waves. From this starting point the model can be developed to describe a real crystal, where two sets of vectors are recognised, one describing the basic lattice repeat unit, or lattice propagation vectors, and a second set describing the relative positions of atoms within that repeat unit, or basis set. The lattice repeat unit is the primitive unit cell. The atomic positions within the structure are delta functions of this wavelike description of the structure and the function describing the lattice is zero valued elsewhere in space.

The diffraction theorem is that it is the set of characteristic reciprocal lattice vectors for a particular crystal structure that defines the permitted scattering directions.<sup>42</sup>

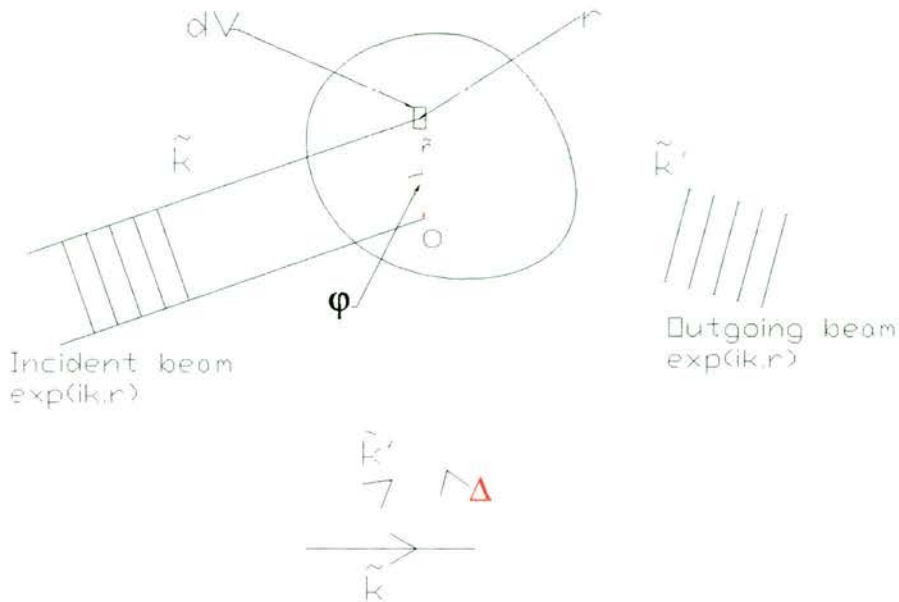


**Figure 8.3 (upper)** shows scattering occurring from 2 elements in a bulk crystal sample. The wave vector of the incident beam is  $\vec{k}$  and for the emergent beams is  $\vec{k}'$ . The vector construction (lower diagram) shows the geometric definition of  $\Delta\vec{k}$ , the scattering vector.

In figure 8.3 above, we determine the conditions under which scattered beams from different parts of the crystal emerge coherently. A phase difference can be defined from the difference in path lengths for the incident beams scattering at points  $O$  and  $r$  as  $r \cdot \sin\theta$ . This phase can be thought of as relating the time, speed and distance characteristics of particles scattered from different parts of the crystal. The difference in phase angle between the incident beams is  $(2\pi \cdot r \cdot \sin\theta) / \lambda$ , which is equal to the dot product of the vectors  $\vec{k}$  and  $\vec{r}$  ( $\vec{k} \cdot \vec{r}$ ). For the scattered beams the equivalent phase angle difference is  $(-\vec{k}' \cdot \vec{r})$ . The difference in phase angle between the beam scattered at point  $O$  and that at point  $r$  is  $(\vec{k} - \vec{k}') \cdot \vec{r}$ . Particles or waves scattered from a volume element at point  $O$  relative to that at point  $r$  have a phase factor of  $e^{i(\vec{k}-\vec{k}')\cdot\vec{r}}$ . The total amount of scattering in the direction of  $\vec{k}'$  then becomes the sum of all volume elements in the crystal which result in coherent scattering in that direction, e.g. those that meet the coherence or phase condition  $e^{i(\vec{k}-\vec{k}')\cdot\vec{r}}$ .

A scattering vector  $\Delta k$  (as opposed to scattered  $k'$ ) is defined as the change in direction of the wave vector in the scattering process. From the vector addition illustrated in figure 6 above, we see that  $k + \Delta k = k'$ . Thus  $e^{i(k-k')\cdot r}$  becomes  $e^{i\Delta k\cdot r}$  and the total amount of scattering in the direction of  $k'$  is:

$$F = \int dV n(r) e^{i\Delta k\cdot r} \quad \text{Equation 8.3}$$

Where the volume integral  $[\int dV n(r)]$  accounts for the number of volume elements at positions  $n(r)$  contributing to the observed scattering. We can see that this equation is of very similar form to that of the Fourier description of a crystal developed earlier, yet that described a lattice only, whilst 8.3 only describes the coherent scattering condition of a wave or particle stream from different volume elements of some material.

Where the scattering occurs from the crystal previously described, the two can be combined to describe the coherent elastic scattering from that particular crystal.

$$G(r) = \sum_G n_G \cdot e^{i(G\cdot r)} \quad \text{Equation 8.4} \quad F = \sum_G \int dV n_G \cdot e^{i(G-\Delta k)\cdot r} \quad \text{Equation 8.5}$$

Where  $G = \Delta k$ , the exponential term becomes  $e^{i(0)\cdot r} = 1$  (from  $e^0 = 1$ ), hence  $F$  collapses to  $F = Vn_G$ . At any value of  $\Delta k$  other than  $G$ ,  $F$  becomes trivial. It is seen that the set of characteristic reciprocal lattice vectors ( $G$ ), their Fourier components ( $n_G$ ) and sample volume ( $V$ ) determine the amount of observed scattering at an angle corresponding to some wave vector  $k'$ . If no scattering (above background) is observed at some angle (for incident beam of given wave vector), then there is either no characteristic reciprocal lattice vector corresponding to that angle, or the value of the Fourier components is for some other reason negligible, e.g. it corresponds to a destructive interference type effect.

In elastic scattering there is no change in the scattered particle's energy, or a new photon of identical energy to the absorbed incident photon is created and emitted. Thus wave vectors  $k$  and  $k'$  have the same magnitude, i.e.  $k^2 = k'^2$ . From  $k + \Delta k = k'$  and  $\Delta k = G$ , we get,  $k + G = k'$ . Squaring both sides gives  $(k + G)^2 = k'^2 = k^2$ , and hence, [from  $k^2 + 2kG + G^2 = k^2$ ],  $2kG + G^2 = 0$ . The latter could also be written as:

$$2kG = -G^2 \quad \text{Equation 8. 6}$$

This seems odd algebra, however the vector  $G$  will be equally characteristic irrespective of its direction, thus  $G$  is equivalent, in this relationship, to  $-G$ .

Miller indices ( $hkl$ ) are used to describe equivalent sections or planes cutting through the lattice at some angle to the unit cell axis. As these equivalent planes are repeated *ad infinitum* at a fixed distance from each other throughout the crystal, each also corresponds to a translational vector mapping one plane to the another – such a vector may or may not correspond to a characteristic reciprocal lattice vector ( $G$ ). As the equivalent planes are parallel to each other, the corresponding translational vector will be normal to the plane. For any reciprocal lattice vector ( $g$ ) [where  $g = hb_1 + kb_2 + lb_3$ ],  $d(hkl) = 2\pi/|g|$ , and so  $|g| = 2\pi/d(hkl)$ .

$$\text{Thus from (8.6), } 2(2\pi/\lambda)\text{Sin}\theta = 2\pi/d(hkl) \quad \text{Equation 8. 7}$$

Where the  $(2\pi/\lambda)\text{Sin}\theta$  term comes from the product of vectors  $k$  and  $g$ , where  $\theta$  is the angle between the two vector and  $\lambda$  is  $1/k$  (from definition of the wave vector  $k$ ). Cancellation of terms through (8.7) yields,

$$\lambda = 2d_{hkl} \text{Sin}\theta \quad \text{Equation 8. 8}$$

Thus we see that the diffraction condition  $2kG = -G^2$  is equivalent to Bragg's law.

Expressed as  $n\lambda = 2d\sin\theta$ , recognises two additional possibilities. Firstly, a common factor in the Miller indices and secondly that integral multiples of the same wavelength will behave in the same manner as the fundamental.

Some people find it convenient to view the scattering along certain Bragg directions as arising from successive Miller planes, others prefer the summation across all pairs of atoms related by a translational vector. However,  $G$  is simply related to Miller planes, being the vector perpendicular to the planes describing their propagation. Woolfson writes, “whether or not one is formally justified in thinking of a diffraction process in terms of specular type reflection is not too certain from the physical point of view but, since the two types of description are mathematically equivalent, there is no harm in doing so.”<sup>43</sup> In the limiting case of a perfect crystal, this equivalence is perhaps complete. However, the specular reflection interpretation may present difficulties when one attempts to account for the thermal motion of atoms, vacancies, other static atomic displacements or disorder.

Bragg’s law is of little help in predicting which diffracted beams will be seen in an experiment. It only serves to relate the angle of scattering to a d-spacing (for fixed wavelength). One could randomly pick any d-spacing and it would give us an angle, and *vice versa*.

It is observed that simple structures exhibit fewer diffraction peaks or spots than more complex ones – if the scattering theorem is valid, this implies fewer characteristic reciprocal lattice vectors. It is also evident that it would require a set of fewer vectors to construct a simple structure than a more complex one.

Where a unit cell is non-primitive, symmetry elements within the basis set result in it

containing translational vectors mapping equivalent atoms within the cell. A number of such translations will also serve to map an atom to its equivalent position in the next unit cell. In such a manner one can see that the certain unit cell translations may become redundant in lattice construction – they are already implied in the basis set. This makes the general suggestion that a primitive reciprocal space unit cell may be a better place to look for characteristic vectors than the conventional real space unit cell for any given structure (which is chosen for convenience).

The characteristic vectors for any structure can be found by constructing the Wigner-Seitz primitive unit cell of the reciprocal lattice, details of this can be found in Kittel and other standard Condensed matter text books.<sup>44</sup> It can be shown from this that all of the characteristic vectors of a structure are found in this primitive cell and hence this cell defines the observed diffraction pattern.

The intensity of scattering observed in any Bragg peak or diffraction spot is determined by two principle factors. Firstly, the number of scattering site contributing to the observation, and secondly the strength of scattering from those sites. Electromagnetic radiation and electrons are scattered from charge density within the sample, and hence by the electron clouds surrounding the atoms. Neutrons however are scattered by nuclei. The strength of scattering from the former two is thus directly proportional to the number of electrons in the clouds of the atoms in the sample. Hence, the heavier the atom, the stronger the scattering. The scattering strength of atoms with respect to neutrons is complex and unrelated to atomic number.<sup>45</sup>

Magnetic scattering is another possibility. Diffraction patterns reflect order within the structure and so the magnetic properties of the incident radiation can equally interact with and scatter from magnetic structure as well as atomic structure. The  $s = 1/2$

neutron can respond to this as readily as electromagnetic radiation or electrons. However, the strength of magnetic scattering of x-rays and electrons is extremely small in comparison with their respective strengths of atomic structural scattering. Hence only with very specialised equipment is possible to discern magnetic scattering using those techniques. Neutrons however show a magnetic scattering strength of the same order as their atomic scattering length, making them an ideal probe of magnetic structure.

Displacement of atoms from their ideal sites via thermal motion has an interesting consequence. These displacements produce a time-averaged reduction in the number of scattering sites that meet the strict diffraction condition and hence reduce the observed scattering intensities. This reduction can be shown to be dependent of scattering angle and is described by the following term:

$$= \exp(-2B_{\text{iso}} \sin^2 \theta / \lambda^2) \text{ Equation 8.9}$$

The parameter B is the Debye-Waller factor, related to the temperature dependent vibration and hence displacement of the atoms about their ideal sites.  $B_{\text{iso}} = 8\pi^2 \langle u_x^2 \rangle$ , where  $\langle u_x^2 \rangle$  denotes the thermal average of the mean square displacement of the atom from its equilibrium position. The  $\langle u^2 \rangle$  term is often referred to as  $U_{\text{iso}}$  and is done so in this work. The expression can be expanded to account for non-isotropic thermal motion, this is not done here however.

Intuitively, and in practise, the Temperature factor extracted from peak intensities is expected to fall with decreasing atomic motion as temperature decreases.<sup>46,47</sup>

Vacancies in some crystals may permit greater freedom of some atoms adjacent to the vacancies to undergo increased thermal spatial motion, this being reflected in the

thermal parameter.

Certain types of disorder within a largely crystalline material can also lead to distinct features. For example, structures with large numbers of vacancies which have some sort of local order, but no long range order may show marked diffuse scattering features.<sup>48</sup> Imagining an oxide material with some of the oxide anions removed, one could imagine that the ions surrounding the vacancy might move a little closer together or even further apart in an attempt to minimise the total energy of Coulombic effects in the structure locally. Single, fairly isolated, vacancies will have a negligible effect on the average position of the surrounding atoms. However, large numbers of such atoms, or bulk displacements caused by strain within the crystal might alter typical atom-atom distances resulting in a slight “tail” on the Bragg peaks to the higher angle/lower d-spacing side of the peaks reflecting the distribution of shortened real space distances.

The peak size and shape observed in powder diffraction is thus a combination of several factors but also include instrumental factors from the experiment itself. It should be possible to model the observed patterns and to thus determine the quantities of atoms and their relative displacements from their ideal sites. This is done in Reitveld refinement, however deconvolution of the observed peak shape and size into those factors via fitting a parameterised theoretical model of the material to the observed pattern is not always capable of determining values reliably. There can be large error factors associated with extracted parameter values and some caution is required in their interpretation. The modelling process is simple in essence, involving the fitting of a series of parameterised equations describing the model pattern to the observed pattern. The fitting usually employs a least squares method, but other

techniques, such as Monte Carlo simulation, can also be employed. As with solving any set of equations the number of variables that can be fitted reliably is dependent on the number of independent equations that can be constructed and fitted to the experimental data. Simultaneous refinement of both x-ray and neutron data, taking a single model structure, modelling it using the two sets of equations needed to construct both x-ray and neutron models, then fitting those to both types of data from the same sample has obvious enough advantages in terms of that reliability. This is done where possible in this work.

### 8.2.2 Constant wavelength Techniques

In constant wavelength diffraction, a monochromated incident beam is directed onto the sample and the scattered radiation is measured at angles around the sample by a camera or a position sensitive detector. More traditionally, the pattern would be recorded by a photographic film surrounding the sample.

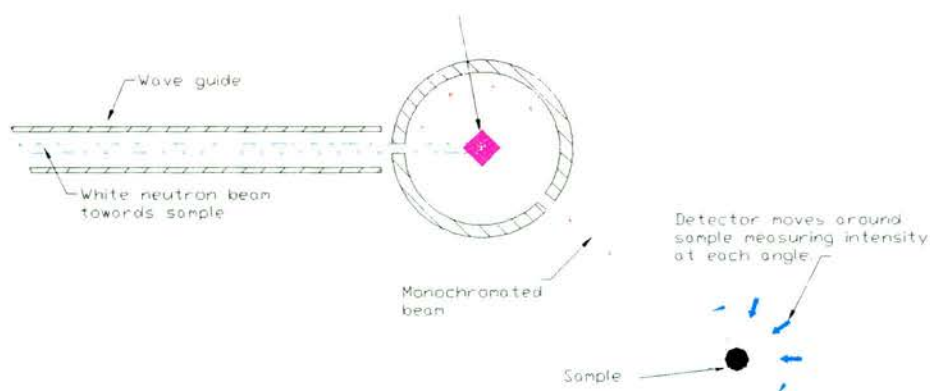


Figure 8. 4 shows a schematic of a typical CW diffractometer

In powder diffraction, the detector is moved through a single angle, whereas in single

crystal measurements it is moved to cover a region of solid angles. In a modern development, electronic image plate detectors are now being used on some instruments, combining the advantages of a photographic film (collecting simultaneously across a large area of solid angle) and those of a PSD where intensities can be measured more accurately than by photographic means.

Powder diffraction may be carried out in transmission or reflection geometries, sometimes referred to as Debye-Scherrer and Bragg-Bretano geometries respectively. The scattering is the same in either process, however in transmission the incident beam is shone through the sample and the diffracted beams passing through the sample are measured. In reflection geometry, the incident beam is shone onto the surface of a sample mounted in a flat container and the pattern collected at angles to the surface.

Transmission experiments generally give more reliable relative peak intensities than reflection geometry, however the absolute intensity measured per unit incident flux is reduced relative to that observed in the reflection experiment. This reflects the volume of sample the radiation passes through, and the consequent amount of absorption and to an extent the probability of multiple scattering involved. In reflection geometry, the diffracted beams originate mainly from volume close to the surface and tend to be less attenuated by the latter effects. In reflection geometry preferential orientation of crystallites close to the surface can have significant effects.

### **8.2.3 White Beam techniques**

Two forms of diffraction experiment utilise a white beam.

In a Laue experiment (restricted to single crystals), a white beam of x-rays or

neutrons is directed onto the sample and the pattern is collected on a photographic, or image, plate that covers the largest practical area of solid angle. The resulting image is usually covered in thousands of Laue spots.<sup>49,50</sup> Complete modelling of such a pattern completely can be extremely difficult, as each wavelength present in the white beam produces its own characteristic pattern all of which sum to give the collected pattern. Plainly, reflections from different wavelengths are very likely to overlap. However the total pattern is characteristic of the crystal and it is seen that certain wavelengths from the mixture scatter very strongly in certain directions.<sup>51</sup> This is very useful for aligning single crystals prior to a CW diffraction or inelastic scattering experiments. This experiment is also the basis for the crystal monochromation of white beams (as above). The Laue technique is also useful for biological molecules that are often damaged quickly by the incident flux – in that it can collect a large amount of information relatively quickly.

The other technique which utilises a white beam is termed time of flight (ToF) and is normally used in neutron scattering. Unlike x-ray photons that travel at light speed irrespective of wavelength, neutrons of different momenta or wavelengths travel at different speeds. Shorter wavelength implies faster, longer – slower. It follows that for a white beam of neutrons, starting from a single point, they will separate and spread out as they travel down the wave-guide according to their speed.<sup>52</sup> This allows the Bragg equation to be turned around and the experiment to run such that instead of measuring how a CW scatters at different angles, we measure the scattering intensity at a single angle with varying time (and hence wavelength).

$$\lambda = 2d \sin \theta, \quad \text{but as } \lambda_n = \frac{hT_{(oF)}}{M_n l}, \quad \text{so } \lambda_n = \frac{hT_{(oF)}}{M_n l} = 2d \sin \theta \quad \text{and hence,}$$

$$d = \frac{hT_{(oF)}}{2M_n \sin \theta} \quad \text{Equation 8. 10}$$

Where  $\lambda_n$  is the effective wavelength of the neutrons (from their momentum), determined from their rest mass  $M_n$ , the distance they travelled ( $l$ ), and the time taken to do so ( $T_{(oF)}$ ). Hence, for a constant path length from the neutron source through the sample to a detector, by counting when the neutrons arrive we can discriminate between wavelengths and thus obtain a diffraction pattern, and thus the term *Time of flight (ToF)*.

Although it is possible to make these time, speed and distance calculations to determine the neutron wavelengths, errors in measuring absolute times and distances can be significant. In practice, it proves easier and more reliable to normalise a detector in an experiment using a standard sample crystal – already well characterised by CW methods, thus calibrating the instrument rather than calculating.

Normally, a time of flight instrument utilises banks of detectors at fixed angles rather than a single detector. This makes for more efficient use of the neutrons scattered in all directions from the sample. As each detector position is equivalent to the others in its bank, parameterised by the change in position (angle and distance from neutron source), patterns from each detector can be normalised and summed to give a single pattern of many times the total scattering intensity than from a single detector pattern.

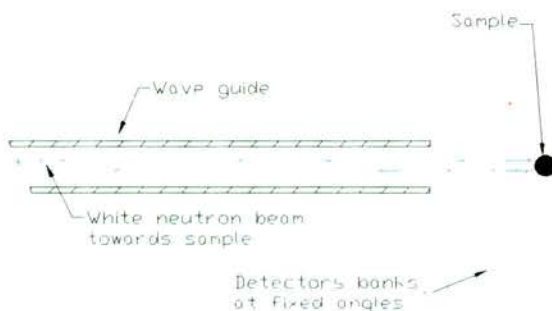


**Figure 8. 5 shows a schematic of a fixed detector bank ToF neutron instrument.**

In addition to calibrating each detector in the bank and normalising them to each other, the patterns are also normalised to account for the distribution of wavelengths in the incident white beam. This can be done by measuring the number of neutrons reaching a detector point at various times in the incident beam (beam monitor). To make the time of flight technique possible, it is important to be able to define a starting time, where the position of the neutrons in the beam is known. This can be achieved in one of two ways or by using a combination of both.

Spallation sources are also pulsed sources. That is to say, the proton beam that causes the neutrons to be smashed from the heavy metal target is directed onto the target in well-defined pulses. Thus instead of having a continuous supply of white beam neutrons to the sample, short bursts are used. It becomes possible then to time these bursts so that the slowest neutrons in the burst have reached the sample and detectors before the fastest ones from the next burst arrive. Failure to meet this condition results in an effect termed *frame overlap*, which would render the experiment useless. To further reduce the likelihood of this effect, devices called choppers can be placed in the wave-guides between the moderator and sample area. These serve to open and close the beam path such that only certain portions of the spreading white beam are selected. Thus the slow, or other unwanted, neutrons can be *chopped out* of a pulse.

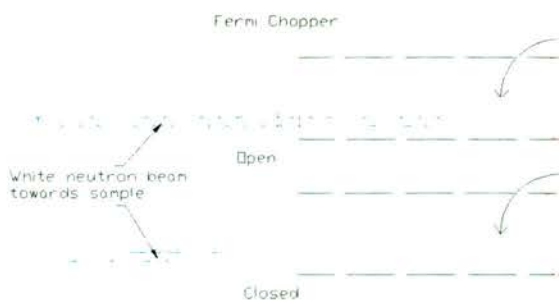


**Figure 8. 6 shows a schematic of Fermi chopper operation.**

This is also the second time defining technique. The Fermi chopper is a rotating disc with a hole running from one face to the other, made from a neutron absorbing material.<sup>53</sup> Synchronising its rotation speed with the pulse, the hole is open to the pulse only so as to let the required neutrons pass, the others are absorbed by the chopper itself. By using choppers in synchronised sets it also becomes possible to use them as monochromation devices, selecting only specific velocities of neutron. Although a mainstay of pulsed spallation sources, these devices can also be used on the white beam of a reactor source to allow ToF techniques to be used there, e.g. instrument D7 at the ILL.<sup>54,55</sup>

### **8.3 Magnetic Measurements**

A number of commercially built magnetometers were used to make magnetic measurements on the samples made. Most of the measurements were carried out using d.c.- squid magnetometers built by Quantum Design (San Diego, USA), models used were the MPMS and MPMS-XL.

In all cases, the sample under investigation is moved through a set of detection coils as shown schematically in figure 8.7 below. Any magnetism associated with the sample will induce some sort of change in the electrical properties of the coils as it is moved through them. This change is then recorded and converted into a measure of the magnetisation/magnetic susceptibility of the sample.

### 8.3.1 dc Measurements

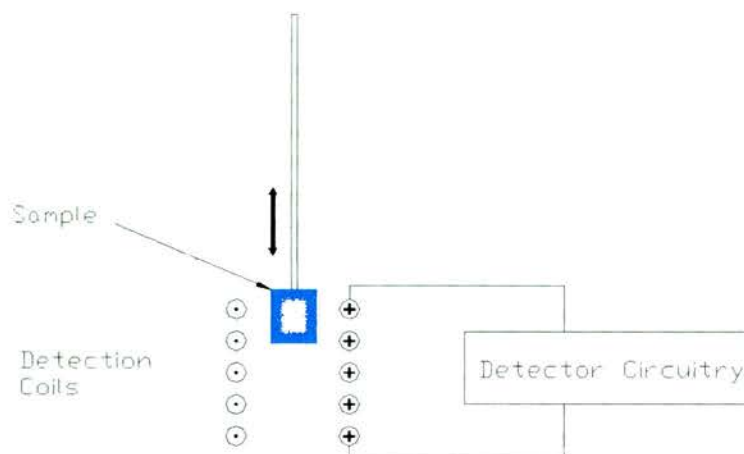


**Figure 8. 7**  
**Schematic of a d.c.**  
**magnetometer**

A magnetic sample moving through the coils causes a change in the magnetic flux inside the coils according to Faraday's Law. This change in flux induces a current proportional to that change to flow through the coil that can then be measured by the detector circuitry. Having calibrated the measuring equipment with a sample of known magnetic properties, the induced signal can be converted into an overall magnetisation value for the sample.

Where the sample being measured has no spontaneous magnetic properties, a dc magnetic field is applied during the measurement and the sample's magnetic susceptibility is determined from the relationship  $\chi_{dc} = M / H_{dc \text{ applied}}$ , where  $H_{dc \text{ applied}}$  is the applied dc field and  $M$  the measured magnetisation. From the latter equation, if a spontaneous magnetisation value can be measured in the absence of an applied field, then the idea of that sample having a magnetic susceptibility is flawed, as clearly  $\chi_{dc} = M / 0 = \infty$ . Below a spontaneous magnetic ordering temperature, electrons in an ordered ground state are not susceptible to applied fields in the same

manner as in paramagnetic state. The d.c. measurement is one of magnetisation and not susceptibility *per se*.

In order to prevent the measurement coils simply measuring the applied d.c. field a pair of balanced detection coils are employed, wired in opposition so as to provide net cancellation of the effects of the applied field. The presence of the sample in one of the coils disturbs this balance and allows a net current to flow. In practise, the perfect balancing of coils is not possible and applied fields are never perfectly homogeneous, however the slight imbalance can be accounted for in the instrument calibration and the measurement made on the basis that the sample causes the difference between the observed magnetisation value and the no sample values. Moving the sample through a series of such coils wired in opposition to each other and regressively fitting the observed voltage / movement plot allows most of such systematic instrumental errors to be removed.

DC methods have been greatly enhanced in terms of sensitivity since the advent of superconducting technologies. The inability of a material in the superconducting state to support a voltage plus their perfect diamagnetism results in an exceptional sensitivity to nearby magnetic materials trying to induce a current as they pass such a material. In a squid magnetometer the metal wire coils of a traditional dc system are replaced with detector loops made from superconducting materials. Elimination of electrical resistance in the detector loops and the consequent increased sensitivity would have been a major advance in dc techniques in itself, however these detector loops are also linked to dc squid devices that are capable of detecting minute variations of magnetic flux.

Fig. 8.8 below shows a schematic of the magnetic signal detection system used in a

QD squid magnetometer. The detector array, made from a superconducting material, is isolated from the rest of the circuitry, signals being carried to the squid detector through the superconducting isolation transformer. The heater attached to this transformer allows these elements to be heated to above the material's superconducting temperature ~ doing so ensures that all residual persistent superconducting currents are removed prior to making each measurement. This transformer is also designed to filter out RF noise.

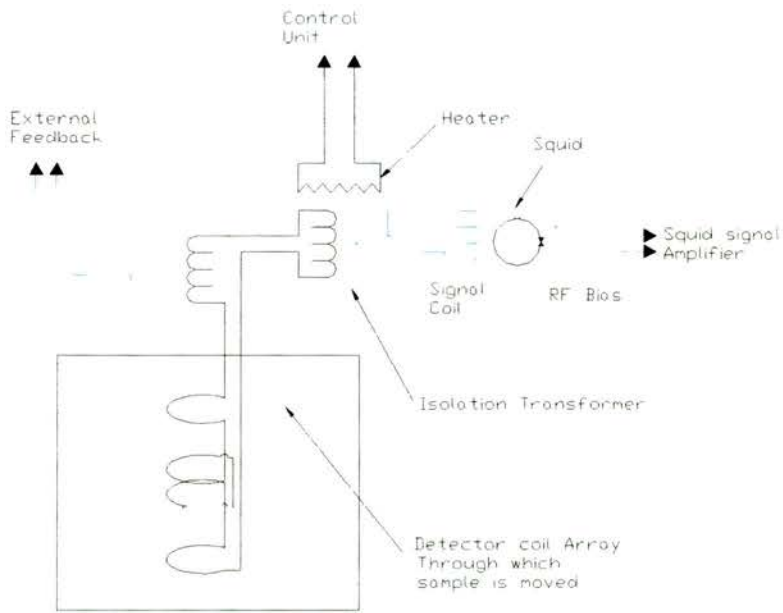
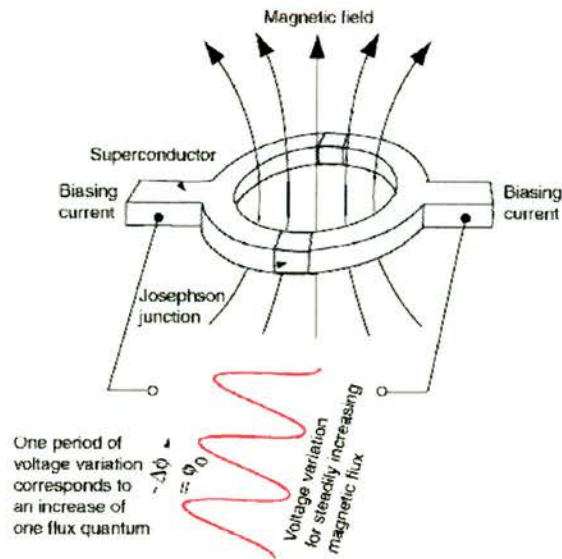


Figure 8. 8 Schematic of detection circuitry in QD MPMS-XL magnetometer. <sup>56</sup>



**Figure 8. 9 Schematic of a squid device.**<sup>57</sup>

The squid device itself consists of a pair of Josephson junctions as shown in fig. 8.9 above. These junctions are formed when two pieces of superconducting material are separated by a thin insulating strip (hence SIS junction). A constant dc bias current-modulated by the external feedback circuitry is passed through the device. This results in the measurement of an ac voltage across the SIS junctions and hence the device overall. The presence of any externally caused magnetic flux within the loop interferes with the wave-functions of the electrons passing through each SIS junction, producing a phase shift across the junctions in addition to that caused by the junctions themselves. The difference between the applied feedback modulation and the squid loop's signal is monitored using a lock-in amplifier or similar device. The feedback is then adjusted so as to cancel the effect of the external flux on the loop. Hence by measuring the amount of feedback-induced flux is required to cancel the external flux, one can infer the amount of external flux present.<sup>58</sup>

The acquired signal is then fitted against a standard signal profile obtained from a calibration sample and the absolute magnetisation determined. This process is

completely automated in the QD MPMS and MPMS-XL systems.

### **8.3.2 Corrections and conversions applied to data**

It is normal to correct measured magnetic susceptibilities and magnetisation measurements to account for demagnetising effects due to the geometry of the sample. This has not been done in the data presented in this work. This is justified on the basis that the volume of the samples being measured was sufficiently small that they could be considered as point sources. As none of the samples considered were found to be ferromagnetic internal demagnetising fields were not considered. Anisotropy effects are averaged out and not anticipated in powdered polycrystalline samples.

DC magnetisation measurements were converted to nominal gram susceptibility by dividing by the applied field and scaling the resultant value according to the mass of sample used in the measurement. Where appropriate, the gram susceptibility was multiplied by the molar mass to yield molar susceptibilities. No attempt is made to model “susceptibilities” below apparent ordering temperatures. Modelling in the paramagnetic region was on the basis of a modified Curie law relationship (see theory section).

## **8.4 $\mu$ SR**

The  $\mu$ SR acronym can be used in reference to a number of different types of muon experiments, which aim to investigate the spin dynamics of a magnetic system. In this case, the technique referred to is that of muon spin relaxation.

### 8.4.1 Muons

The muon is a short-lived sub-atomic particle that was first observed experimentally in 1933 by Kunze in Rostock<sup>59</sup>. Whilst investigating the interaction of cosmic rays with matter in a cloud chamber, he observed some sort of decay process that produced what appeared to be an electron and some other unrecognised particle. The basic properties of this new particle were determined by Neddermeyer and Anderson in 1937 whilst they were measuring the energy loss of particles in cosmic ray / material interactions. They deduced that this new particle, or muon, was much smaller than a proton, larger than an electron, and carried a unitary charge. Later, it was discovered that the muon was in fact a decay product of an even shorter-lived particle known as a pion. The pion itself a product resulting from collisions between matter and cosmic rays.

It was found that there were three different kinds of muon, positive, negative and neutral, each the decay product of a pion of the same charge. Unlike the pions which have no net spin, the product muons do have an intrinsic angular momentum, or spin. To conserve spin in the decay process, neutrinos are also formed, their spin being in the opposite direction to that of their corresponding muons. The effective magnetic moment arising from the muon's spin is c.3 times that of the proton or electron. Charged muons have a charge of  $\pm 1$ , like a proton or electron. The muon's mass is c.1/9<sup>th</sup> that of a proton and c.200 times that of an electron. In some senses, charged muons can be viewed, and used as, either light protons or very heavy electrons.

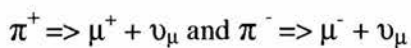
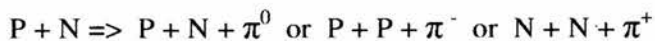
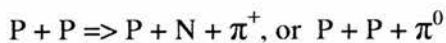
### 8.4.2 Muon Production<sup>60</sup>

Particle physicists discovered that if materials were bombarded with high energy

particles, that not only could atoms be smashed up into protons, neutrons and electrons, as per Rutherford's splitting of the atom; but that if sufficiently high energy incident particles were used that it was possible to smash the protons and neutrons themselves into their even smaller constituent particles. If light elements such as carbon, are chosen as incident beam targets, then the probability of smashing the nucleons is larger than it would be were heavier elements chosen. This can be rationalised simply by considering the number of nucleons per unit volume. Heavier elements have more nucleons to be ejected from their nuclei and to thus absorb the energy of the incident particles. Hence, such means can be used to produce useful numbers of neutrons and protons. Lighter elements, have fewer nucleons and so, for the same incident beam energy, it is likely that a significantly larger numbers of the nucleons will be smashed in order to absorb the incident energy.

The incident beam used in this process is usually a high-energy proton beam. All three types of pions and hence muons are produced in such a spallation process, some of the nuclear equations for their production are noted below.

P = Proton, N = Neutron,  $\pi$  = Pion,  $\mu$  = muon and  $\nu_{\mu}$  = neutrino ( $\mu$ )



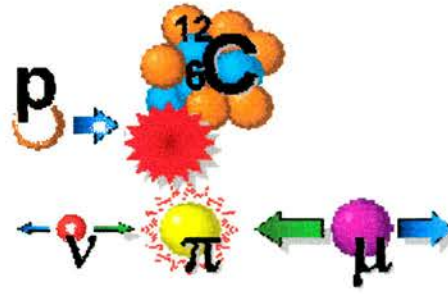


**Figure 8. 10 to the right shows the chain of events leading to Muon production : proton beam smashing a light element nucleus, pion emission and subsequent decay into Muons and neutrinos.**

These pions have a half-life of 26 nanoseconds. A range of additional, more complex, pion producing nuclear reactions are possible at very high incident beam energies, however, those given above constitute the most common ones.

Charge-less  $\pi^0$ s and  $\nu^0$ s are impossible to guide and extremely difficult to detect even, these are lost from the production process. Useful muons can be extracted in a number of ways from the production process.

Positive and neutral pions in, but close to the surface of, the target material can decay as above emitting their respective muons. The charged muons can be guided using magnetic and electric fields towards the sample to be investigated. Negative pions in the target material are likely to be captured by the target nuclei and become involved in the pionic disintegration of the nucleus without the formation of muons and hence are also *lost* to the process. This is known as *the surface beam* production method, capable of producing only positive muons. These pions decay whilst *at rest* in the target material and the resulting muons all emerge with the same energy (29.8 MeV/c) and hence velocity.

However, not all of the pions remain in the target material, many are ejected during the spallation process. Again the neutral pions will be lost to the process. The positive

and negative ones can be separated using electrical/magnetic fields. These will then decay to give muons. These are termed *decay channel muons*. The above fields can also be used to separate and select pions of different velocities (energies) which will in turn produce / select muons of different energies. This production method is thus more versatile in being able to produce positive and negative muons over a range of energies. By choosing the muon energy it is possible to influence how penetrating these investigative particles will be.

The stream of muons produced emerges from the pion decay process 100% spin polarised. This has been termed a maximal violation of parity symmetry. It constitutes one of the rare occasions in which nature is seen to have a “handed-ness” at a fundamental level. One would normally expect to find a random distribution of spin orientations in such a process. This 100% initial spin polarisation conveniently provides one of the pre-requisites for MuSR studies.

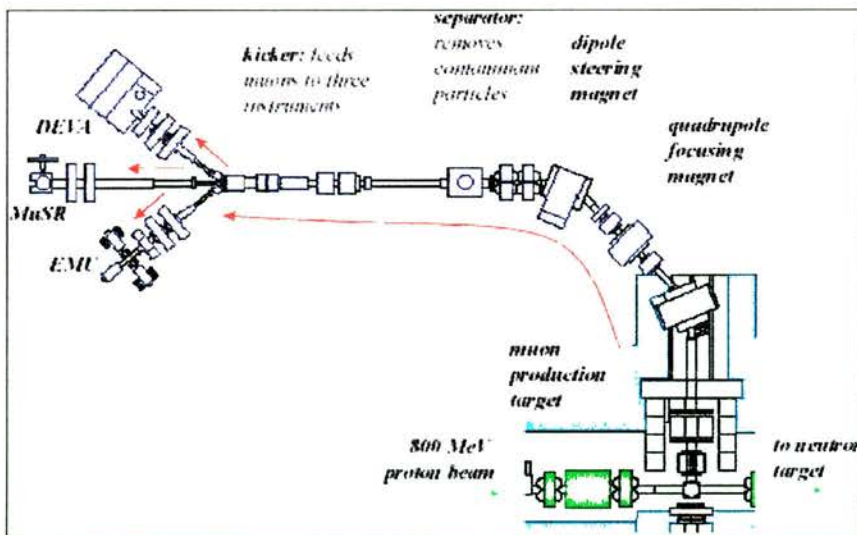


Figure 8. 11 Production and instrumentation of surface beam muons at ISIS RAL.

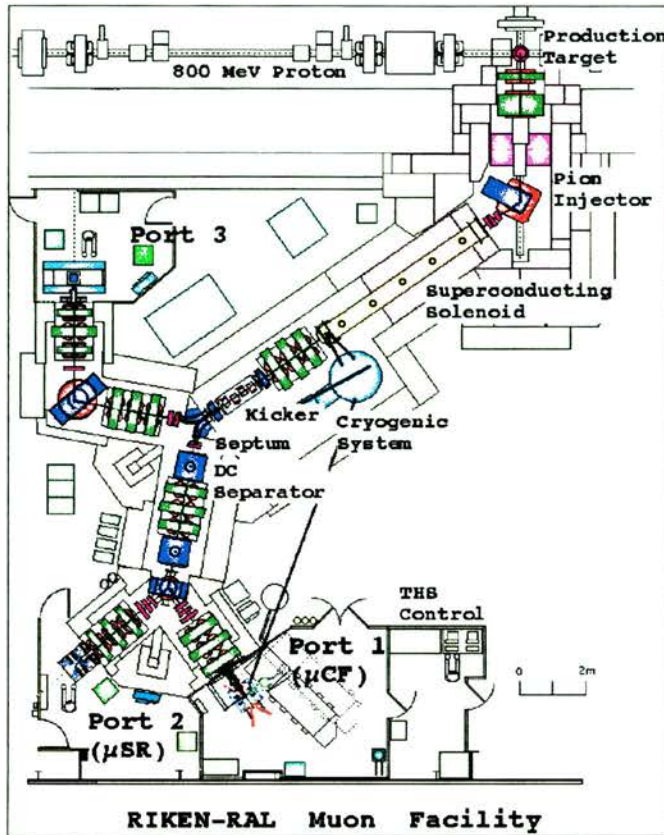


Figure 8. 12  
Production of decay  
channel muons and  
instruments at the  
Japanese Riken/ISIS  
facility, at ISIS, RAL.

The above figures 8.11 and 8.12 show the muon instruments, production targets and wave-guides at ISIS, RAL, UK.<sup>62</sup> The instruments Argus (port 2,  $\mu$ SR on the ISIS/Riken facility) and MuSR were used in this work. The properties of positive muons are summarised in the table 8.1 below.<sup>63</sup> In this work only pulsed source MuSR is considered.

Property	Value
Mass ( $m_\mu$ )	206.83 $m_{\text{electron}}$
Charge ( $Q_\mu$ )	+1
Spin ( $I_\mu$ )	1/2
Magnetic moment ( $\mu$ )	3.183 $\mu_{\text{proton}}$
Average lifetime ( $\tau_\mu$ )	2.197 $\mu$ S
Gyromagnetic Ratio ( $\gamma_\mu$ )	$2\pi \times 136 \text{ KHzT}^{-1}$

Table 8. 1  
Summarises the  
properties of the  
positive muon.

### 8.4.3 Muons in the sample

Once in the sample, after an average lifetime of 2.2 $\mu$ s, muons decay to yield positrons

or electrons ( $e^+$  or  $e^-$ ), the charge being the same as the corresponding muon (and more neutrinos). With such a short muon lifetime, one might wonder what use they are, is it possible to get them into one's sample before they decay even? Muons emerge travelling at a significant fraction of light speed, (approximately 0.24 times light speed from the surface beam production process). Uemura quotes Brewer *et al.* (1975) estimating that the muon slowing and embedding itself in the sample process typically occurs in less than 1ns.<sup>64</sup> Thus the transport and implantation processes occur so rapidly that any magnetic interactions between the muon and the sample that occur during implantation are insignificant by comparison with subsequent interactions. Muons emergent from the channel decay process can have even higher velocities. As positive muons are the mainstay of MuSR techniques, the rest of this description will assume that only positive muons are being considered.

Once a muon has entered the sample, it rapidly comes to rest (thermalises). Being charged, the muon will seek a position in the sample that minimises its electrostatic interactions with the sample's atoms. For example, in a closed packed metal oxide lattice, one might imagine positive muons occupying tetrahedral or octahedral holes in the oxygen sub-lattice that are not occupied by a metal cation.

Muons are not always restricted to staying in one place in a sample however. Hopping can occur either by quantum mechanical tunnelling or by a thermodynamically activated process. The latter is akin to the motion of the transport ions in an ionic conductor. The two forms of hopping process have different characteristics. By measuring the hopping rates over a range of temperatures, it should become possible to model the process(es) and to distinguish between quantum tunnelling and thermally activated motion. During this hopping process, the muons

lose their original collective spin polarisation allowing the hopping rates to be inferred from the depolarisation rates.

Given that a positive muon is in many respects similar to a small proton, this allows MuSR techniques to investigate the motion of proton like particles in materials and hence may have applications in the modelling of proton conductors.

Alternatively, the muon's magnetic moment can interact with local magnetic features in the sample. Remembering that the muons were originally spin-polarised, one might expect that interactions between the muon and local magnetic features in the sample would also cause the reorientation of the individual muons' spin directions. This does occur and the process is termed depolarisation. In a static (ordered or disordered) magnetic environment, the muon's spin will reorient such as to minimise its potential energy. In a fluctuating local environment, the muon's spin direction is expected to do likewise. The muon spin is expected to precess in sympathy with the local fields it experiences.

#### **8.4.4 Positron emission & depolarisation**

The positrons produced during the decay of the muons are emitted preferentially in the direction of the muons' spin at the time of decay. Emitted positrons can be detected and counted using scintillation tubes. By counting the number of positrons detected in different positions around the sample it becomes possible to measure the muon depolarisation rate in the sample over time.

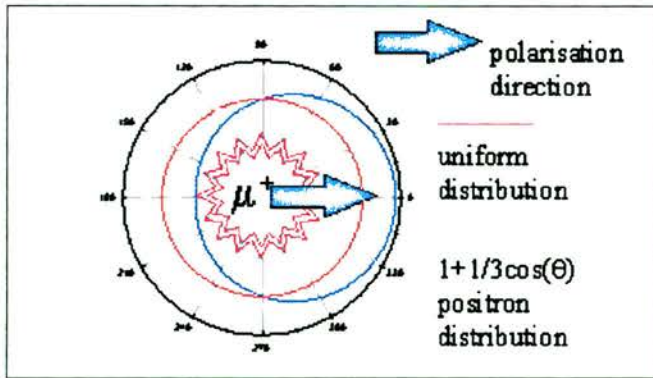


Figure 8.13 Shows how the emitted positron direction is biased in the direction of the muon spin at the time of decay.

The direction of the emitted positrons is strongly dependent on the direction of the muon spin at the time of its decay. This is shown in figure 8.13. Strictly, the distribution of positron emissions follows a  $P(\theta) = 1 + a\cos\theta$  function, however the  $a$  parameter is found to be dependent on the energy of the muons. In typical MuSR experiments, muon energies are c.30 MeV/c resulting in  $a$  being approximately 1/3.

It is noted that the muons do not all decay at the same time, the time quoted is a mean value. This is a process similar to the spontaneous decay of unstable radioactive nuclei where there is a no means of predicting when any particular particle will decay, but a very predictable statistical overall rate of decay. Thus for a packet of muons delivered into a sample from a pulsed source, there is a natural distribution of decay times related to the half life of the muons, irrespective of the muon's interaction with local magnetic fields.

The sample is usually mounted in a holder inside a cryostat or furnace and changes in the muon depolarisation rate observed over time, against changes in sample environment such as temperature or magnetic field. As long as the sample mounting materials have a constant and predictable effect on the depolarisation, they can be calibrated into the measurement and will not interfere with the relevant observations. Non-magnetic elements such as silver or aluminium are ideal in this context. In this

work silver containers were used.

The detector arrangement used to measure muon depolarisation rates is very simple.

A schematic diagram of a muon instrument is shown below;

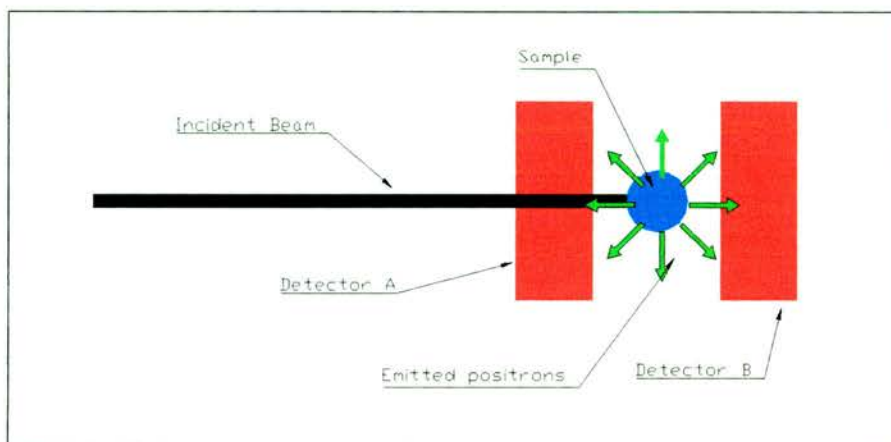


**Figure 8. 14 Shows a schematic of a longitudinal or zero field MuSR sample and detector arrangement. In addition to the elements shown there are also two sets of coils providing longitudinal and transverse magnetic fields for usage as required.**

The number of positrons counted at some time and some point is described by

$$\Delta N(t) = N(t)(1 + a_0 P(t) \cos \theta) \delta t \delta \sigma \quad \text{Equation 8. 11}$$

Where  $N$  is the number of positrons,  $t$  is time,  $\delta \sigma$  is the solid angle covered by the detector,  $a_0$  is the inherent initial asymmetry of the system including instrument calibration and background, and  $P(t)$  describes the time dependent polarisation of the thermalised muons.

For detectors placed at the front and back of the sample, were the implanted muons to sit static in the sample and not precess due to local magnetic fields, the distribution (asymmetry) of positron counts at both detector would be described by the  $P(\theta) = 1 + a \cos \theta$  function. Interactions between the muons and the sample disturb this distribution and allow the interactions to be probed by examining the change in this

distribution. The natural half-life time distribution of muon decay events allows variations in behaviour to be followed over time, reflecting the time dependent dynamics of the magnetic environment.

Expressions describing the number of positrons expected at the front and back detectors over time are:

$$\Delta N_F(t) = N_0 e^{-\frac{t}{\tau}} (1 + a_0 P(t)) \delta t \delta \sigma \quad \text{Equation 8. 12}$$

$$\Delta N_B(t) = N_0 e^{-\frac{t}{\tau}} (1 - a_0 P(t)) \delta t \delta \sigma \quad \text{Equation 8. 13}$$

And the asymmetry of positron counts with time over both detectors is given by:

$$A(t) = \frac{N_F(t) - N_B(t)}{N_F(t) + N_B(t)} = a_0 P(t) \quad \text{Equation 8. 14}$$

The  $a_0$  value is described as the initial asymmetry, this effectively describes the degree of polarisation of the muons at the moment of thermalisation, but also includes other phenomena such as detector efficiency, random background counts and other detector triggering events (for example counts from stray electrons).

It is often interesting to see how the application of a magnetic field influences magnetism in a material. If that field is applied parallel to the direction of the muon's initial polarisation, then that field will not of itself tend to depolarise the muons with respect to that direction. From the experimental arrangement required, such a field is described as longitudinal (LF). Carried out with no such field, the experiment is described as zero-field (ZF). An alternative experiment may be carried out where instead of using front and back detectors, detectors are placed left and right of the sample. In this case, the applied field is actually transverse with respect to the detectors, this is thus described as a transverse MuSR experiment. This field

transverse to the initial muon polarisation causes the muon spins to precess around the applied field, leading to oscillations in the observed asymmetry. The experimental data thus obtained focuses on observing the behaviour of these oscillations with changing temperature or applied field strength. This experiment is not discussed further here.

The *alpha* value including these instrumental effects is determined in an initial experiment often termed T20 or T40. This refers to the strength of a small field applied to the sample transverse to the direction of the muon's initial spin. This causes a damped oscillation, as above, to be seen in the observed depolarisation rate and hence asymmetry. These oscillations can be fitted to extract the alpha value, calibrating the system with respect to detector efficiencies background and such like. The small field is applied using an additional set of coils to remove the need to change anything else in the experimental set-up prior to the main experiment. Once the latter effects have been measured in this type of experiment, the extracted alpha value calibration is then used in fitting the LF or ZF experimental data to account for such effects and allow the extraction of fitted parameters.

The thermalised muon spin orientation is modified by local magnetic fields via dipolar interactions. If we assume that local fields are random, then after some time the muons will become completely depolarised. For positive muons, their spin orientation is parallel to their momentum, thus if the  $a_0$  value is correctly extracted, the asymmetry value should drop to around 1/3rd of its initial value, marking the transition to a random distribution of spin orientations in three dimensions from the initial polarisation in a single direction. The depolarisation process is however time dependent, thus the way in which asymmetry changes over time is indicative of the

depolarisation rate, and hence of local spin fluctuations. Where spin fluctuations are rapid and entirely random, as in the paramagnetic state, the muons experience averaged local fields. These spin fluctuations are largely too fast for the muons to respond to and the depolarisation rate is low. As the rate of these local fluctuations decreases, possibly due to the system approaching a spin-glass or ordered magnetic state, the muons become progressively more capable of responding to the local fields and the depolarisation rate becomes more rapid. In the case of static, ordered or frozen glassy, local moments, the depolarisation is rapid.

Magnetic fields that the muons respond to are not restricted to those arising from electrons. In the absence of any electron magnetism, nuclear moments in the sample can act to depolarise the muon spins. As the muons will be sited at a greater distance from nuclear moments than they would be from magnetic electrons, the influence of nuclei is correspondingly weaker than that of electrons. The strength of the nuclear-muon interaction is also dependent on the moment of the nuclei, (those of zero spin having no influence), influence increasing with increasing nuclear spin. In many systems both nuclear and electron influence is observed. In the vanadates of these studies, the vanadium cations carry an  $S = 7/2$ -spin and so nuclear-muon interaction is expected. The presence of two such influences on the depolarisation rate complicates interpretation of observed data.

An applied field has an additional effect however. As muon-nuclear interactions are weak relative to muon-electron spin interactions, an applied field can serve to decouple the muons from their nuclear interactions whilst still leaving them susceptible to muon-electron spin interactions. Thus in the LF/ZF experimental geometry, it is possible to some extent to discern between electron and nuclear effects

by observing differences between ZF and small LF experiments. It is difficult to estimate at what strength the nuclear decoupling field will begin to have a measurable impact on the muon-electron interactions however. Whilst a field as small as 50 Gauss may be sufficient to decouple nuclear effects, in finely balanced electron magnets it may also have some effect on the electron-magnetism. Finally, the observed experimental data is correct for the system under investigation and whether or not an applied field is influencing the electron magnetism becomes a matter of interpretation.

#### **8.4.5 Modelling Muon Behaviour**

As a relatively young experimental technique MuSR is still in the development stage. Much of the early work on developing analytical models has been carried out on metals and alloys rather than the oxides discussed in this work. As such, analytical models of muon behaviour in the multitude of known oxide structures are not widely available and it is beyond the scope of this work to develop such models.<sup>65</sup> Additional problems present themselves insofar as many of the available data fitting functions contain several parameters, whilst individual datasets may present relatively simple depolarisation curves. This situation lends itself towards a significant danger of over-fitting and over-interpreting of the data. In isolation, MuSR data can be difficult to safely interpret. Despite such problems, it can however unambiguously discern features like spin freezing, rapid or slow magnetic transitions *et sim.*

Depolarisation functions virtually always follow some form of modified exponential decay. For metallic dilute spin glass alloys, Uemura showed that the distribution of dynamic fields experienced by a thermalised muon is Gaussian, however, a summation over a number of different muon sites combined with the probability of

muon site occupation resulted in a Lorentzian distribution.<sup>66</sup> In the fast fluctuation regime, the total muon depolarisation rate for any given muon site would be described by:

$$G_z(t) = e^{-(\lambda t)^{1/2}} \quad \text{Equation 8.15}$$

However, in a concentrated spin glass like system, the muons are sited adjacent to many more magnetic sites. The fields experienced by a muon are more concentrated and the distribution of fields is rather different. The distribution is expected to be narrower for a muon site as there are fewer possible arrangements of muon and magnetic sites. Campbell *et al* suggested that the behaviour to a concentrated system might be better described by a stretched exponential function<sup>67</sup> :

$$G_z(t) = e^{-(\lambda t)^\beta} \quad \text{Equation 8.16}$$

Where, crudely,  $\lambda$  represents the local magnetic fluctuation rate and  $\beta$  represents the distribution of the fluctuation times of those fields.

This function is further parameterised by a scaling factor, in this case  $a_0$ , the initial asymmetry value. Thus the function becomes:

$$G_z(t) = a_0 e^{-(\lambda t)^\beta} \quad \text{Equation 8.17}$$

This function is useful for fitting MuSR data generally, however it is somewhat indeterminate as it can be used to fit almost any broadly exponential decay. Thus, whether or not the  $a_0$ ,  $\lambda$  and  $\beta$  parameters have any real physical significance becomes debatable. Where the observed data maps a simple relatively featureless curve, there may be a number of combinations of the parameters that yield the observed curve, emphasising the earlier comment on over-fitting.

For the concentrated magnetic system, in the fast fluctuation limit, where muon behaviour approximates paramagnetic behaviour, there will be little difference in muon behaviour between a true paramagnet, and a system heading towards a spin glass or ordered magnetic state. Thus it should be possible to use the same function to fit the depolarisation rates both above and below spin freezing transitions.

In collecting the experimental data there may be additional technical complications. Detector dead time; this describes the ability of the positron detector system elements to reset themselves after making a count in order to be able to make the next count. Secondly there is an overall dead time associated with the pulsed nature of the source and the ability to the detector system to register and measure the start of each pulse of muons/positrons. These are a function of the relevant instrument's capabilities, the instrument Argus has a large number of detectors and a high intrinsic ability to make measurements from extremely close to the start of each muon pulse. As a result, the Argus dead-time value is considered to be effectively zero. This allows an improved estimate of the observed  $a_0$  over that of the instrument MuSR that has a significant dead time. The latter is measured experimentally and factored into the data fitting process. An additional factor is the frequency/time resolution of the instruments, e.g., how accurately the instruments can measure individual time events. Frequency resolution on the ISIS pulsed source instruments is poor in comparison with that of steady state sources and instruments such as those at PSI. A combination of dead times and limited frequency resolution places limits on the ability of the ISIS instruments to measure detail, particularly at very short relaxation times. The magnitude of the experimental error exceeds that of the details of interest. In part, the ISIS instruments make up for these limitations by offering a relatively large muon flux.

$a_0$ , the initial asymmetry value should be treated with caution if this is varied. Strictly speaking at  $t_0$  the implanted muons have had no time to interact with the sample and are still spin-polarised. Thus suggesting there is an initial asymmetry of physical meaning is suspect. However, in practise, because the experiment can never really measure  $t_0$ , some depolarisation will have occurred before anything is measured. An isolated initial asymmetry value has little absolute meaning. However, comparison of a number of fitted initial asymmetry values taken from the same sample under different conditions, at different temperatures perhaps, gives some indication of changes that are occurring on the very rapid timescale between implantation and the initial measurement. Thus changes can indicate spin depolarization effects at ultra short timescales where the particular measuring instrument cannot access.

the lack of frequency resolution also loses the oscillations expected in the relaxation behaviour of ordered magnets at these very short times. These oscillations are indicative of the type of magnetic ordering present and can be modelled to unambiguously determine the same. Further, different forms of order which are simultaneously present, for example low dimensional ordering combined with a spin wave result in a convolution of such oscillations, their deconvolution allowing both contributions to be determined.<sup>68</sup>

In this work muon data is fitted to stretched exponential functions using Francis Pratt's WiMDA MuSR data analysis software.<sup>69</sup>

#### **8.4.6 Muons – a local probe**

MuSR techniques reflect the local magnetic environment of the muon rather than being a bulk probe like susceptibility. The data collected are the linear combination of

many individual environments, thus in some cases it becomes possible to distinguish between different a number of different magnetic phenomena occurring simultaneously within a sample. Examples might include a system showing long range order in one direction plus a spin density wave in another, or some of the perovskites, which have antiferromagnetic order in perhaps the bc plane direction, plus an FM ordered component in the  $c$  direction.<sup>70</sup> It is the different muon precessions induced by these local environments that produce the oscillations at short muon decay times mentioned above.

One can also see that muon behaviour will be influenced by the proportion of the volume of a sample that is in a particular state. Thus, if one were to follow a magnetic transition with temperature, from a paramagnetic regime, through the growth of antiferromagnetic clusters, to a fully ordered antiferromagnetic: in the paramagnetic regime a starting asymmetry value would be noted, as antiferromagnetic clusters begin to form the asymmetry should fall in proportion to the volume of clusters present, until finally in the bulk antiferromagnetic state it should approach the value of c.  $1/3^{\text{rd}}$  (the paramagnetic value) expected for an ordered state. As such MuSR offers a reliable means of assessing whether a transition is continuous or sudden.

## **9.0 ZnV<sub>2</sub>O<sub>4</sub> Structural Studies**

This section deals with the crystal structure of ZnV<sub>2</sub>O<sub>4</sub>. *Prima facie*, this is a cubic spinel that undergoes a very slight tetragonal distortion at around 50K. However, the spinel distorts in seemingly the *wrong* direction. Features such as structural dynamics, spin-orbit coupling and crystal field effects from next-nearest neighbours are all considered as possible explanations for this.

### **9.1 Ambient Structure**

ZnV<sub>2</sub>O<sub>4</sub> is a cubic spinel that undergoes a slight cubic to tetragonal distortion at low temperature. Ueda *et al.* had reported this distortion as being the unusual  $c < a$  variant in 1997.<sup>71</sup> Recognising this as being extremely unusual for a spinel with a single B-site cation type (The similar compound MgV<sub>2</sub>O<sub>4</sub> is the only other reported example), it merited further study.

Structural studies were mainly by powder neutron diffraction (PND). Vanadium however has a coherent neutron scattering length close to zero. As a result, the vanadium nuclei are effectively invisible to the PND experiment. A room temperature (RT) XRD pattern, collected at length, from the sample used for most of these studies was used in combination with a RT PND pattern in a simultaneous Reitveld refinement using GSAS to:

1. Ensure the integrity of the sample.
2. Confirm the structure at ambient temperature.
3. Determine the fractional site occupancies.

4. Thus provide a basis for comparison with the low temperature PND studies.

The XRD pattern was collected on a Bruker D8a diffractometer<sup>72</sup>, in reflection geometry. Much of the incoherent fluorescent scattering generated by vanadium cations under a  $\text{Cu}_{k\alpha}$  incident beam was eliminated by carrying out this experiment in a furnace designed for this diffractometer. It is thought that the furnace windows acted as filters absorbing some of the fluorescence, however this instrument also had its monochromator on the detector that would remove most of the fluorescence.

PND data collected from HRPD was used in conjunction with that from the D8a for the RT refinement. The data was fitted to space group Fd-3m, (#227), firstly the lattice parameter, histogram scale factors and background were varied. The HRPD zero point was varied to lock both data sets together. Peak profile parameters were then varied. Finally, thermal factors and fractional occupancies were varied. (NB this general refinement strategy is also used in subsequent modelling). Figures 9.1 and 9.2 and table 9.1 below show the results of the RT refinement.

Cubic, Space Group Fd-3m, Fractional Coordinates:

Zn at	x = 0.125	y = 0.125	z = 0.125
V at	x = 0.5	y = 0.5	z = 0.5
O at	x = O(x)	y = O(x)	z = O(x)

[U =  $U_i/U_e \cdot 100$ ]

T(K)	$\chi^2$	a (Å)	Vol(Å <sup>3</sup> )	O(x)	$U_{\text{Zn}}$ (Å <sup>2</sup> )	$U_{\text{V}}$ (Å <sup>2</sup> )	$U_{\text{O}}$ (Å <sup>2</sup> )
293	1.088	8.406231(11)	594.0240	0.260507	0.531(21)	0.596(27)	0.404(18)

**Table 9. 1 gives parameters extracted from the room temperature combined neutron and RRD refinement.**

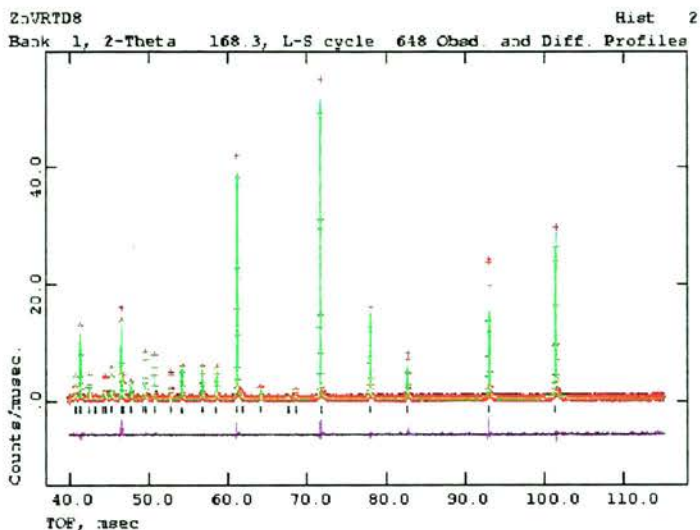


Figure 9. 1 shows the fit of the refined model to experimental neutron data, (Experimental data points are in red, the model is in green and the difference curve is shown below in purple; this convention is followed in all plots of refined data).

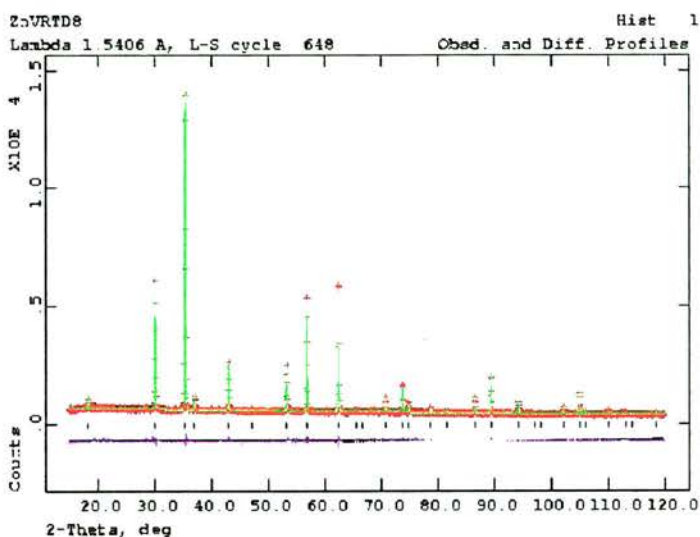


Figure 9. 2 shows the fit of the refined model to experimental x-ray data.

As seen in the plots shown above, an excellent match was obtained between the model and observed data. Temperature factors compare rationally with those for the same elements in similar environments.<sup>73</sup> No evidence is found of the presence of impurity phases. The extracted lattice parameter at  $8.4062\text{\AA}$  matches the published values. Fractional occupancies refine essentially to one, indicating the spinel is normal and that there is no evidence of either cation or oxygen deficiency. This sample is thus confirmed as being of good integrity and suitable for the purposes of

further studies. zero field-cooled magnetic susceptibility data (shown later) further strengthens this view, again being in good accord with published data.

## 9.2 Structure at 4K

Earlier PND studies on Polaris showed the reported slight low temperature structural distortion in the form of certain Bragg peaks being visibly misshapen, figure 9.3 below. These peaks were obviously splitting, but the split at this resolution was too slight to resolve and fit them properly.

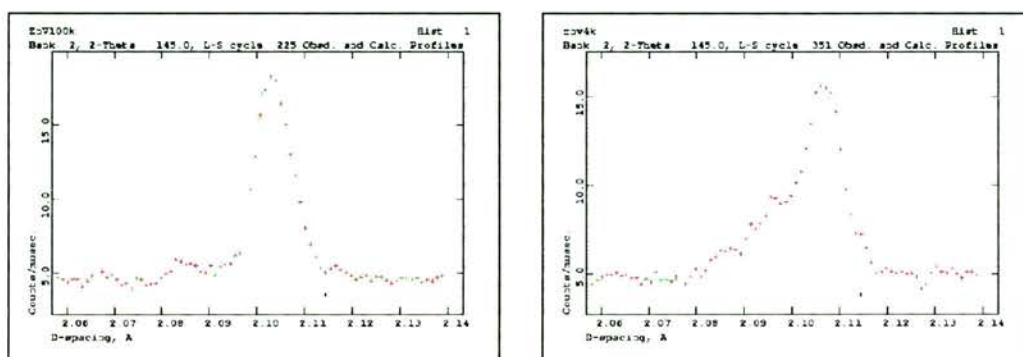


**Figure 9.3s (a) and (b) shows the same peak in powder neutron diffraction patterns for  $\text{ZnV}_2\text{O}_4$ , [(4,0,0) cubic], the one to the left was collected at ambient temperature, whilst that to the right was collected at 4k. Clearly the refined model (green line) fails to model both to the cubic structure.**

HRPD data collected at 4K has this splitting well resolved. Suspecting that the tetragonal distortion might take the same form as that for  $\text{LiMn}_2\text{O}_4$ ,<sup>74</sup> (allowing for the direction of the distortion being reversed), the model used was space group  $I4_1/amd$  (#141, setting 2). The initial tetragonal lattice parameters  $a$  and  $c$  chosen corresponded to  $a$  and  $\sqrt{2}a$  from the near equivalent cubic structure. In refinement, fractional occupancies were fixed at the values obtained from the RT refinement, varying the lattice and other parameters as before yielded the fit and data shown in figures 9.4 and 9.5 and table 9.2 and associated data below. During this and

subsequent neutron only refinements, variation of the vanadium thermal factor and fractional occupancy is pointless. Unable to see the vanadium, the refinement returns negative or otherwise meaningless values for these parameters. Data sets from HRPD's back-scattering and 90° detector banks were used in the refinement.

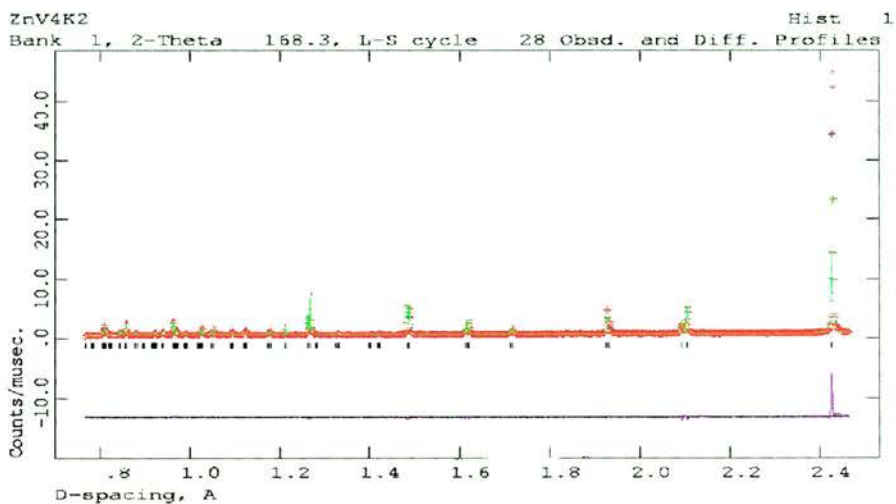


Figure 9. 4 shows the powder neutron data, model and difference plot for the tetragonal  $ZnV_2O_4$  spinel structure at 4K.

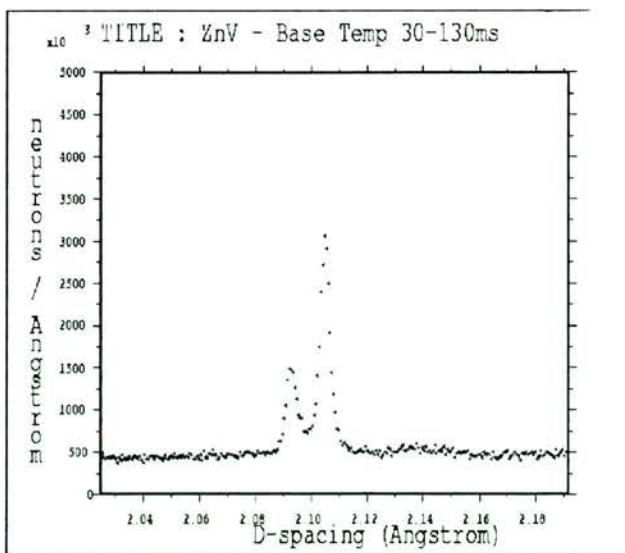


Figure 9. 5 shows an expanded view of the cubic (4,0,0) peak at 2.1Å splitting at 4K into the tetragonal (0,0,4) and (2,2,0) left and right respectively. (HRPD data).

Tetragonal, Space Group  $I4_1/amd$ , Fractional Coordinates:

Zn at  $x = 0$   $y = 0.25$   $z = 0.375$   
V at  $x = 0$   $y = 0$   $z = 0$   
O at  $x = 0$   $y = O(y)$   $z = O(z)$

[U =  $U_i/U_e \cdot 100$ ]

T(K)	$\chi^2$	a(Å)	c(Å)	Vol(Å <sup>3</sup> )	O(y)	O(z)	$U_{Zn}$ (Å <sup>2</sup> )	$U_V$ (Å <sup>2</sup> )	$U_O$ (Å <sup>2</sup> )
4	1.083	5.952045(18)	8.36984(4)	296.5170	0.52004(10)	0.23876(8)	0.606(31)	0.6	0.617(17)

**Table 9. 2 gives parameters extracted from the 4K neutron data refinement [ (vanadium thermal parameter not varied) tetragonal, space group  $I4_1/amd$ ].**

As can be seen from above, the observed data gives an excellent fit to the  $I4_1/amd$  model. This is taken to indicate that this model correctly describes the low temperature structure of  $ZnV_2O_4$ . Note that there is more of a problem in getting the intensity of the main peak in the above data to match the model than was found for the RT data. This may be explained in terms of this peak contains additional magnetic scattering at 4K. Thermal factors here are from neutron-only data and are not directly comparable with those obtained from combined neutron and x-ray data given above.

### 9.3 Transition

The transition from cubic to tetragonal form was known from Ueda's XRD work to occur at around 50K. Additional PND patterns were collected on HRPD at 1K intervals from 45K to 55K to allow this transition to be followed. The diffraction multi-plot (figure 9.6) below shows the evolution of this transition with temperature.

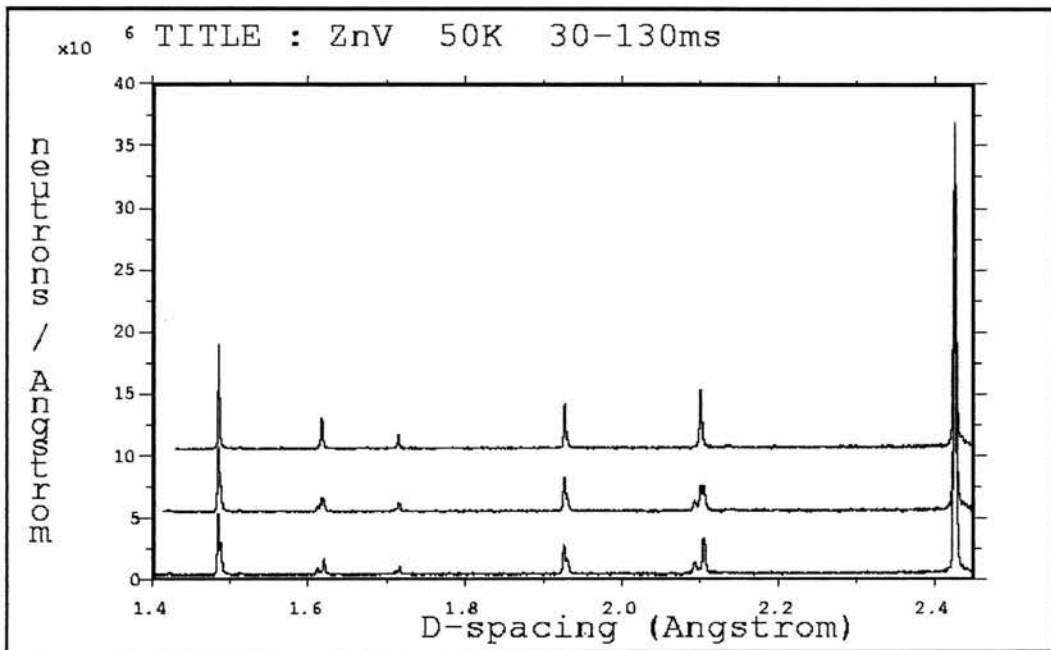


Figure 9. 6 shows HRPD histograms of ZnV<sub>2</sub>O<sub>4</sub> at 50, 51 and 52K bottom to top respectively.

This shows the transition to be rapid with respect to temperature, occurring over a single Kelvin, indicating that it is probably first order. Refinement of the patterns collected over the above temperature range, at 4K and at higher temperatures was carried out.

#### 9.4 $c < a$ Distortion – A Thesis

In 1997, Y. Yamashita and K. Ueda published a theoretical paper entitled “Spin driven Jahn-Teller distortion in the pyrochlore ZnV<sub>2</sub>O<sub>4</sub>”.<sup>75</sup> They argued that the distortion was too small to be accounted for by normal Jahn-Teller effects, that the stabilisation energy this implied was more of the order of magnetic stabilisation. Secondly, they showed that there was a small stabilising energy to be gained by lifting the degeneracy of the two d-electrons into orbitals of different energy. Finally, they proposed that the spin splitting energy and magnetic frustration on the B-site sub-lattice was the driving factor in stabilising the  $c < a$  structure. Whilst their

argument did not seem unreasonable, their point that the energy involved in this structural transition was too small to be a normal Jahn-Teller distortion seemed to be tenuous; seemingly ignoring the literature reporting a number of very small Jahn-Teller distortions wherein orbital ordering effects alone were proposed to be a sufficient driving factor for the distortions. Burdett specifically notes;

*“It is found experimentally that the ‘size’ of the ‘Jahn-Teller’ distortion varies wildly in the transition metal series. Sometimes it is very small and the molecule exists in a dynamic state around some sort of equilibrium geometry. Cooling the sample leads to a freezing out of the distortion. This ‘dynamic Jahn-Teller effect’ most often occurs where the orbital degeneracy is associated with an unsymmetrical arrangement of electrons in the  $\sigma$ -non-bonding orbitals (but involved perhaps in  $\pi$  interactions).”<sup>76</sup>*

Whilst Figgis notes:

*“The dynamic Jahn-Teller effect occurs when both (distorted) configurations are of lower energy than that of the undistorted octahedron, and the potential barrier for interconversion between them is small. ... Here, the time averaged position of the ligands may be very close to the regular octahedron.”<sup>77</sup>*

Secondly, Yamashita and Ueda assumed no spin-orbit interaction was present in their calculations. Nguyen and Goodenough note;

*“In an octahedral interstice, the  ${}^3F_2$  ground state of a  $V^{3+}$  ion is transformed to a  ${}^3T_{1g};t_2^2e^0$  configuration having a threefold orbital degeneracy. The cubic crystalline fields do not quench totally the orbital angular momentum; the orbitally three-fold degenerate manifold of  $t$  orbitals retains azimuthal quantum numbers  $m_l = 0, \pm 1$  associated with  $xy$  and  $yz \pm izx$  constituents referred to a tetragonal deformation or*

*the  $a_1$  and  $e_{\pm}$  constituents referred to a rhombohedral deformation of an elementary  $VO_6$  octahedron. The preferred deformation of the  $VO_6$  octahedron is rhombohedral. However, the sign of the deformation depends upon whether the Jahn-Teller deformation that removes the degeneracy quenches or enhances the orbital angular momentum.”<sup>78</sup>*

These comments are worth quoting at length as the pair of d electrons in the octahedral V(III) cation do occupy  $\sigma$  ~ non-bonding orbitals; additionally the direction of the observed distortion is not what one would expect from simple crystal field considerations alone. Thus Yamashita and Ueda’s assertions on both the size of the deformation, and assumption on a lack of spin-orbit coupling appear to be, at least, questionable. Nguyen and Goodenough produce a diagram in association with their comments given above, this is reproduced below for tetragonal deformations:

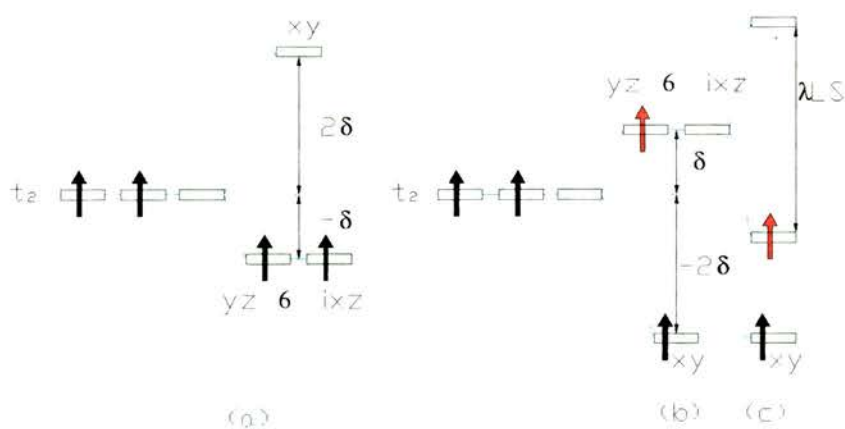


**Figure 9.7 (a) represents the  $c > a$  tetragonal deformation; while (b) shows the  $c < a$  variant, and (c)  $c < a$  including a second splitting due to an L-S coupling stabilisation energy (red electron), [after Nguyen and Goodenough].**

The observed  $c < a$  tetragonal distortion in  $ZnV_2O_4$  does suggest that form (b)/(c) is likely to reflect the electronic structure of the V(III) cations in this material. If the net stabilisation energy for (c), including a spin-orbit coupling contribution, is greater

than that observed for (a) then this will be the preferred distortion.

Assuming constant volume for both  $c < a$  and  $c > a$  distortions:

In (a) we note that there are 2 electrons both sitting at energy  $-d$  yielding a net stabilisation energy of  $-2d$ . In (b) we have one electron at  $-2d$  and one at  $+d$ , yielding a net stabilisation energy of  $-d$ .

Thus between (a) to (b); (a) is the preferred form.

The electron in (b) and (c) occupying the former  $xy$  orbital offers a stabilisation of  $-2d$ , thus where the energy of the second electron (red one in my diagram) falls below that of  $t_2$ , form (c) becomes preferred as a distortion. Clearly, the magnitude of  $\lambda L.S$  in (c) becomes critical. None of this is quantitative, however, we can see how the unexpected distortion could be stabilised.

From spectroscopic studies, Clark notes:

*“Under the influence of its spin-orbit coupling constant of  $\lambda = 105\text{cm}^{-1}$ , the magnetic moment of an octahedral vanadium(III) complex is expected to be appreciably dependent on temperature. However, all the complexes which have been studied over a temperature range have magnetic moments very close to the spin-only value at all temperatures, implying a large distortion of the ligand field from the octahedral.”*<sup>79</sup>

This is an interesting observation referring to V(III) complexes in the solution state and also to very dilute V(III) doped into solid alumina ( $\text{Al}_2\text{O}_3$ ). Plainly, the V(III) octahedron is distorted in the alumina structure and spin-orbit coupling is expected to be completely quenched; however in solution a small distortion may be much more difficult to observe. The spectroscopy indicates coupling but no structural effects are

observed in solution despite the spectroscopy. Given Burdett and Goodenough's commentaries on the suitability of a V(III) cation to show a dynamic Jahn-Teller effect, one is led to suspect that this vanadate spinel may be showing a dynamic Jahn-Teller effect in the cubic form, freezing out into a cooperative  $c < a$  distorted form, stabilised (in direction) by spin-orbit coupling at low temperature. The size of the observed distortion can then be justified on two grounds; firstly that these electrons are  $\sigma$ - non-bonding and offer little absolute stabilisation energy in either distorted form; and secondly, in that the energy difference between the  $c < a$  and  $c > a$  forms is likely to be very slight, the two providing competition suppressing a higher temperature transition. Only at low temperature, where the  $\lambda$ LS energy begins to become relatively significant to the overall energy of the material is the freezing out observed.

## 9.5 $c < a$ Distortion – Evidence of dynamic effects?

With the above in mind, we attempted to find physical evidence to support the dynamic Jahn-Teller contention. Were this effect to be present, one would expect it to be reflected as rapid variation in the V-O bond lengths. This would not, however, be directly observable on the timescale of a diffraction experiment. It would however introduce an element of uncertainty into the atomic positions of the vanadium and oxygen ions.

In refining these positions to both of the models used, both vanadium and zinc occupy special crystallographic positions, anchoring the model as it were; their positions cannot be varied in the refinement, however that of oxygen can. Uncertainty as to the position of these ions, and/or motion, is also reflected in their temperature (Debye-Waller) factors. Thus we look for some indication of abnormality in the Oxygen

position and in temperature factors extracted from diffraction data collected over a wide temperature range. Additionally, as the oxygen close packed sub-lattice forms the basis for the entire structure, abnormalities may be observed in the behaviour of the lattice parameter.

This experiment was carried out on a Bruker D8A diffractometer in reflection geometry, fitted with the prototype Oxford Systems Phenix closed cycle refrigerator [CCR] (helium). This was facilitated by R. Gover and J.S.O. Evans at Durham.

Scans were collected in the temperature range 20K to 230K in steps of roughly 6K. The CCR heat shields surrounding the sample were made from fine aluminium foil, and the sample itself mounted on an anodised aluminium disc. By far the largest diffraction peaks in the acquired patterns come from the aluminium. The aluminium foil served to filter out almost all of the vanadium x-ray fluorescence that has been a problem in other XRD measurements, but also served to reduce the overall intensity of the x-rays scattered from the sample. The patterns collected are shown in the multi-plot figures 9.8 and 9.9 below.

This data turned out to be relatively poor. Very little sample would adhere to the sample mounting stage (a circular aluminium plate), it also seems likely that some of the sample that was there was not held sufficiently well to the plate by the small amount of grease used for that purpose. The data may also be suffering from preferential orientation, this is seen in the peaks not having the expected relative intensity values (consistently across all temperatures). The reflection geometry of the diffractometer and lack of any sample rotation might only serve to enhance such a problem. It is noted though that the earlier room temperature data collected in the same diffractometer's furnace attachment shows no evidence of these problems. In

the latter case, the sample was not subject to the high vacuum, and thus one must suspect that the quantity of sample on the CCR mounting was the primary cause of these difficulties. Unfortunately it has not been possible to arrange to repeat this experiment (where steps are taken to ensure a greater volume of sample is under the beam). An application to acquire SRS beam time had earlier been rejected.

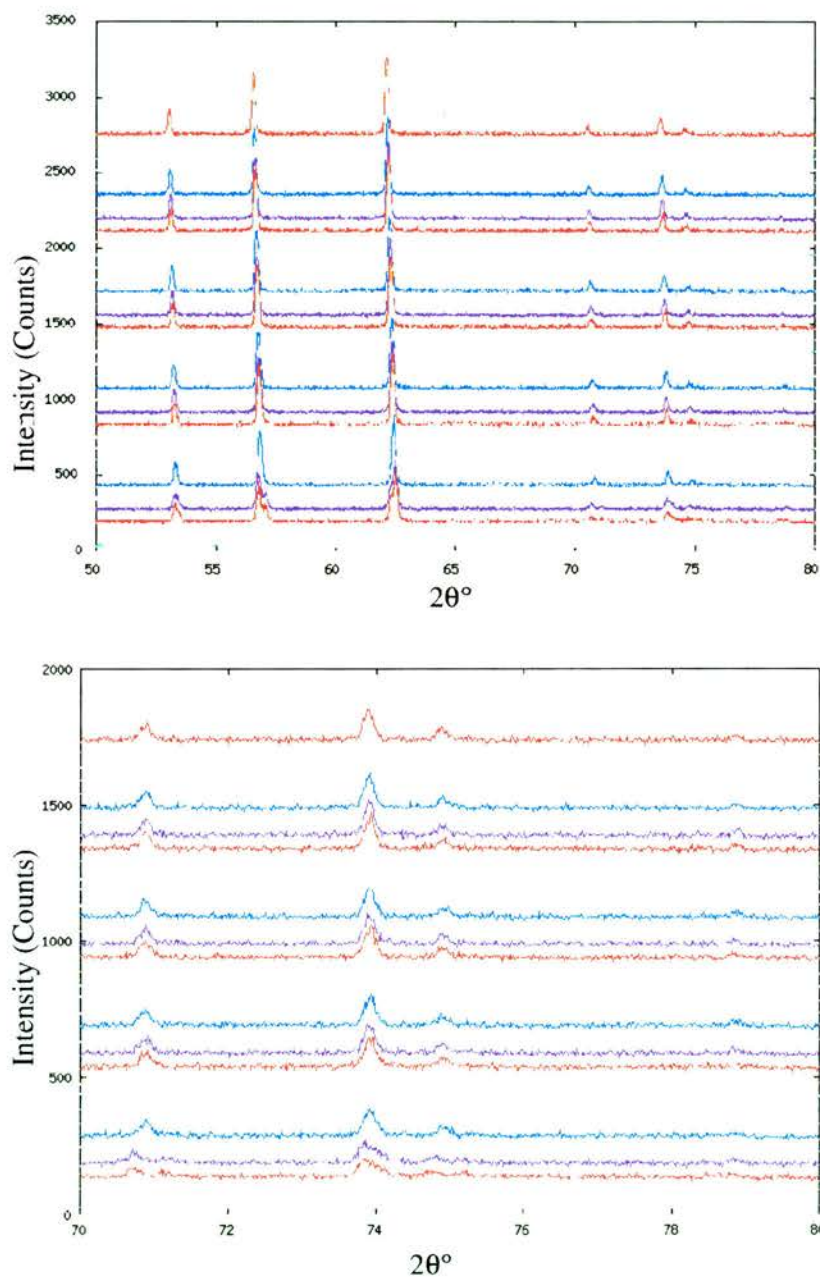


Figure 9. 8 & Figure 9. 9 show multi-plots of the D8a XRD datasets. The upper plot shows the region from  $50^\circ$  to  $80^\circ$   $2\theta$ , whilst the lower one expands the  $70^\circ$  to  $80^\circ$   $2\theta$  region. Temperatures run low to high from bottom to top. From 23K to 227K in approximately 6K intervals. The slight structural transition is seen best in figure 9.9 as the peak at c.  $54^\circ$   $2\theta$  splitting between datasets 5 and 6 respectively. The lack of sample volume and effect of the aluminium CCR heat shields is reflected in the relatively poor intensity of the scattering with respect to the background.

The relevant lattice parameters, thermal factors and the oxygen position were extracted from the data sets and are shown in the tables and plots below. The same scaling is used for each of the thermal parameter plots for ease of comparison;

Cubic, Space Group  $Fd\bar{3}m$ , Fractional Coordinates:

Zn at            x = 0.125            y = 0.125            z = 0.125  
V at             x = 0.5                y = 0.5                z = 0.5  
O at             x = O(x)              y = O(x)              z = O(x)

[U =  $U_i/U_e \cdot 100$ ]

T(K)	$\chi^2$	a (Å)	Vol(Å <sup>3</sup> )	O(x)	$U_{Zn}$ (Å <sup>2</sup> )	$U_V$ (Å <sup>2</sup> )	$U_O$ (Å <sup>2</sup> )
227	1.088	8.40305(9)	593.351	0.2629(8)	1.17(12)	0.96(11)	1.06(28)
221	1.116	8.40250(7)	593.237	0.2621(8)	1.07(25)	1.53(25)	0.62(34)
215	1.109	8.40230(7)	593.194	0.2625(8)	1.13(10)	1.4(10)	1.07(25)
209	1.110	8.40225(7)	593.181	0.2610(9)	1.21(10)	1.64(10)	1.04(25)
203	1.128	8.40211(7)	593.152	0.2621(8)	1.16(10)	1.4(10)	0.82(25)
197	1.068	8.40191(7)	593.108	0.2630(8)	0.84(9)	1.34(10)	0.45(25)
191	1.095	8.40184(7)	593.094	0.2623(8)	1.09(9)	1.37(10)	0.54(24)
185	1.120	8.40178(7)	593.081	0.2630(8)	1.06(9)	1.52(10)	0.49(24)
179	1.084	8.40165(7)	593.093	0.2626(8)	1.05(9)	1.45(9)	0.94(25)
173	1.087	8.40160(7)	593.042	0.2605(9)	1.11(9)	1.59(10)	0.92(24)
167	1.109	8.40141(7)	593.002	0.2632(8)	0.94(9)	1.37(10)	0.91(26)
161	1.077	8.40156(7)	593.034	0.2604(9)	1.03(9)	1.6(10)	1.02(24)
155	1.103	8.40148(7)	593.017	0.2622(8)	1.12(10)	1.45(10)	0.79(25)
149	1.106	8.40140(7)	593.002	0.2607(9)	1.14(10)	1.49(10)	1.45(25)
143	1.108	8.40112(9)	592.942	0.2627(8)	1.07(9)	1.4(10)	0.51(24)
137	1.100	8.40119(8)	592.956	0.2628(8)	1.05(10)	1.17(10)	0.36(24)
131	1.045	8.39946(18)	592.589	0.2613(8)	0.99(9)	1.43(10)	1.00(25)
125	1.064	8.40109(7)	592.935	0.2613(8)	0.96(9)	1.36(10)	0.91(24)
119	1.151	8.40118(8)	592.954	0.2607(9)	1.01(10)	1.32(10)	0.97(26)
113	1.162	8.40143(8)	593.007	0.2629(8)	1.15(10)	1.33(10)	0.96(26)
107	1.201	8.4014(8)	593.001	0.2606(9)	0.85(10)	1.37(11)	0.77(26)
101	1.187	8.40123(8)	592.964	0.2608(9)	0.92(10)	1.37(11)	0.85(26)
95	1.168	8.40136(8)	592.991	0.2605(9)	0.99(10)	1.39(11)	1.03(29)
89	1.172	8.40135(8)	592.99	0.2612(9)	0.98(10)	1.45(11)	0.87(26)
83	1.193	8.40112(8)	592.942	0.2623(8)	0.93(10)	1.31(11)	0.48(26)
77	1.211	8.40128(9)	592.975	0.2617(9)	0.99(10)	1.36(11)	1.01(27)
71	1.203	8.40135(9)	592.989	0.2616(9)	0.68(10)	1.24(11)	0.82(27)
65	1.207	8.40143(9)	593.006	0.2619(9)	0.69(10)	1.29(11)	0.72(27)
59	1.235	8.40143(9)	593.007	0.2613(9)	0.85(10)	1.32(11)	0.32(26)
53	1.233	8.40152(9)	593.027	0.2623(9)	0.56(10)	1.03(11)	0.55(28)

**Table 9. 3 Shows parameters extracted from refinement of the D8 XRD data in the Cubic regime space group ( $Fd\bar{3}m$ ).**

Tetragonal, Space Group  $I4_1/amd$ , Fractional Coordinates:

Zn at  $x = 0$   $y = 0.25$   $z = 0.375$   
 V at  $x = 0$   $y = 0$   $z = 0$   
 O at  $x = 0$   $y = O(y)$   $z = O(z)$

[ $U = U_i/U_e \cdot 100$ ]

T(K)	$\chi^2$	a(Å)	c(Å)	Vol(Å <sup>3</sup> )	O(y)	O(z)	$U_{Zn}$ (Å <sup>2</sup> )	$U_V$ (Å <sup>2</sup> )	$U_O$ (Å <sup>2</sup> )
47	1.182	8.37276(33)	5.95219(13)	296.635	0.5276(22)	0.2349(15)	0.50(11)	1.15(12)	0.33(28)
41	1.184	8.37045(31)	5.95276(13)	296.610	0.5270(22)	0.2389(15)	0.67(11)	1.13(12)	0.69(27)
35	1.183	8.37111(31)	5.95289(13)	296.646	0.5261(22)	0.2413(16)	0.7(11)	1.12(12)	0.51(27)
29	1.169	8.37029(32)	5.95301(13)	296.629	0.5279(21)	0.2391(15)	0.58(11)	1.52(13)	0.48(27)
23	1.162	8.36860(32)	5.95183(13)	296.451	0.5264(22)	0.2381(15)	0.52(11)	1.52(12)	0.76(27)

Table 9. 4 shows parameters extracted from refinement of the D8 XRD data in the tetragonal regime (space group  $I4_1/amd$ ).

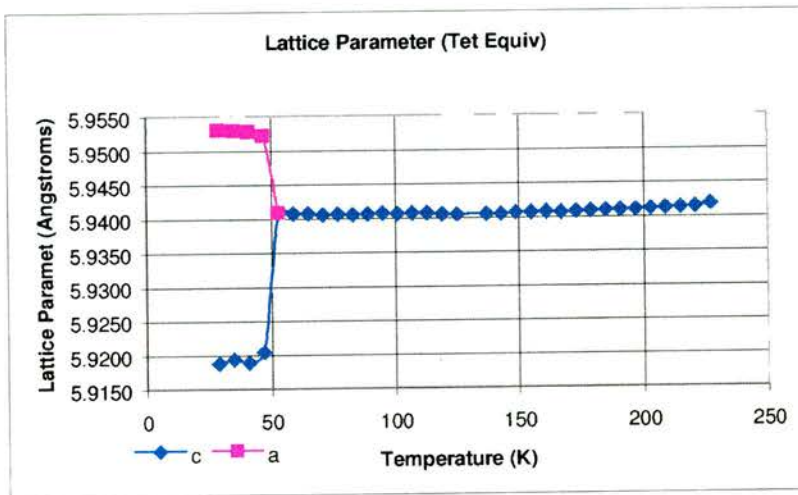


Figure 9. 10 shows the  $ZnV_2O_4$  lattice parameter across the measured temperature range. Note that for display purposes here, the c.8.4Å cubic lattice parameter is given in terms of its  $1/\sqrt{2}$  tetragonal equivalent c. 5.95Å. (Error range too small to scale for this figure, typical values seen below in fig. 9.11)

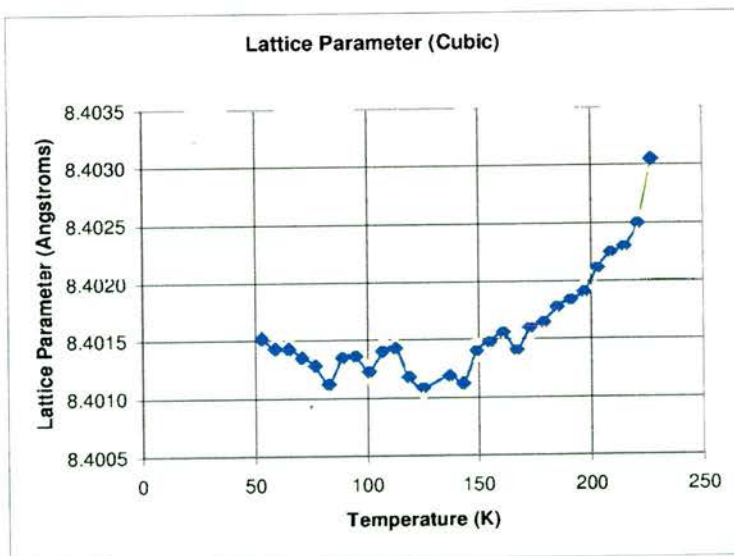


Figure 9. 11 shows the same data as 9.10 in the cubic regime from 53K to 227K, with the vertical scale expanded. Errors in Yellow. (scale cubic rather than tetragonal of 9.10) .

From 9.10 we see the structural transition clearly and get the impression that the lattice parameter is well-behaved above 53K. Expanding the scale however in figure 9.11, we might begin to question that latter contention. One would expect to see a smooth linear contraction of the cell parameter with reducing temperature, possibly noting something of an abnormality just around the structural transition. Instead however, there is a fairly linear region from the highest temperature to around 170K, a region between about 170K and 80K where the parameter varies in an odd fashion, followed by an increase between 80K and 53K (perhaps an expected anomaly heralding the observed transition). It is difficult to say what is going on from this plot, but it does appear that something is taking place; even allowing for experimental errors.

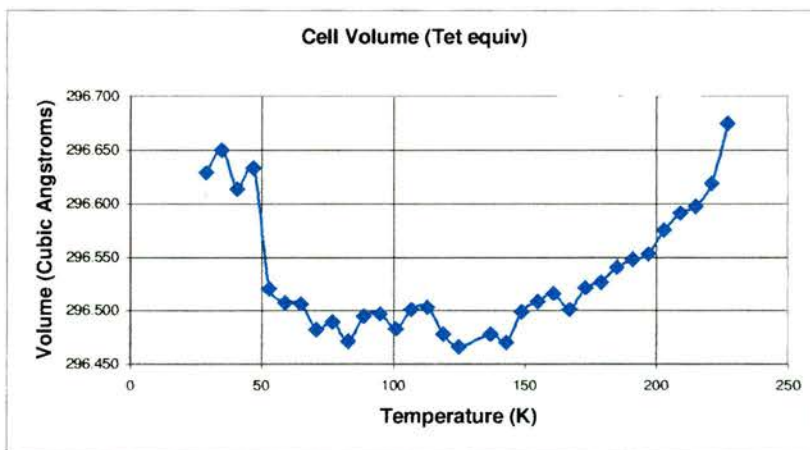


Figure 9. 12 Shows the cell volume (in tetragonal equivalent) across the temperature range. (Errors not shown: errors present c.  $\pm 0.01 \text{ \AA}^{-3}$ ), cubic versions of those shown in the lattice parameter fig. 9.11).

The cell volume (shown in figure 9.12), in the cubic regime (51K-227K), is simply the lattice parameter cubed and follows the same pattern. Across the 51K transition however we note that there is a slight but sudden increase in cell volume, corresponding to a reduction in the density of the material. This implies a reduction in the total energy per unit volume of the material.

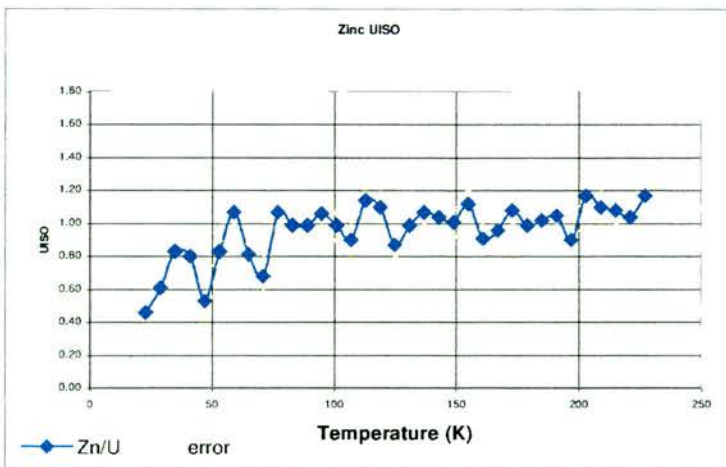


Figure 9. 13 shows the Zinc thermal parameter, (refinement error range in yellow).

Some scatter of the zinc thermal parameter is shown in figure 9.13, however there appears to be a gentle downwards trend, curve possibly, with decreasing temperature. This is consistent with the notion that the zinc ions reduce their amount of thermal induced motion with decreasing temperature.

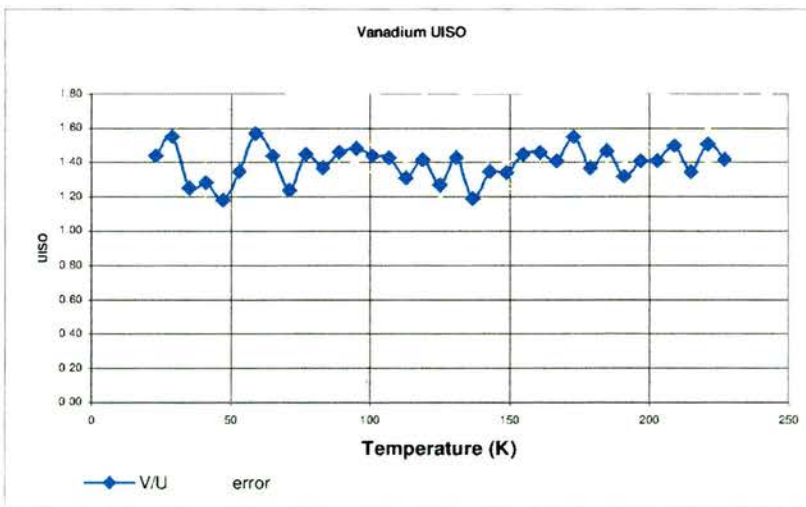


Figure 9. 14 shows the Vanadium thermal factor, (refinement error range in yellow).

The vanadium thermal factor is seen to behave in a different manner from that of the zinc (Figure 9.14). The general curvature/falling away of the zinc thermal parameter is possibly seen in the vanadium data; however, if it is, the fall-off is less rapid. It may be possible to split the vanadium UIISO behaviour into different regions. The

data below the 51K transition is not strictly comparable with that from higher temperatures as the vanadium is occupying a slightly different site. The  $c \ll a$  distortion of the octahedra will favour thermal motion in the “xy plane”, where cation-ligand distance is greater relative to distance in the  $z$  direction. As per the lattice parameter, there may be a region between 80K and 170K, behaviour above and below being different. Again, this is not entirely clear, but the data does not remove the suspicion that there is something unusual there.

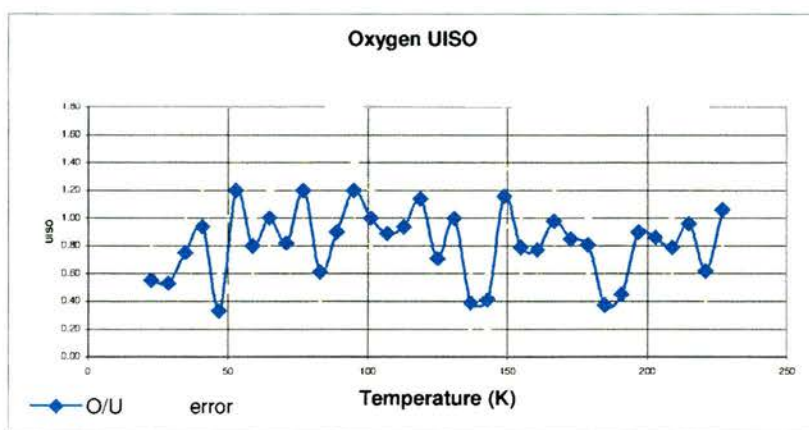


Figure 9. 15 shows the oxygen thermal parameter, (refinement error range in yellow).

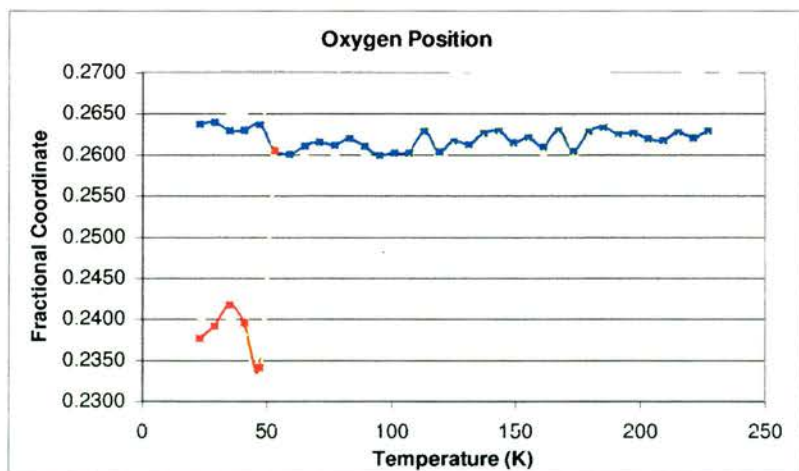


Figure 9. 16 shows the oxygen position (fractional coordinate  $x = y = z$  above 51K. Below 51K the oxygen has  $0,y,z$  coordinates. The  $y$  coordinate is  $c \cdot 2 \times$  the  $z$  coordinate. In this diagram, the red values indicate the  $z$  coordinate whilst the blue data points below 51K represent the  $y$  coordinate/2 (for scaling purposes). Refinement error range in yellow.

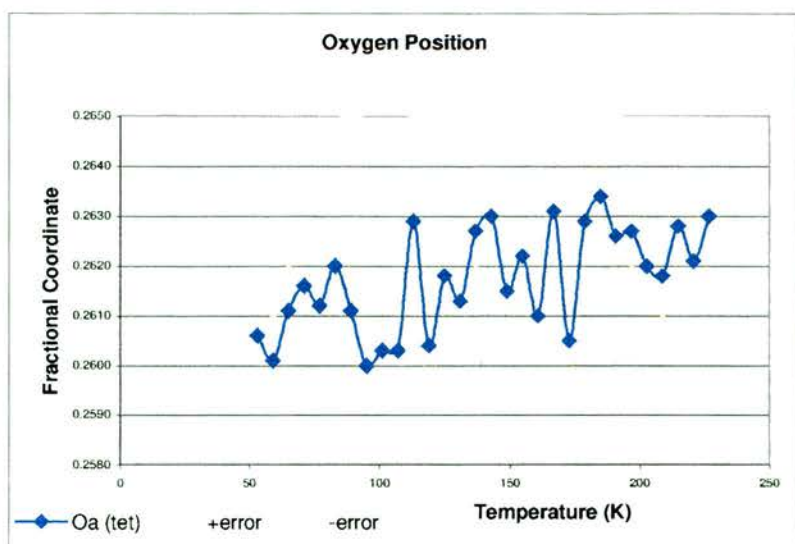


Figure 9. 17 shows variation in the oxygen position, (fractional coordinate), in the 50-227K range, reflecting the tilting of octahedra.

Figures 9.15 to 9.17 show considerable scatter in both the oxygen thermal parameter and the oxygen position (fractional co-ordinate). To some extent this scatter / uncertainty is probably due to the experimental technique's inherent ability "to see" oxygen ions relative to the other ions present. The range of observed oxygen coordinates multiplied by the cubic unit cell parameter ( $8.402\text{\AA}$ ), crudely gives a maximum shift of oxygen position of c.  $0.038\text{\AA}$ . There are no apparent trends however in that plotted data so that such a shift can be unambiguously discerned from random scatter / uncertainty. Similar comment can be made for the oxygen thermal parameter. As such, this data makes the suggestion that the oxygen position/thermal motion is uncertain to within the limit of this experimental data to tell us. It does not, however, show a smooth or predictable pattern and thus does nothing to dispel the contention that there may be unusual dynamics present.

Finally in this section, bond lengths and angles are looked at briefly. The above noted uncertainty in the oxygen position immediately introduces variation into the V-O bond lengths. Some of these parameters are plotted after explanatory diagrams are shown. Figure 9.20 shows the V-V bond lengths extracted from the refinements

across the temperature range; unsurprisingly, this resembles the plot of lattice parameters almost exactly.

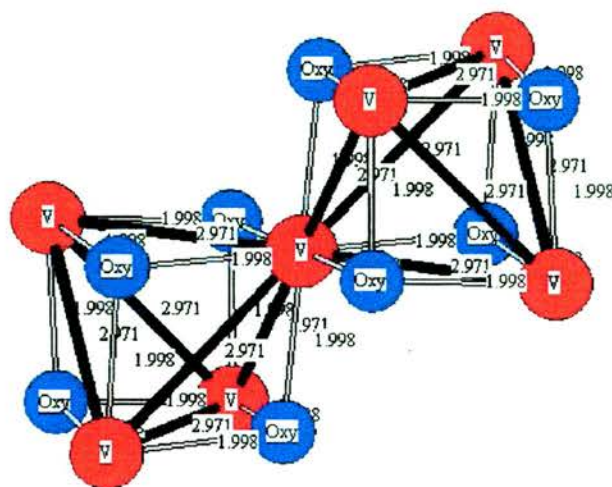


Figure 9. 18 shows a schematic of part of the unit cell of the  $ZnV_2O_4$  spinel in the cubic form at 227K, atom types labelled. No scale is implied to the relative atom sizes by their depiction. Two “vanadium tetrahedra” are clearly seen linked by a central vanadium cation. Bond lengths V-V at 2.971Å and V-O at 1.998Å are shown from refinement at 227K in the cubic form.

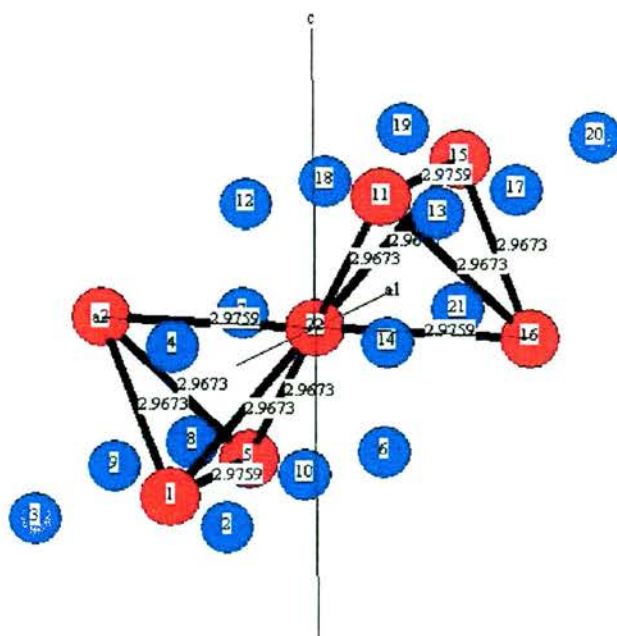


Figure 9. 19 shows the analogous plot of the tetragonal  $ZnV_2O_4$  spinel unit cell at 23K. Atoms are coloured as in 9.19 and numbered as a key for the bond angles/lengths noted in the table below. Two different “tetragonal” bond lengths are also shown in the figure. V-O bond lengths are omitted from this figure but given in the table to avoid further clutter. NB a2 = Atom 23, a2 refers to axis labels.

Bonds In Tetragonal Form @ 29K

Atoms		Distance		
V <sub>1</sub>	=>	V <sub>5</sub>	2.97650(6) Å	
V <sub>1</sub>	=>	V <sub>22</sub>	2.96792(6) Å	
V <sub>1</sub>	=>	V <sub>23</sub>	2.96792(6) Å	
V <sub>1</sub>	=>	O <sub>2</sub>	1.993(8) Å	Table 9.5a
V <sub>1</sub>	=>	O <sub>3</sub>	1.993(8) Å	
V <sub>1</sub>	=>	O <sub>4</sub>	2.0090(10) Å	
V <sub>1</sub>	=>	O <sub>9</sub>	1.993(8) Å	
V <sub>1</sub>	=>	O <sub>10</sub>	1.993(8) Å	

(Note Oxygen diametrically Opposite O<sub>4</sub> outwith above diagram's extents - equivalent bond from atom V<sub>23</sub> to O<sub>10</sub> = 1.993(8) Å)

Bond angle examples

V <sub>5</sub> -V <sub>1</sub> -V <sub>23</sub>	Angle:	59.90(0) °	
V <sub>22</sub> -V <sub>1</sub> -V <sub>23</sub>	Angle:	60.19(0) °	
V <sub>1</sub> -O <sub>4</sub> -V <sub>22</sub>	Angle:	94.2(4) °	
V <sub>22</sub> -O <sub>4</sub> -V <sub>23</sub>	Angle:	96.9(4) °	Table 9.5b
O <sub>2</sub> -V <sub>1</sub> -O <sub>4</sub>	Angle:	96.2(5) °	
O <sub>2</sub> -V <sub>1</sub> -O <sub>10</sub>	Angle:	96.5(5) °	
O <sub>3</sub> -V <sub>1</sub> -O <sub>2</sub>	Angle:	83.1(5) °	
O <sub>4</sub> -V <sub>1</sub> -O <sub>9</sub>	Angle:	83.9(4) °	

**Table 9. 5a & b Give bond lengths and angles in the tetragonal form at c.29K extracted from the D8 XRD data – subscript atom numbers refer to the atoms numbering in figure 9.19. Relevant cubic parameters are plotted in later figures, N.B. in the cubic state only one angle exists for each of the above pairs.**

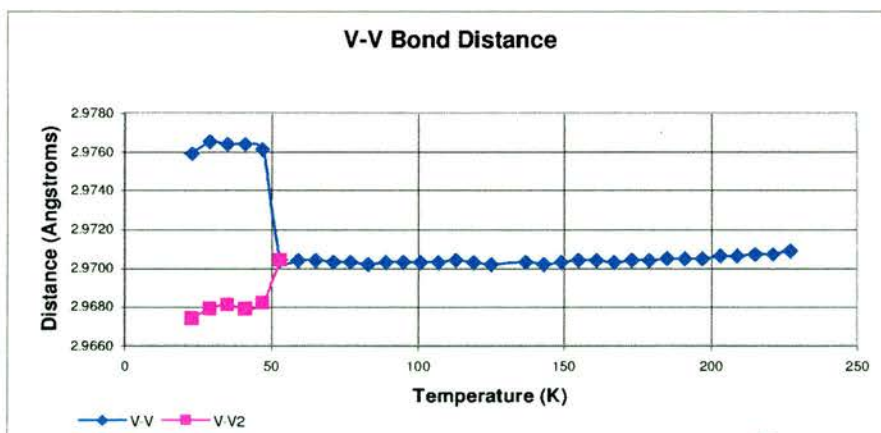


Figure 9. 20 shows the V-V bond length Vs. temperature. Errors are not visible in this scale, See table 9.5a and fig. 9.21 for typical values. (Outlying point at 131K removed).

Again, not surprisingly, expanding the 50-227K range resembles the equivalent lattice parameter plot.

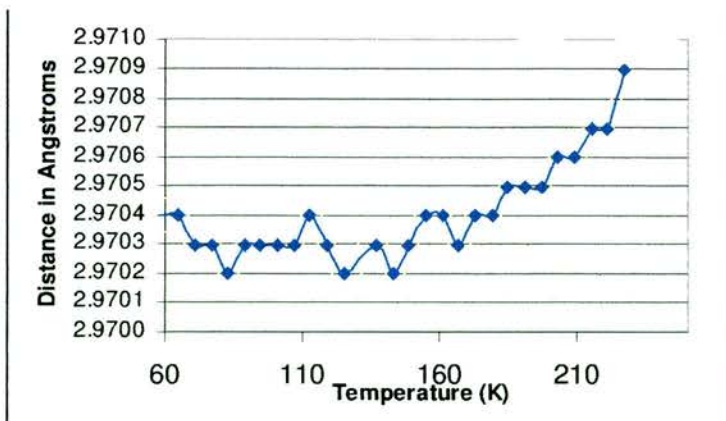


Figure 9. 21 shows the V-V bond length Vs. temperature (outlying point at 131K removed).

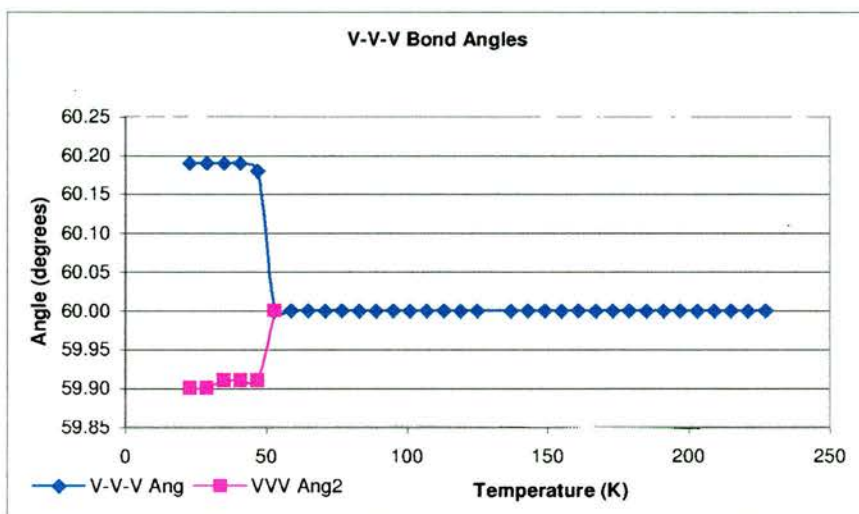


Figure 9. 22 shows V-V-V bond angles (outlying point at 131K removed. No errors returned by refinement – V cations on special sites, angle dependent on space group and lattice parameters only).

Above the transition, all V-V-V bond angles are 60°, reflecting the “perfect” tetrahedral network of vanadium ions. Below the transition two V-V-V angles are seen, however the difference between these angles (fractionally less than 0.3°) and V-V bond lengths (0.009Å) strongly emphasises the minute scale of this distortion of the B-site sub-lattice. From 227K to the distortion, the V-V bond changes length from c.2.9709Å to c.2.9703Å, spanning a range of some 0.0007Å (*in extremis*)

Turning to V-O bond lengths and V-O-V bond angles, figures 9.23-24 below show scatter (expected as per the oxygen position figure 9.17 above). Dropping from the 227K, approaching the 51K transition, there seems to be an increase in the V-O distance of c.0.02Å, this runs contrary to the expected general contraction of bond lengths expected as energy is removed. This increase is much larger than the decrease

observed in the V-V distances. As before, it might be possible to tenuously discern distinct regions above the structural transition, one from c.150K-227K and slightly longer bond distance regime between 150K and 50K.

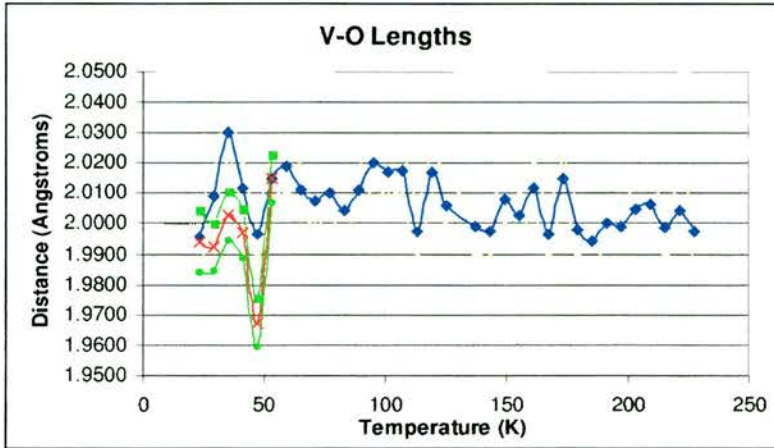


Figure 9. 23 shows the V-O bond distance in Angstroms. Yellow & green sets indicate errors, blue and red the data points.

V-O-V bond angles reflect the degree of tilt between adjacent VO<sub>6</sub> octahedra, this data is rather scattered, but there may be a reduction of c.1° between 227K and the transition.

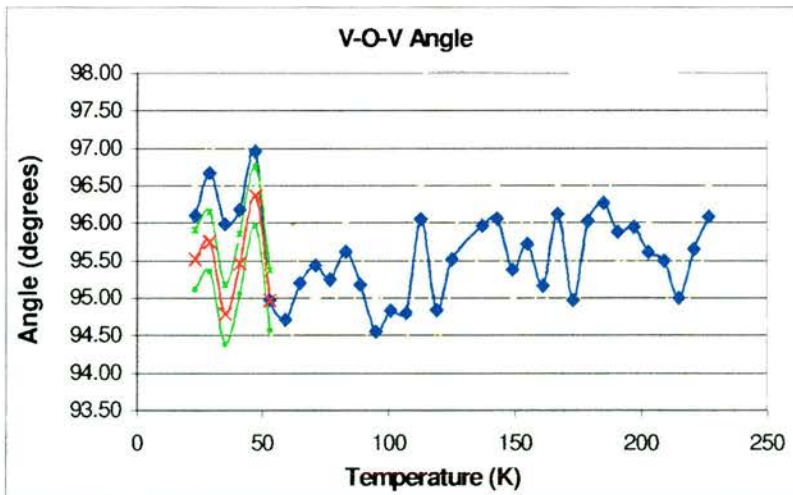


Figure 9. 24 shows V-O-V bond angles. (e.g O<sub>2</sub>-V<sub>1</sub>-O<sub>4</sub>) .

Data points above and below 51K transition in blue & red, errors in yellow & green respectively.

The two different O-V-O bond angles are plotted in figures 9.25 and 9.26 below.

These are mirror images of each other, the relevant angles being complimentary. As per the V-O-V angle we see scatter and a reduction/increase in angle of around  $1^\circ$ . Anomalies in several of these data sets are seen at around  $39\text{K} - T_N$ , this may indicate slight magneto-elastic effects arising coincident with magnetic ordering.

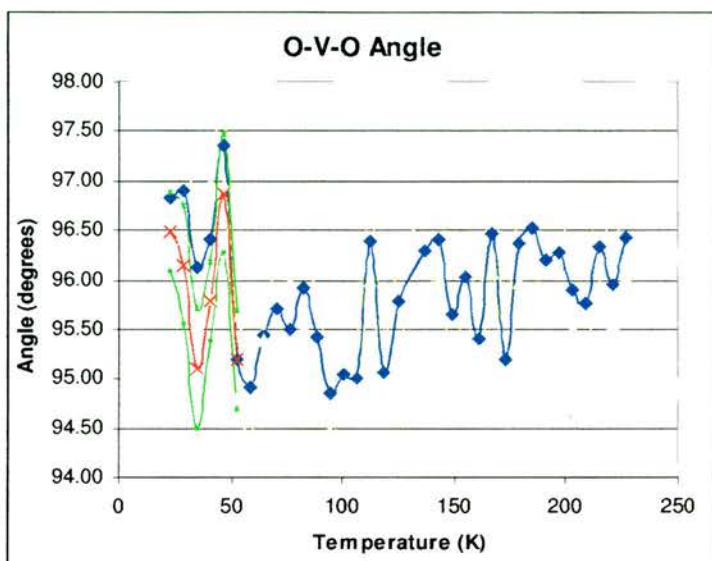


Figure 9. 25 shows one of the O-V-O bond angles.

Blue & red data points show the values above and below the 51K transition, yellow & green show errors. (NB errors constant across temp range covered)

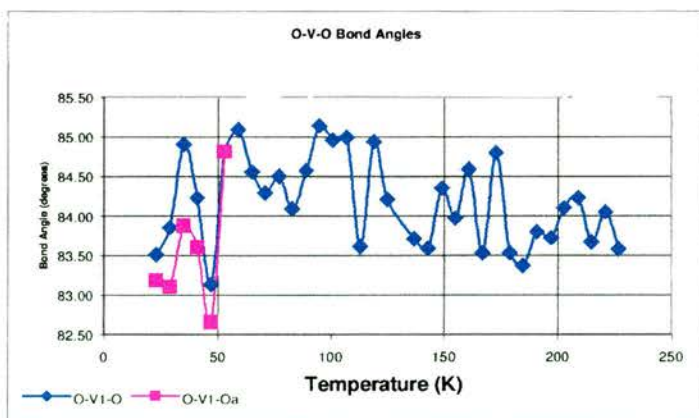


Figure 9. 26 shows another of the O-V-O bond angles. (e.g.  $O_3-V_1-O_2$   $O_4-V_1-O_3$ )

Errors complimentary to those shown in fig 9.25, omitted for clarity.

Analysis of low temperature HRPD neutron data yields thermal parameters broadly similar (given inherent difference in technique) to the x-ray ones for the zinc and oxygen ions. Effectively unable to see the vanadium cation in the presence of much stronger scatterers, no thermal parameters could be obtained for vanadium from the

neutron data. Extracted values for the zinc and oxygen are shown in figures 9.27 and 9.28 below.

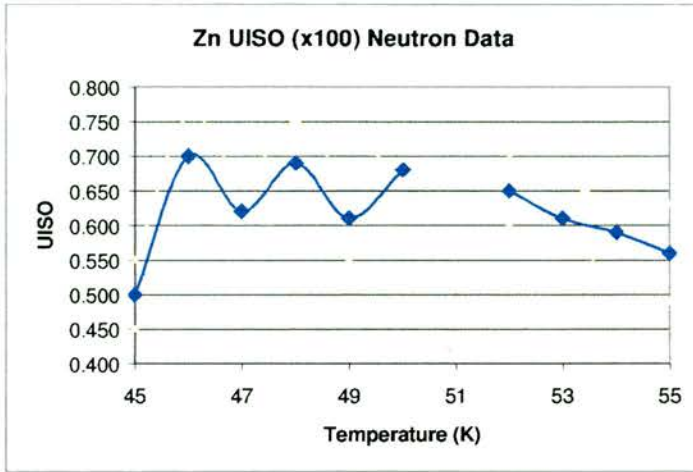


Figure 9. 28 shows zinc UIISOs extracted from HRPD neutron data across the 45-55K temperature range, (errors above and below in yellow).

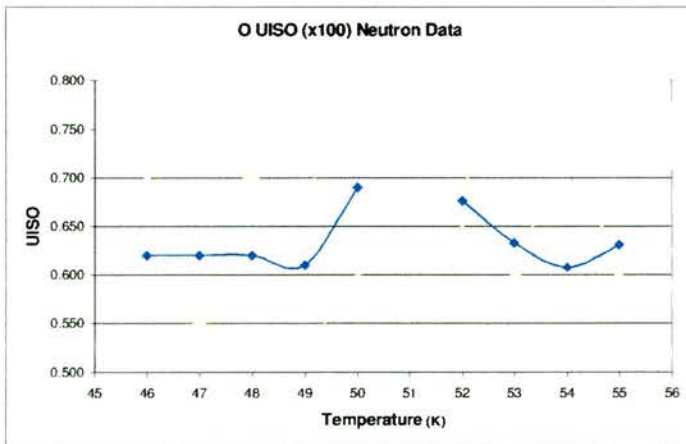


Figure 9. 27 shows oxygen UIISO\*s extracted from HRPD neutron data across the 45-55K temperature range, (errors above and below in yellow).

This data is limited in terms of the temperature range examined. It appears to show more uniform values, less variation than the x-ray data. However note the data point intervals, each of these whole neutron plots cover a range corresponding to two data points on the x-ray plots. No data was available at 51K that corresponded to the middle of the transition, this data could not be refined as both phases were present and GSAS could not balance the relative proportions of each and reach convergence.

## 9.6 Structure on Gallium / Lithium Doping

Doping of  $\text{ZnV}_2\text{O}_4$  with lithium and gallium is dealt with in a later section, however, some of the observations from that work are noted briefly here as they are useful to mention at this point.

Doping a small amount of gallium onto the V site in  $\text{ZnV}_2\text{O}_4$  suppresses the distortion to the tetragonal variant rapidly. This implies that the distortion is cooperative and strongly reliant on the V-sub-lattice; interruption of the V sub-lattice breaking up the cooperative effects. At a Ga concentration as low as 0.025% the distortion is completely suppressed.

Doping lithium for zinc has a similar effect, but requires larger dopant concentrations for complete suppression. Increasing lithium doping (for zinc) results in the increasing oxidation of V(III) to V(IV), but leaves the V sub-lattice intact. That this leads to the suppression of the distortion more slowly than that found for gallium doping further strengthens the cooperative argument. The V(IV) cation would not favour a dynamic Jahn-Teller effect, but is still capable of partially mediating it, until the V(IV) concentration is such that co-operation is weakened to local effects only. Whereas the Ga(III) cation's markedly different mass and lack of any formal d-electrons destroys cooperative effects through its site almost immediately.

## 9.7 Structural: Discussion and Conclusions

Having discussed some theoretical ideas and presented some experimental evidence, the case for deciding on the reason for the 51K structural in  $\text{ZnV}_2\text{O}_4$  is not made conclusively. From a theoretical perspective, we noted that the octahedral V(III) cation is expected to show spin-orbit coupling and also has good potential for

exhibiting a Dynamic Jahn-Teller effect.

The distortion is found above the spin-ordering temperature (see 9.2ff) and can thus be attributed to orbital-ordering effects rather than spin-ordering.<sup>80</sup> Nearest neighbour V-ligands appear to favour the  $c > a$  variant, however once L-S coupling is considered, should the spin-orbit coupling constant,  $\lambda L.S$ , be large enough, the potential for the greater stability of the  $c < a$  variant becomes apparent. Given that the electrons involved in the cubic degeneracy are  $\sigma$ -non-bonding, the degree of stabilisation by any cubic distortion is necessarily small, implying that  $\lambda L.S$  need not be very large to cause such a reversal in preferred structure. As these stabilisation energies are slight and the distorted state is so similar to the cubic form, this enhances the likelihood of a resonance state existing at higher temperatures, e.g. a dynamic Jahn-Teller effect.

The cubic  $3d^2$  cation is undoubtedly Jahn-Teller unstable, however the observed deformation seems unlikely to be of a *standard* Jahn-Teller type. Burdett describes a first order Jahn-Teller distortion as one where the direction of distortion is determined by crystal field effects from the bonding orbitals of nearest neighbour ligands. This is not always sufficient to differentiate between alternative deformations however; consider  $c < a$  and  $c > a$  for  $3d^4$  or  $3d^9$  cations: most often the  $c > a$  variant is seen, e.g. Cu(II)- $3d^9$ , yet from the first order consideration both  $a > c$  and  $a < c$  are of equal energy, and further consideration is necessary. In such a case, what Burdett describes as 2<sup>nd</sup> Order effects become important. One of these is the mixing of higher energy orbitals favouring one distortion over another; some statistical occupation of these excited states is sufficient to offer one option at lower energy than other possibilities. Whether this is or is not the case in  $ZnV_2O_4$  cannot be said without quantitative calculations beyond the scope of this work.

A second potential 2<sup>nd</sup> order effect is that of next-nearest neighbour ligand field effects - in this case the co-ordination of the vanadium cation to its neighbouring vanadium cations. This coordination induces a trigonal splitting of the central cation's orbitals and would indeed favour the  $c < a$  or rhombohedral deformations.<sup>81</sup> Electrostatic effects fall off with  $1/r^2$  and so this 2<sup>nd</sup> order splitting effect is a very small fraction of that of the immediate ligands, estimates suggest a few per cent at most.<sup>82</sup> Surveying spinels, the  $c < a$  distortion is only reported in the normal *simple* spinels  $ZnV_2O_4$  and  $MgV_2O_4$ . Other spinels showing this distorted variant are relatively rare, all have mixed B-sites and often magnetic cations on both A and B-sites – the range of possible interactions is much larger and they are much more complex. Ironically then, these relatively *simple* vanadate spinels, despite lacking such complications, prove no easier to explain. The rarity of other simple spinels showing this distorted variant emphasises the weakness of this particular 2<sup>nd</sup> order trigonal field splitting effect. Nevertheless, this does offer an additional slight pressure favouring the observed deformation.

The octahedral  $3d^2$  cation, shows a tendency towards this distortion type in other materials and environments at low temperatures, V(III) in several perovskites and Cr(IV) in  $CrO_2$ .<sup>83,84,85</sup> This latter observation tends to dispel the contention that the structural changes seen are directly spin-related. The low temperature deformation of Cr(IV) octahedra in  $CrO_2$  emphasises this as this material is ferromagnetic with a Curie temperature hundreds of Kelvin above the regime where the structural change is observed. In  $LaVO_3$ , Nguyen & Goodenough attribute the apparent reversal of the material's magnetism to orbital ordering effects, e.g. the spin component of the magnetism is following orbital considerations rather than the reverse.

For reasons to be explained in 10.2, extraction of  $\text{ZnV}_2\text{O}_4$ 's actual magnetic moment from magnetic susceptibility measurements in this temperature regime proves impossible. This makes estimation of the gyromagnetic ratio impossible and hence it becomes very difficult to ascertain absolutely whether or not spin-orbit coupling is present and significant by this method. A small amount of  $\text{ZnV}_2\text{O}_4$  was diluted in a UV/VIS reflective material and UV/VIS spectroscopy in reflection mode was attempted, the vanadate absorbed strongly across the entire frequency range, further dilutions simply weakened the featureless spectra, this yielded no useful results. Similarly, an ESR experiment failed to yield results. However, a step seen in magnetisation measurements coincident with the structural deformation but above the spin ordering/freezing temperature looks to correspond to a partial quenching of spin-orbit coupling.<sup>86</sup>

Analysis of the refined XRD data above is inconclusive, the data quality being not so good. The lattice parameter/V-V bond length behavioural data does appear to be abnormal in the region from c.130K to just above the 51K structural transition, which seems to imply unusual dynamics. Whilst some abnormality might be expected close to the transition, 100K above it seems unlikely. Were a dynamic Jahn-Teller effect present at high temperature, as the dynamics begin to slow down, this could be reflected as an abnormal looking thermal expansion/contraction before sufficient energy is lost from the system for a static cooperative deformation to freeze out. This odd behaviour of the lattice parameter and V-V bond lengths may be evidence for such dynamics.

General uncertainty in the oxygen position may arise from the experimental technique itself rather than from unusual dynamics of the oxygen; this is also reflected in the

scatter of the thermal parameter. Rather than conclusively confirming or rejecting the contention that unusual dynamics are present, this analysis suggests something of this nature may be present and encourages further study. Certainly, there is no indication from this that unusual dynamics are not present.

The spinel structure favours cooperative distortions, the tetragonal arrangement of the distorting B-site cations is not amenable to the production and gradual propagation of initially small distorted regions. In a sense this tetragonal B-site arrangement is as frustrated to orbital-ordering as it is to antiferromagnetic spin-ordering – and for the same geometrical reasons. It follows then that this frustration will reduce the temperature at which deformation is first seen; and once it reaches a temperature where the frustration can be overcome, the energetics will be such that all of the cations will wish to “turn” simultaneously. This sets such materials up for distortions occurring over a narrow temperature range. This is possibly the case in  $\text{ZnV}_2\text{O}_4$ , the deformation being seen to occur over a narrow temperature range.

Without spin-orbit coupling, the  $c < a$  deformed variant retains a degree of orbital degeneracy and is thus prone to further distortion. It remains possible that there is an exceptionally small additional distortion, possibly trigonal, which has not been observed in these studies. Which of the former  $xz$  and  $yz$  orbitals the 2<sup>nd</sup> electron couples to in the tetragonal form is unclear. The lack of a second deformation implies no ordering with respect to this. The  $z$  component of the wave function of both former orbitals is identical thus one might expect to see effects related to this uniform  $z$ -direction electron density. Conversely electron density disorder related effects could arise in the  $x$  &  $y$  directions. This is discussed later when magnetic measurements have shed some light on the matter.

Finally then in summary on structure, we suspect that above 150K a situation exists where spin-orbit coupling and a dynamic Jahn-Teller effect compete for dominance in determining the extant structure. In this temperature range, the dynamic effect dominates and an averaged cubic structure is observed with no apparent behavioural anomalies. Between around 150K and the cubic-tetragonal static deformation at c.51K, there is some evidence of odd behaviour, suggesting the dynamic effect is becoming less dominant and heading towards a freezing out. On the freezing the  $c < a$  deformed variant is of lower energy than the  $c > a$  variant due to a spin orbit-coupling plus crystal field stabilisation exceeding that of the  $c > a$  crystal field stabilisation alone.

## 10.0 $\text{ZnV}_2\text{O}_4$ : Magnetism

### 10.1 Introduction and summary of previous work

There are a number of published descriptions of magnetism in  $\text{ZnV}_2\text{O}_4$ . The origin of this study was in more general work on the  $\text{Li}_x\text{Zn}_{(1-x)}\text{V}_2\text{O}_4$  solid solution series. The extant published work on  $\text{ZnV}_2\text{O}_4$  had failed to fully explain the magnetic properties of this material, the term anomalous is seen several times in the literature. Further, some of said studies offered conflicting evidence / explanations.

The zero-field cooled and field cooled magnetic susceptibility plots for  $\text{ZnV}_2\text{O}_4$  were first published by Rudorff and Reuter in 1947<sup>87</sup> and are similar to that taken from our samples shown below in figure 10.1. This behaviour was later reproduced and published by Ueda *et al.* in 1997.<sup>88</sup>

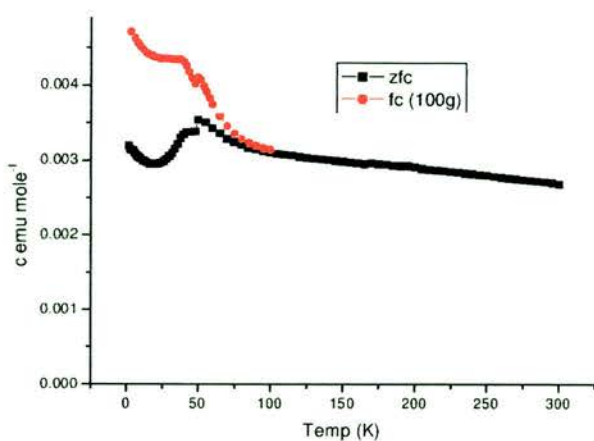


Figure 10. 1 shows zero field and field cooled (in 100G) susceptibility / magnetisation from sample ZnV1.

In 1973, Niziol carried out a neutron scattering experiment observing what they thought was evidence of magnetic Bragg peaks at 4K.<sup>89</sup> The plot he published is reproduced below in figure 10.2.

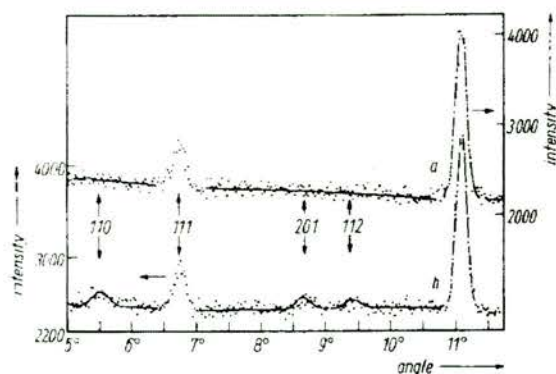


Figure 10. 2 shows Niziol's magnetic Bragg peaks?

As Niziol's plot shows, there is little intensity to the reported magnetic Bragg peaks and one might even question whether they have observed anything significant above background noise. This is more apparent if the black lines used to guide the eye are disregarded. This data was taken to imply that long range magnetic order was present in  $\text{ZnV}_2\text{O}_4$  and until this current work was carried out, this was the only published evidence of that *fact*. Recently (2002), Büttgen *et al.* carried out another neutron scattering experiment and found no evidence of long-range magnetic order.<sup>90</sup> This

latter work is wrong as will be shown presently. In Rudorff and Reuter's original work, they suspected that  $\text{ZnV}_2\text{O}_4$  might be metamagnetic, undergoing an antiferromagnetic to FM transition somewhere near 4K. This idea was later discounted by Niziol's 4K neutron work (FM would not break crystallographic symmetry giving antiferromagnetic like Bragg peaks). Although we don't believe the  $\text{ZnV}_2\text{O}_4$  is metamagnetic per se, our data will presently show why one could believe that might be the case. Ueda probably gave the best general summary of  $\text{ZnV}_2\text{O}_4$ 's magnetic behaviour to date in the paper where they mapped out the magnetic phase diagram for the  $\text{Li}_x\text{Zn}_{(1-x)}\text{V}_2\text{O}_4$  series.<sup>91</sup> Ueda broke the zero field-cooled/field-cooled susceptibility behaviour into several components:

1. A large temperature independent Pauli like susceptibility underlying the whole of the measured temperature range.
2. A region above 100K where the behaviour was essentially paramagnetic.
3. A region between 40K and 100K where cluster-like magnetic order was observed.
4. Finally, below 40K where long-range antiferromagnetic ordering was known (after Niziol).

Although he described the 40-100K region as above, it was also commented on that this region seemed to be anomalous.

Ueda looked at remnant magnetisation measurements in spin-glass like members towards the middle of the Li/Zn series, however remnant magnetisation in the parent  $\text{ZnV}_2\text{O}_4$  was not considered. This was not unreasonable as a regular fully ordered antiferromagnet would not be expected to show any significant remnant magnetisation. Ironically, this would prove to be one of the most interesting features

in the magnetic behaviour of  $\text{ZnV}_2\text{O}_4$ .

From this summary several questions worthy of further consideration arise. Why does a material that is known to be an insulator show such a large Pauli-like temperature independent susceptibility when that is a property of metallic materials? Considering the scant evidence for long range order, is the region below 40K really as described - an ordered antiferromagnet? What evidence exists for local magnetic clusters between 40K and 100K other than the divergence of zero field-cooled and field-cooled susceptibility plots?

## 10.2 Magnetic Measurements

The majority of measurements presented here were collected from a sample named "ZnV2". This was the sample described above and examined in detail in the chapter on structure. A smaller number of measurements were collected from an earlier sample "ZnV1". Both of these samples were seen to show the same susceptibility behaviour. During other syntheses, samples were made whose room temperature lattice parameter did not agree with the expected value of c.8.41 Å (after Ueda). Both slightly doped variants and these *mis-firings* show significant changes in their susceptibility behaviour relative to that of the parent material. This observation serves thus two purposes. Firstly, it shows the sensitivity of the parent spinel to compositional disorder. But secondly, suggests that the form of the magnetic susceptibility is the most reliable test of sample integrity. In particular, the structural transition at 50-51K is very sensitive to composition, this should be reflected as a relatively sharp step in susceptibility. A marked broadening of this feature or a change in the temperature at which it is seen indicates a potential problem with the sample.

### 10.3 Zero field cooled susceptibility

Data obtained from our own measurements are shown in figure 10.1 above. Several attempts were made to fit this data to a modified Curie-Weiss Law to extract the temperature independent component (TIP), Weiss temperature ( $T_w$ ) and a Curie constant ( $C$ ). This proved to be impossible, the TIP,  $C$  and  $T_C$  parameters were found to be completely interdependent. The region between 200 and 400K from a later measurement was taken to be paramagnetic, its reciprocal plotted against temperature and a linear fit used to extract  $T_C$ .

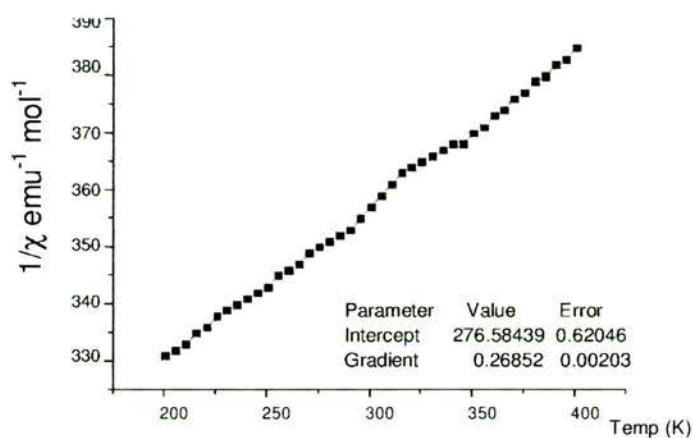


Figure 10. 3 shows the reciprocal of  $\chi$  plotted against temperature and a linear fit of the same taken from sample ZnV2.

Solving the linear fit of the 200-400K susceptibility data yields Weiss temperature of  $-1032\text{K}$ , repeating the exercise for sample ZnV1 over a 200-300K temperature range yields a Weiss temperature of  $-1010\text{K}$ . This Weiss temperature is exceptionally large implying the presence of strong antiferromagnetic correlations and is markedly enhanced by the inherent geometric frustration of the B-site sub-lattice. Muhtar *et al.*, reported a Weiss temperature of around  $-990\text{K}$ .<sup>92</sup> Other published values include  $-600\text{K}$ <sup>93</sup> and  $-420\text{K}$ <sup>94</sup>. The table below, taken from Baltzer *et al.*, shows some antiferromagnetic spinels for comparative purposes,<sup>95</sup> these apparent vanadate Weiss temperatures are the highest of any spinel recorded.

TABLE I. Magnetic and crystallographic properties of antiferromagnetic spinels.

Composition	Lattice parameter $a$ , Å	* parameter	Néel temp. $T_N$ , °K	Curie-Weiss $\theta$ , °K
MgV <sub>2</sub> O <sub>4</sub>	8.413 <sup>a</sup>	0.385 <sup>a</sup>	45 <sup>b</sup>	-750 <sup>b</sup>
ZnV <sub>2</sub> O <sub>4</sub>	8.410	...	...	-600 <sup>a</sup>
ZnMnCrO <sub>4</sub>	8.35	...	...	-268
CdMnCrO <sub>4</sub>	8.620	...	...	-95
ZnCr <sub>2</sub> O <sub>4</sub>	8.328	0.387	16 <sup>b</sup>	-392 <sup>d</sup>
CdCr <sub>2</sub> O <sub>4</sub>	8.596	0.396	9 <sup>a</sup>	-83 <sup>f</sup>
MgCr <sub>2</sub> O <sub>4</sub>	8.333 <sup>e</sup>	0.385	15 <sup>b</sup>	-350 <sup>b</sup>
ZnCr <sub>2</sub> S <sub>4</sub>	9.988	0.385	<20 <sup>b</sup>	+18 <sup>g</sup>
ZnCr <sub>2</sub> Se <sub>4</sub>	10.500	0.384	20 <sup>b</sup>	+115 <sup>h</sup>
ZnFe <sub>2</sub> O <sub>4</sub>	8.416	0.380	10	-1(1)
CdFe <sub>2</sub> O <sub>4</sub>	8.704	0.386	...	-22.2
GcFe <sub>2</sub> O <sub>4</sub>	8.411 <sup>i</sup>	0.375 <sup>i</sup>	10 <sup>b</sup>	-15 <sup>b</sup>
GcCo <sub>2</sub> O <sub>4</sub>	8.317 <sup>k</sup>	0.375 <sup>k</sup>	20 <sup>b</sup>	+90 <sup>b</sup>
GcNi <sub>2</sub> O <sub>4</sub>	8.221 <sup>k</sup>	0.375 <sup>k</sup>	16 <sup>b</sup>	0 <sup>b</sup>

<sup>a</sup> Reference 3.  
<sup>b</sup> Reference 8.  
<sup>c</sup> W. Rüdorff and B. Reuter, Z. Anorg. Allgem. 253, 177 (1947).  
<sup>d</sup> Previously reported to be -250 in Ref. 8.  
<sup>e</sup> Reference 2.  
<sup>f</sup> Independently reported to be -88 in Ref. 2.  
<sup>g</sup> R. J. W. Verwey and E. L. Hellmann, J. Chem. Phys. 15, 374 (1947).  
<sup>h</sup> Reference 9.  
<sup>i</sup> A. Arrott and J. R. Goldman, Bull. Am. Phys. Soc. 30, 62 (1933).  
<sup>j</sup> A. Durif-Varsatzen et al., Ann. Chim. 1, 525 (1956).  
<sup>k</sup> E. C. Romelia, Philos. Res. Rept. 8, 304, 321 (1953).

Figure 10. 4 Shows a table of selected antiferromagnetic spinels their respective Néel and Weiss Temperatures.

Using the extracted Weiss temperature as a constant we fit the susceptibility to a modified Curie-Weiss model and to extract a Curie constant. The model used is :

$$\chi_M = \frac{C}{T + T_W} + TIP$$

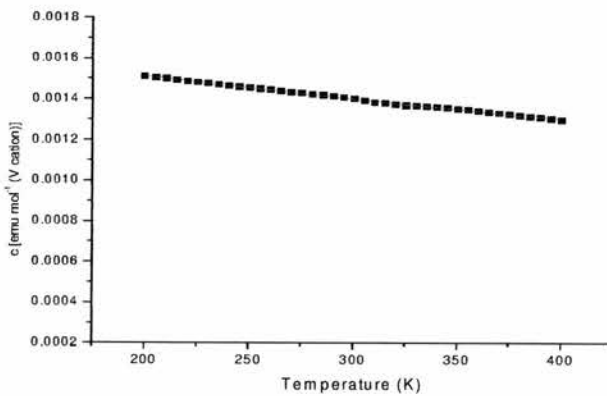


Figure 10. 5 shows a fit of the ZnV2 susceptibility data to a modified Curie Weiss law model (note change of scale, molar data values halved to give magnetisation per V cation).

Where  $\chi_M$  is the measured susceptibility, C is the Curie constant,  $T_W$  is the Weiss Temperature and TIP is a temperature independent component.

The results of this fitting are given in table 10.1.

TiP (emu mol <sup>-1</sup> )	C	T <sub>w</sub> (K)	R <sup>2</sup>
3.29 x 10 <sup>-7</sup>	1.866	-1020	0.99836

**Table 10. 1 shows fitted values for TiP, C and T<sub>w</sub> over the noted temperature range.**

From the expression for the Curie constant,  $C = \frac{N\mu_B^2 P^2}{3k_t}$ , the effective moment per vanadium cation (where this is defined as P), was determined using the extracted Curie constant. This yielded an effective moment of **3.863μB** per vanadium cation.

Ashcroft and Mermin<sup>96</sup> quote typical values for P for the V(III) cation as follows :

P(calc) = g[J(J + 1)] <sup>1/2</sup> Spin orbit coupled	P(calc) = 2[S(S + 1)] <sup>1/2</sup> Spin only value	P(experimental) Spin orbit quenched
1.63μB	2.83μB	2.8μB

**Table 10. 2 shows values of P taken from the noted literature.**

It is seen that the extracted vanadium moment exceeds the possible value, this was also noted by Muhtar *et al.* who struggled to find an explanation for this feature. Mamiya & Onada found that fitting data 500-1000K yielded a T<sub>cw</sub> of -420K, implying a substantially reduced moment. (Van Vleck corrections were calculated by Muhtar *et al.* but were found to be insignificant on the scale of the raw data).

From Figure 10.5, which is on a reduced scale, we see that the fitted susceptibility is essentially linear, thus in fact we are fitting 3 parameters to a straight line. Fitting a 3-parameter curve to what is almost a straight-line results in an almost complete interdependence of those parameters.

Returning to the raw data for a moment, looking at the data in the 200-400K region (re-plotted in figure 10.6), the linearity of this region becomes immediately evident.

The observed “susceptibility” is composed mainly of a linear temperature dependent term, with possibly a slight Curie curvature superimposed on top of that.

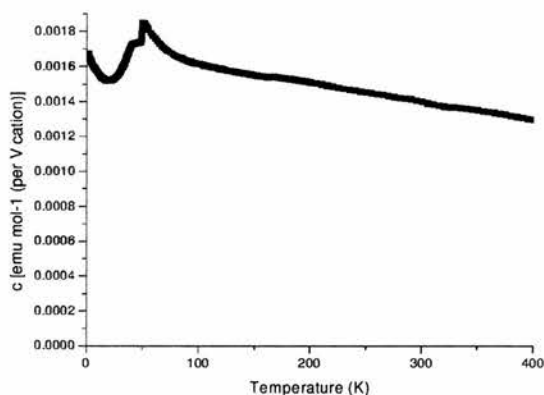


**Figure 10. 6 Shows the raw zero field-cooled susceptibility of ZnV<sub>2</sub>O<sub>4</sub>.**

The material does not appear to be showing reasonable Curie-like behaviour in the 200-400K temperature range; one concludes that modelling of this data is of very suspect value and values obtained thus must be treated with caution. The question then arises as to where the large Weiss temperature and linear temperature dependency of the susceptibility comes from.

Some enhancement of the Weiss temperature is expected from the inherent geometric frustration of the tetrahedral vanadium sub-lattice, however this geometric component should have is no significantly greater effect than that found in ZnCr<sub>2</sub>O<sub>4</sub>. The degree of geometric frustration is equal in the equivalent structures. Indeed this material shows a smaller lattice parameter (shorter M-M distances) and a larger spin only moment; one might reasonably expect that the strength of the frustrated antiferromagnetic interactions would be greater, rather than less, leading to a higher T<sub>W</sub> than that found in ZnV<sub>2</sub>O<sub>4</sub>. It does not, the observed ZnCr<sub>2</sub>O<sub>4</sub> Weiss temperature is -392K, less than half of the ZnV<sub>2</sub>O<sub>4</sub> value.

In studies on titanate spinels (parent, reduced and doped  $\text{LiTi}_2\text{O}_4$ ), Harrison, Edwards & Goodenough used an additional term in modelling of their susceptibilities, their model being of the form:<sup>97</sup>

$$\chi = \frac{C}{T + T_c} + f(T) \quad \text{where, } f(T) = A_M + B_M T$$

e.g. there is a 2<sup>nd</sup> linear temperature dependant term being used. It was suggested that  $A_M$  accounted for temperature independent contributions such as a Pauli and diamagnetic contributions, the  $B_M T$  term was described as being a temperature dependent enhancement to the Pauli susceptibility caused by:<sup>98</sup>

1. Electron-electron or electron-phonon interactions.
2. The presence of quasi-particles such as large polarons of spin-paired dimers.
3. The materials they were looking at were metallic however or very close to a compositional metal insulator transition. Hence band formation giving the basic Pauli susceptibility.

There is little point however in fitting the observed data to an expression such as the one above, insufficient curvature in the data to fit an expression with 4 variables. Indeed the parameters extracted from a 3 variable expression are sufficiently interdependent to make them of suspect value.

$\text{ZnV}_2\text{O}_4$  is insulating according to the literature and some cursory measurements carried out during this work, it's room temperature resistance is quoted as  $2 \times 10^5 \Omega$  and Goodenough estimates the V-V separation is too great for direct vanadium  $t_{2g}$ - $t_{2g}$  overlap and hence metallic band formation.<sup>99, 100</sup> Nevertheless, a compositional metal-

insulator transition is found in the  $\text{Li}_x\text{Zn}_{(1-x)}\text{V}_2\text{O}_4$  series between  $x = 0.3$  &  $0.4$ , inferred from Seebeck coefficients.<sup>101</sup> Thus the material lies reasonably close to a metal-insulator transition. It seems plausible that an extremely narrow band might exist, possibly on the verge of complete localisation. Were this to be the case, then a Pauli contribution would be expected which might be temperature dependent. Temperature dependence in the sense that marginal changes in lattice parameter with temperature will have a greater effect on the degree of band formation relative to that where greater overlap is already present. Even were the material not actually metallic, close proximity to a metallic state may lead to some form of incipient behaviour resembling the same.

The mentioned titanates, however, undergo no collinear ordering, their susceptibility remains Curie like (including this additional temperature dependent term) to much lower temperatures than is seen in this vanadate. At lower temperature, more of the Curie like curvature of the susceptibility data is available for modelling, allowing them to make a reasonable attempt to deconvolute the two temperature dependent terms. With the vanadate, the structural transition and collinear ordering remove much of the curvature from the data available for fitting, preventing such modelling.

In  $\text{ZnCr}_2\text{O}_4$ , each of the  $t_{2g}$  orbitals is singly occupied, thus there is no orbital degeneracy or susceptibility.  $\text{ZnV}_2\text{O}_4$  is quite different in that respect. The triply degenerate pair of d-electrons in an isolated  $\text{V}^{3+}$  cation have six possible combinations of orbital occupancy which satisfy the exclusion principle and Hund's rules. In the absence of an applied field the six possible combinations might be expected to be randomly occupied. In a field however that changes. If, for sake of example, we choose an applied field parallel to the cation's z-axis, we introduce an

orbital Zeeman splitting of any orbital with a z directional component. In such a case, each of the xz and yz orbital pairs are split into higher and lower energy levels. The xy orbital is unaffected (though any electron in these orbitals will experience greater torque than one in the others). It follows that the two d-electrons will tend to want to occupy the lowered yz and xz orbitals. The field induces a single lower energy state. The degree of occupation will be  $k_B T$  dependent and possibly linearly so in the given temperature range. Were this to be correct, then more of the electrons' moment could be drawn into the applied field direction than would be expected were they randomly distributed in the orbitals – giving a pseudo-Pauli susceptibility. This would result in a larger measured magnetisation than expected and hence give the impression of a larger effective moment than is actually present.

The introduction of an additional linear dependent term to the high temperature susceptibility could have the observed effect on the Weiss temperature and extracted moment, deconvoluting this from the normal Curie behaviour is impossible, as both are temperature and field dependent.

Both explanations offered involve orbitals, either on isolated vanadium cations or in the combination of orbitals to form a conduction band. Uncertainty over the actual effective moment precludes us from determining whether or not the two electrons are spin-orbit coupled but it seems likely that orbitals are in some way related to the material's observed magnetic properties ~ from the more plausible Edwards / Goodenough / Harrison / Lambert explanation. As noted in the section 9, we recognise that spin-orbit coupling is possible due to orbital degeneracy and the orbitals in which the electrons reside pointing away from the oxygen anions that would quench such coupling. Specifically Goodenough states, "*In an octahedral*

interstice the  ${}^3F_2$  ground state of a free  $V^{3+}$  ion is transformed to a  ${}^3T_{1g}$ :  $t_2^2e_0$  configuration having threefold orbital degeneracy. The cubic crystalline fields do not quench totally the orbital angular momentum.” Further, “it [ $V^{3+}$ ] is biased already to  $|\delta/\lambda|^2$  in favour of a local deformation which preserves the orbital angular momentum, where  $H_i = 0$ .”<sup>102</sup> Where  $\delta$  is a term scaling the stabilisation due to a non cubic distortion,  $\lambda$  is a term scaling the stabilisation due to spin orbit coupling and  $H_i = 0$  means above a magnetic ordering temperature [no ordered internal field splitting orbital energy levels].

Orchard makes several interesting comments related to a situation analogous to that found in  $ZnV_2O_4$ :

“Where  $L$  is only partially quenched in the ground state, there is normally a first order multiplet splitting, moderated in varying degree by the effect of Jahn-Teller and other) distortions. In general, the fine structure exhibited by the ground term involves energy spaces comparable to the Boltzman Energy  $kT$ , with the result – whatever the detail - that  $M_{eff}$  is itself a function of temperature and the dependence of susceptibility on temperature correspondingly complex.”<sup>103</sup>

In other words, there are likely to be significantly populated low-lying excited states at all except the lowest of temperatures, considerably complicating any consideration of the magnetic moment or susceptibility. This is interesting with relation to thoughts on the titanates above, a possibility not considered in the mentioned papers. With reference to Jahn-Teller effects Orchard notes:

(Where a measure of L-S coupling is retained), “Ordinarily such a complex will be simultaneously susceptible to Jahn-Teller distortions of some kind, these two effects

*(J-T and L-S coupling), invariably in conflict, commonly have a marked influence of paramagnetic properties, especially their temperature dependence.”<sup>104</sup>*

And dynamic Jahn-Teller effects specifically:

*“But the Jahn-Teller effect has also, and more fundamentally, a dynamic aspect: in general the effect is about vibrational-electronic (vibronic) interactions, i.e., the breakdown of the Born-Oppenheimer approximation.”<sup>105</sup>*

And:

*“When the ground state of a complex is Jahn-Teller unstable, the detailed analysis of its magnetic properties by any static model of the ligand field may sometimes be little more than a useful analogical device of uncertain physical validity.”<sup>106</sup>*

Although Orchard is referring to magnetically dilute chemical complexes rather than solids, the essence of the ligand field effects and L-S coupling considerations remain valid, being a function of the immediate environment of the cation. If anything, the concentration of magnetic species in a solid further complicates matters, when the *more simple* case of the chemical complex is found to be so complicated, encountering difficulties with the solid is perhaps to be expected.

We conclude from this consideration of the literature and our own attempts to fit the above experimental data that the actual vanadium moment cannot be determined in the temperature range we have investigated using magnetic susceptibility measurements. The potential complications noted offer a range of possible causes for the unrealistic extracted moment and our inability to fit the data to a simple modified Curie-Weiss law.

## 10.4 “Diamagnetic” Measurements

The data set shown plotted below measures the zero field-cooled remnant magnetisation of  $\text{ZnV}_2\text{O}_4$ , effectively we are measuring the spontaneous magnetisation of the zero-field cooled sample using no measuring field. Although this is an odd measurement to make it has some importance in the context of spinels. Many antiferromagnetic spinels are known to show parasitic ferromagnetism arising from incomplete moment cancellation. Our measurement suggests that zero-field cooled  $\text{ZnV}_2\text{O}_4$  is diamagnetic in the absence of an applied field. This measurement eliminates spontaneous parasitic ferromagnetism as a source of influence on other measurements.

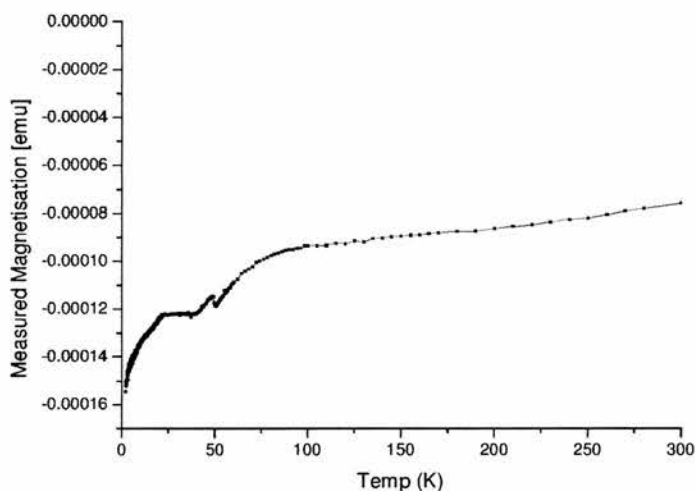


**Figure 10.7**  
“Diamagnetic”  
measurement (note  
magnetisation scale  
is negative  
throughout).

Absolute values are suspect as no subtraction was made to account for the diamagnetic sample holder materials, thus no particular scaling was carried out. This measurement may have partly failed insofar as the diamagnetic plot largely mirrors the features in the zero field-cooled susceptibility plot. Whether this really reflects changes in diamagnetism with temperature, or whether fields associated with either the squid detection circuitry or remnant fields from the SC magnet are sufficient to

superimpose a tiny applied field signal on top of the diamagnetic one is unclear. (Remnant SC magnet fields are quoted by Quantum Design as being typically less than 1 gauss). This measurement was checked many times during the latter part of its execution to ensure that the instrument was fitting the correct part of the measured signal – no problem was found. However, one would think a tiny applied field measurement superimposed over a diamagnetic signal ought to reproduce a tiny zero field-cooled plot rendered negative by its addition to a negative term. The fact that it is mirrored rather than simply lowered below the zero susceptibility axis inclines one to suspect that the sample was mis-centred and the instrument was fitting the signal on the wrong part of the I/R plot. That the measurement was checked repeatedly during its execution and appeared to be measuring correctly is odd. As this type of measurement is not commonly made, other than on spontaneous ferromagnets that produce a very different result, no comparative data on other materials was found.

Above 100K, the measured “diamagnetic” signal remains slightly temperature dependent. This may reflect another characteristic of an almost metallic material.

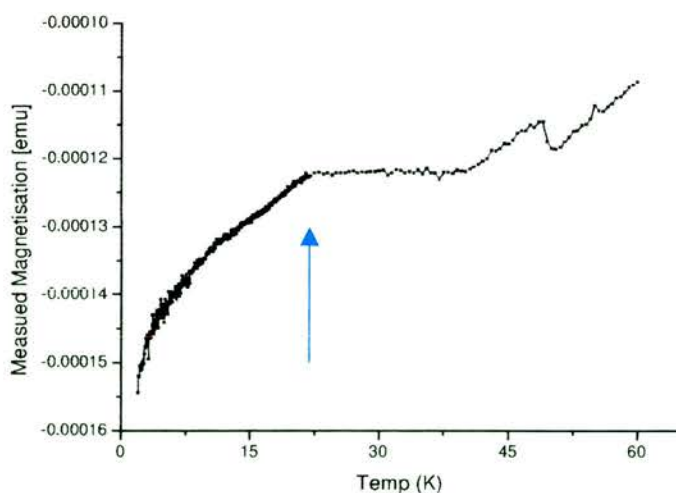


**Figure 10. 8 expands the low temperature region of the “diamagnetic” measurement, the change in experiment temperature intervals is marked approximately by the blue arrow.**

Of particular note is the low temperature region of this measurement. On writing the measurement programme, temperature intervals of 0.025K were accidentally specified rather than the 0.25K intended. The 0.025K measurement proceeded overnight until the programming error was spotted the following morning. At this point the programme was aborted and restarted using the intended value, continuing on from the temperature at which the original run was aborted. This change in measurement rate produced a strange result.

The measured (dia-)magnetisation flattened out over a range of about 15 Kelvin then began its miniature negative mirroring of the zero field-cooled susceptibility. Why changing the rate of measurement should have such an effect is unclear. Irrespective of what is actually being measured here, this does indicate that even at very low temperatures, below an ordering temperature and in the absence of any significant field, there is still some sort of very slow temperature dependent spin dynamic present in this sample.

The temperature region below about 22K does not mirror that of the zero field-cooled susceptibility plot – this may also indicate that even the most minute of measuring fields are having a measurable effect on the sample. Alternatively, if the conjecture that the mirroring effect indicates a mis-measurement and we are actually measuring a tiny (inverted) applied field zero field-cooled susceptibility added to a diamagnetic background is correct, then the region below 22K if inverted may correspond to a tiny spontaneous ferromagnetic component.

## **10.5 M/H sweeps**

The  $\text{ZnV}_2\text{O}_4$  sample was subjected to M/H sweeps at a range of temperatures to

examine its field dependent behaviour. The results of this experiment are shown in the plot below.

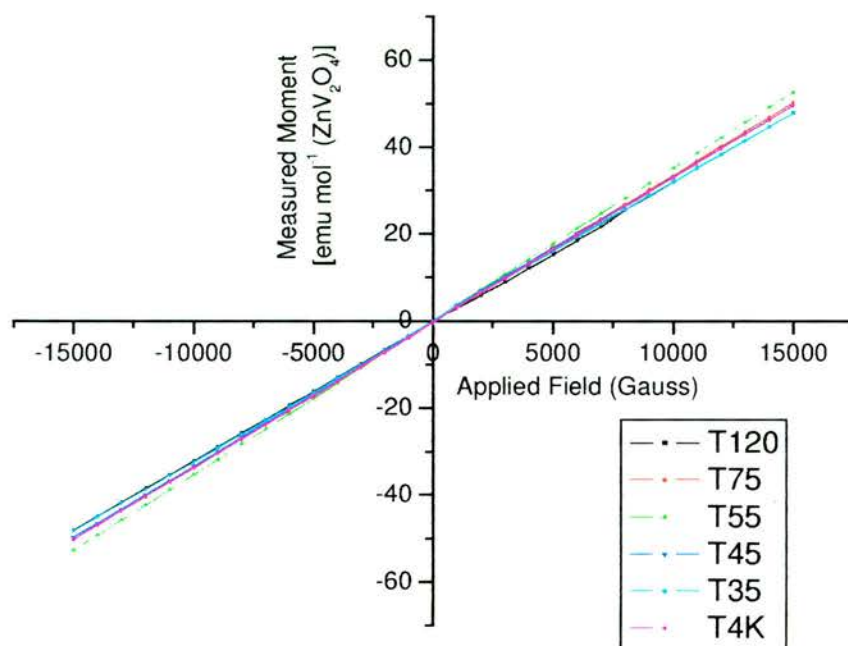


**Figure 10.9** shows M/H sweeps at a range of temperatures

The multi-temperature plot shows that the sample's magnetisation is essentially proportional to the applied field. Relatively little temperature dependence is observed. No coercive field is measured other than a vanishingly small value at 4K. There is no sign of the magnetisation beginning to saturate at any temperature in fields up to 1.5T. In a second measurement at 4K, taking smaller field intervals and expanding the region around the plot's origin, shows a very slight hint of hysteric behaviour in the sample. A maximum coercive field is estimated at around 0.5 Oe, this may be nothing and questioning the ability of the instrument to measure to that accuracy might be wise. This is shown in figure 10.10 below.

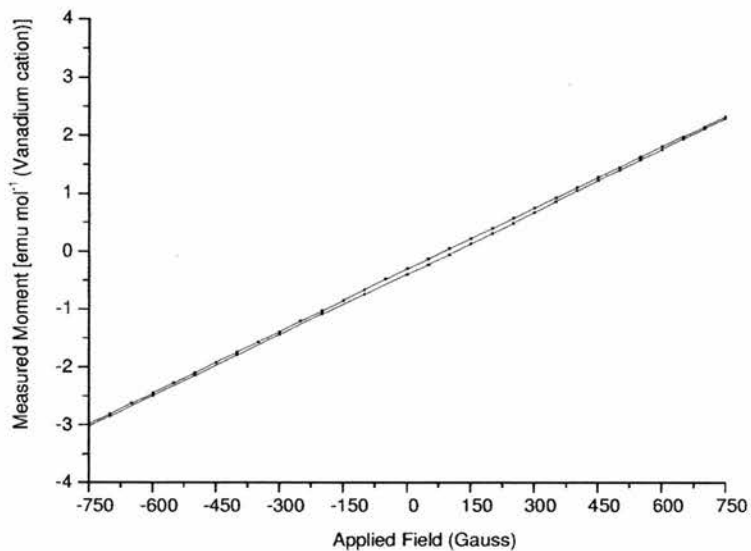
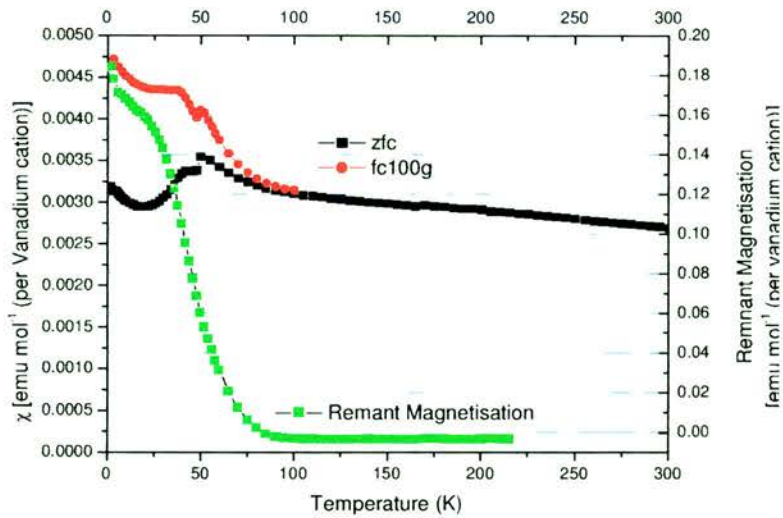


Figure 10. 10 shows a section of an M/H sweep taken at 4K

These measurements become interesting in the context of the field induced remnant magnetisation and remnant magnetisation decay measurements. They show clearly that any induced magnetisation is very weak, having no effective resistance to an applied field. This may also have some bearing on the comments concerning field sensitivity in the diamagnetism section. There appears to be an extremely small offset to the zero centring of the M/H loop in figure 10.10 above. This is a characteristic of a spin glass, however in this case, the offset is so small that it may simply be an experimental error and carry no significance at all.

### 10.6 Field cooled Susceptibility in $ZnV_2O_4$

The plot below shows zero field-cooled, field-cooled susceptibilities and the remnant magnetisation for  $ZnV_2O_4$ . In this measurement the zero field-cooled and field-cooled data were collected using an applied field of 100G. The same field was used for field cooling in both the field-cooled run and the remnant magnetisation measurement. Remnant magnetisation is measured in zero field.



**Figure 10. 11 shows the zero field-cooled and field-cooled susceptibilities and remnant magnetisation for  $ZnV_2O_4$ , (100G used as applied cooling and measuring field). Remnant magnetisation plot uses the scale to the right.**

The most apparent observation from figure 10.11 is surprising amount of remnant magnetisation for a normal antiferromagnet. As the material is cooled in a field from a paramagnetic state, the applied field will lower the energy of magnetic electrons aligned with it relative to that of other orientations, thus more electrons will be found in that state than otherwise. Below the temperature at which the rate of spin fluctuations collapses, e.g. a Curie, Neel or glass temperature, this has the potential to result in a freezing-in of some of that induced order. In a bulk antiferromagnet one would expect that the majority of electrons would overcome the applied field and take part in the cooperative antiferromagnetic ordering. However, some proportion are expected to remain *stuck*, as it were, outwith the bulk ordering. As these have been aligned to some extent by the cooling field prior to their freezing, cumulatively they result in a slight net magnetisation of the sample – and can be observed in the remnant magnetisation measurement. Regions which have a net magnetisation are termed uncompensated. Visual inspection of figure 10.11 suggests that rather than the limited amount of uncompensated magnetism that should be present in an ordered bulk antiferromagnetic, there is a very considerable amount of induced net magnetisation. This observation leads to several possible conclusions:

1. The small applied cooling field is strong enough to disrupt or prevent bulk antiferromagnetic ordering.
2. There is more than one magnetic component present in the material leading to the simultaneous observation of more than one type of behaviour.

Further evidence will tend to support the last theory.

In general (though there are more exotic possibilities), an ability to field induce a substantial amount of remnant magnetisation into a material, describes that material as either a permanent ferro or ferri-magnet, or a spin glass. As the first two of these options should show significant hysteresis in the M/H experiment, they are discounted. Thus  $\text{ZnV}_2\text{O}_4$  appears to be showing an unexpected spin glass-like characteristic. This idea was then tested further. Firstly, by cooling the sample in a number of different applied fields and measuring its field-cooled susceptibility using the same applied field.

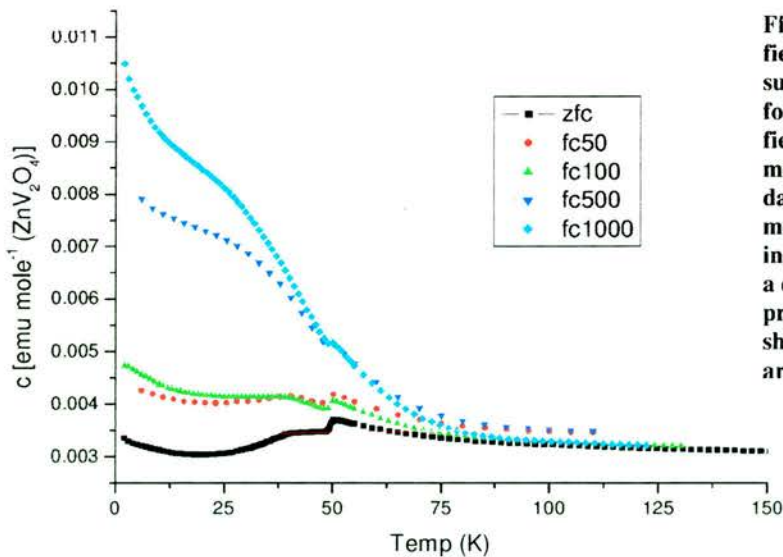


**Figure 10. 12 shows zero field-cooled susceptibility and susceptibility measurements following various applied field coolings, all were measured in 100G. Note the data for the 50G and 500G measurements were collected in a separate experiment with a different sample mass, probably explaining the slight shift in absolute values. Data are as otherwise collected.**

Figure 10.12 shows that the sample's observed magnetic properties are extremely sensitive to applied fields, particularly on cooling. The step corresponding to the structural transition is seen at 50K in all of the plots and this does not appear to be influenced by applied fields. The ability of the material to show cooling field induced magnetisation is striking. An almost complete change in the form of the measured curve is observed for cooling fields of 500G or larger. However, a peculiar observation is made when the sample is cooled in a much larger field.

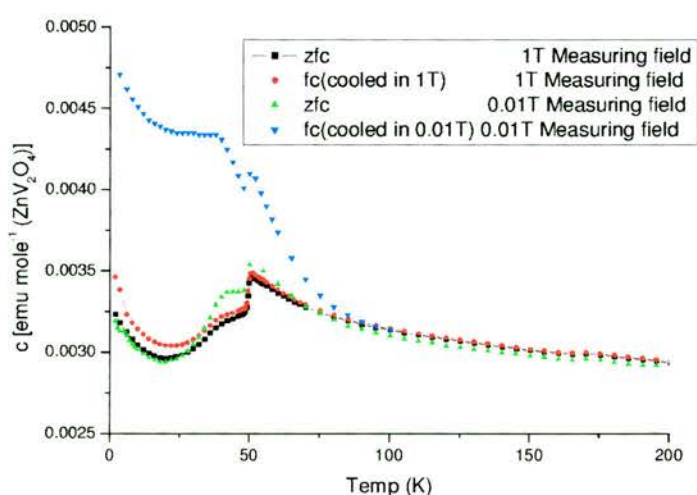


**Figure 10. 13 show ZnV<sub>2</sub>O<sub>4</sub>'s susceptibility behaviour when the sample is cooled and measured in 1T compared with cooling and measuring the sample 0.01T.**

In the 1 Tesla cooling and measuring case, zero field-cooled and field-cooled plots show very little difference until the Neel temperature is reached at 39K. This may be explained in terms of the large measuring field being sufficient to induce broadly the same effect whether or not the sample has been cooled in it. But that both behave more like the low field zero field-cooled case than any of the intermediate cooling field plots is intriguing.

In figure 10.13, it seems that the step in susceptibility corresponding to the structural transition may be larger in the 1T measuring field case. However this is an artefact due to the small number of data points in the 0.01T data set. A set with more data

points is used in figure 10.14 below.

Goodenough thought this step mirrored that in some of the orthovanadate perovskites, it resulting from a quenching of at least some of the orbital moment on the structural transition.<sup>107, 108</sup>

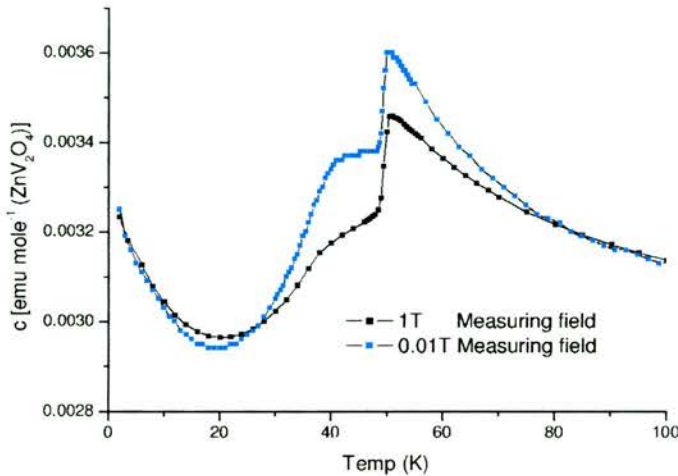


**Figure 10. 14 shows the susceptibility measurements 0.01T and 1T measuring fields after zero field cooling, expanding the region around the structural and collinear ordering temperatures.**

Looking at the expansion of the region around the transitions for the 1T and 0.01T measuring fields after zero field cooling, we also note a marked change between the shape of the data sets between the 51K structural transition and the 39K Neel Temperature. We see that the 0.01T field appears to reach a shallow maximum flattening off at 39K, while the 1T field case shows an inflection in downwards slope rather than a maximum. Also the maximum susceptibility reached just before the 51K structural transition is greater in the lower field measurement. A larger field effecting a reduction in susceptibility implies some measure of field dependent resistance to the applied field. A spontaneous reversal of magnetisation is reported in LaVO<sub>3</sub>, associated with an orbital ordering effect, but this is related to a structural transition at a given temperature, whether it is show field dependence is unknown.

In section 10.9, it is shown unambiguously, by the appearance of magnetic Bragg

reflections, that 39K is the Neel temperature. Thus the difference in susceptibility data between the high and low measuring field is intriguing. The change in curvature gives some indication that the large field is possibly interfering with the ordering process. The transition appears to be smeared somewhat from the susceptibility data.

## 10.7 Remnant Magnetisation

Having field cooled the sample in 1000G to 4K, the field was removed and the sample heated to 10K, magnetisation was then measured at 15 minute intervals to investigate the behaviour of the remnant magnetisation over time at constant temperature. The field cooling process was repeated the sample heated to 60K and the measurement repeated.

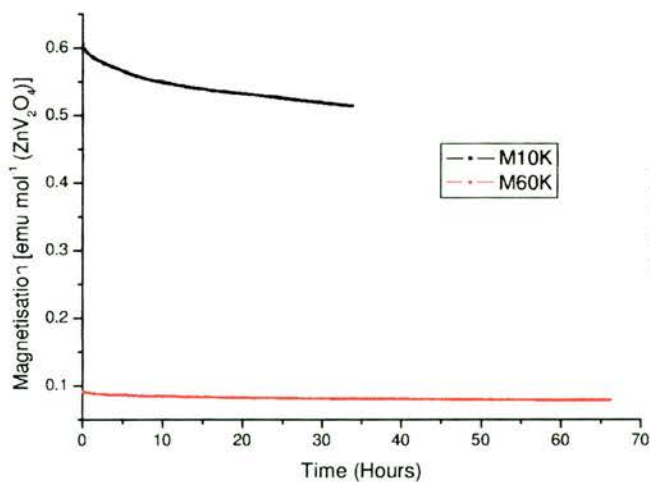
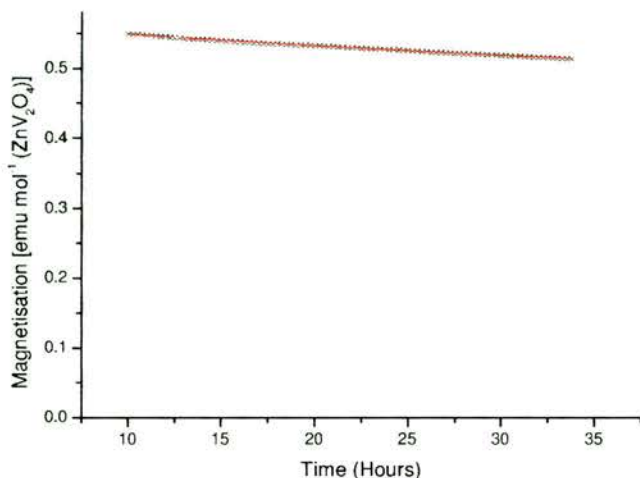


Figure 10. 15 shows the decay in remnant magnetisation at 10K and 60K against time.

Below the apparent Neel temperature of 39K, the material is seen to be able to sustain a significant level of induced magnetisation over time. This is not surprising in view of MuSR data that will later show a collapse in spin dynamics at 39K. But this is also like the behaviour one might expect of a spin glass. The decay appears to be broken into two distinct sections, one relatively fast stage for about the first 10 hours and a second thereafter. The curve cannot easily be fitted to a single exponential decay,

suggesting the decay process is not first order, or more than one decay process is present.

Fitting the second section to an exponential decay (model  $M = M_0 + Ae^{-T/t}$ ) gives the following results:



**Figure 10. 16 shows a fit to the latter section of the decay of remnant magnetisation at 10K (fit in red, data points in black).**

$t = 57.78307(4.35938)\text{hrs}$ ,  $M_0 = 0.4475(0.00622)\text{ EMU/Mol}$ ,  $A = 0.11963(0.00573)$ ,  $[R^2(\text{fit}) = 0.99849]$ .

These parameters can only be interpreted in a very general sense as no real physical model for the decay process is offered.  $M_0$  giving a baseline magnetisation and  $t$  giving an indication of the speed of the process. The fit suggests a very slow decay process from the time constant ( $t$ ), but also indicates that the magnetisation is decaying towards a constant value ( $M_0$ ).

Carrying out the same exercise on the 60K data produced the following results:

$t = 27.28525(0.58878)\text{hrs}$ ,  $M_0 = 0.07687(0.00005)\text{Emu/Mol}$ ,  $A = 0.00853(0.00005)$ ,  $R^2(\text{fit}) = 0.99391$

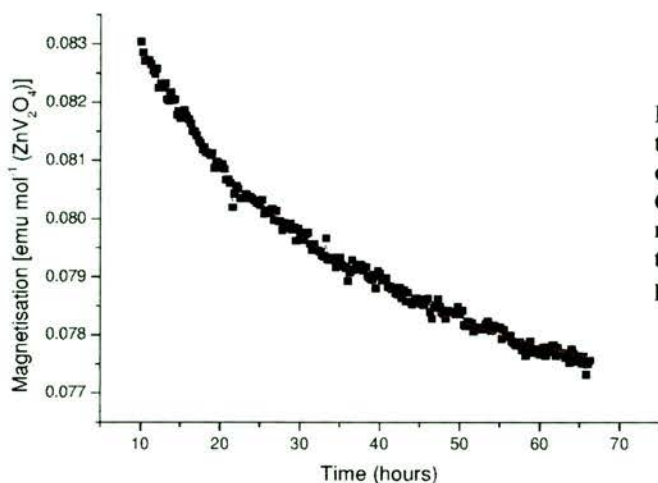
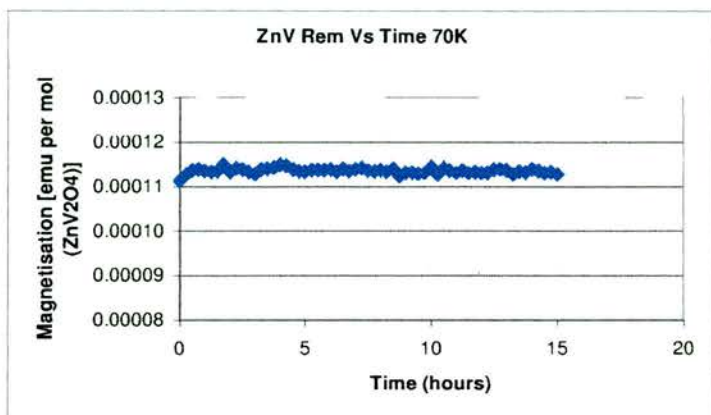


Figure 10. 17 shows a fit to the latter section of the decay of remnant magnetisation at 60K, (note change of magnetisation axis scale for this plot relative to the previous ones).

The measured signal at this temperature is small hence the data is relatively noisy, however, a clear trend is observed. Again, from figure 10.17, we see the magnetisation decaying “rapidly” over a ten hour period, however from the fitting we also see that again the net magnetisation is not decaying towards zero. Evidently, at 60K, the material is capable of sustaining a much lower quantity of time independent field-induced magnetisation than at low; however that the material is able to sustain any time independent magnetisation at this temperature is odd. In this temperature regime, the material is cubic, extremely frustrated to spin ordering, above its spin freezing temperature and possibly subject to the rapid bond length fluctuations implied by a dynamic J-T effect. It is difficult to see how the material can retain any time independent magnetisation at all.

These 10K and 60K experiments were repeated, albeit for shorter lengths of time, resulting in data sets consistent with those shown above. Similar measurements were carried out at temperatures of 70K and 80K. These were carried out over a period of about ten hours each rather than the days of the other two. For the measured time period, these behaved in a similar manner to the 60K measurement. The absolute

magnetisation and apparent residual time independent magnetisations were smaller than at 60K, reflecting the remnant magnetisation vs. temperature plot. At these temperatures, the measured signal was becoming very small and consequently much noisier. No attempt was made to fit this data. The raw 70K data is shown below.



**Figure 10. 18 shows the decay of remnant magnetism vs. time at 70K**

Ueda believed that this region contained uncompensated antiferromagnetic clusters<sup>109</sup>, and that these were causing the divergence between zero field-cooled and field-cooled susceptibility data from 100K downward until  $T_N$ . However given the lack of anything to stabilise those clusters, one would expect that in the absence of the applied field that any net magnetisation due to the same would decay rapidly towards zero, as the clusters are broken up by rapid thermal spin and possibly structural fluctuations. The growth of clusters with decreasing temperature would suggest a second order transition. As these would require the growth of geometrically unfrustrated, or at least less frustrated, structural clusters, one would expect to see the growth of a corresponding gradual structural transition. From section 9 we see that the 51K structural transition occurs over a small temperature range and that no indications of its incipency are observed above 51K. Only at 51K is evidence found of cubic and tetragonal phases both being simultaneously present.

Putting these pieces of evidence together it is hard to agree with Ueda's contention of antiferromagnetic clusters in this region. The situation appears to be more complicated. In a later section (10.13) MuSR data will tend to confirm this.

Given the very small magnetisations being measured here, it is tempting to wonder if the data is real and not just some measurement artefact. However, change is observed over the timescale of the measurements that cannot be reasonably attributed to instrumental drift – the change at one temperature is different from that at another – while we might expect a drift to be constant. The 10K and 60K experiments were repeated yielding the same results. The data follow a rational pattern with respect to increasing temperature, e.g. higher temperature implies greater thermal disruption of whatever is decaying and the time constant reduces. Also the absolute measurements follow a pattern consistent with the remnant magnetisation vs. temperature data. It is difficult to see these measurement data as being other than due to the material itself.

## **10.8 Magnetic Neutron scattering**

Data collected on the HRPD low angle banks gave little indication of magnetic Bragg peaks below 39K, however this instrument sacrifices much in the way of beam intensity to achieve its exceptional resolution at low d-spacings. Very small magnetic Bragg peaks were observed in the HRPD data on close examination. A further low temperature experiment was carried out to look for magnetic Bragg peaks on the ISIS instrument Osiris. This instrument was designed as a combined high intensity neutron diffractometer and spectrometer with good resolution across a large range of d-spacings, with provision for polarised neutron work. At the time of this experiment, the instrument was still being developed as a diffractometer it already had an ideal specification for looking for magnetic Bragg peaks at longer d-spacings.

No cryomagnet was available at that time of the experiment to aid the proper investigation of possible field induced changes in the magnetic scattering. In a crude attempt to mimic a cryomagnet, a steel and aluminium yoke was built to hold the sample can during the experiment and a number of strong permanent magnets were placed on either side of the sample. The assembly was shielded using thick cadmium foil to prevent Bragg scattering from the metal and the instrument's detector elements at angles in line with the bulk of the assembly's metal were disabled. A small amount of aluminium was inadvertently left unshielded, some Bragg scattering from this is seen in the collected patterns.

The effective magnetic field at the sample position was measured using a handheld Gaussmeter as c.60G. Given the magnitude of the applied field and the relatively short distance between the sample and detectors, the applied field should not have any significant influence on the neutrons scattered by the sample. The permanent magnets were removed and the sample cooled from ambient temperature without them for the zero field-cooled scattering experiment.

Patterns at each temperature were collected for the same total number of neutron detector counts to facilitate direct comparison of intensities between raw patterns.

## **10.9 Zero Field-Cooled Magnetic Scattering**

Earlier, a recent paper claiming to have found no evidence of the magnetic Bragg peaks originally reported by Niziol was described herein as being wrong.<sup>110</sup> The plots below, showing diffraction data collected on Osiris (ISIS, RAL) at various temperatures between 4K and ambient settle this argument conclusively.

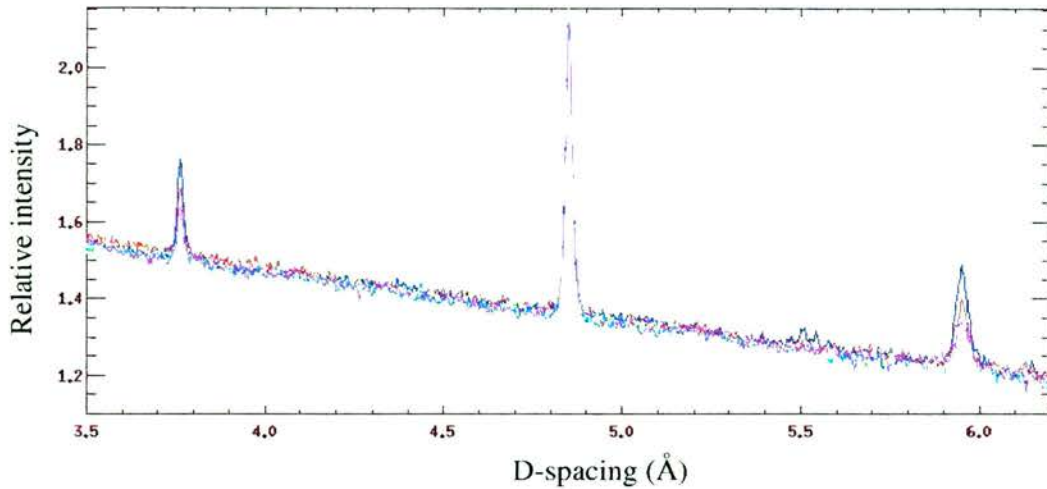


**Figure 10. 19** shows elastic neutron scattering data collected on Osiris at RAL from a  $\text{ZnV}_2\text{O}_4$  sample. The blue dataset was collected at 4K, red 35K, magenta 36K, green 37K, yellow 38K, and cyan 39K. The peak at 4.85Å is structural (1,0,1) whilst those at 3.75Å (1,1,1) & 5.95Å (1,0,0 or 0,1,0) respectively are magnetic.

Niziol's *little humps* were indeed small magnetic Bragg peaks. They are first observed at 39K, which corresponds to a maximum in the zero field-cooled susceptibility data, growing in intensity down to 4K (the lowest temperature measured). No evidence at all was found of these peaks, or diffuse precursors to the same, above 39K. No Bragg peaks, magnetic or structural are observed beyond 6Å.

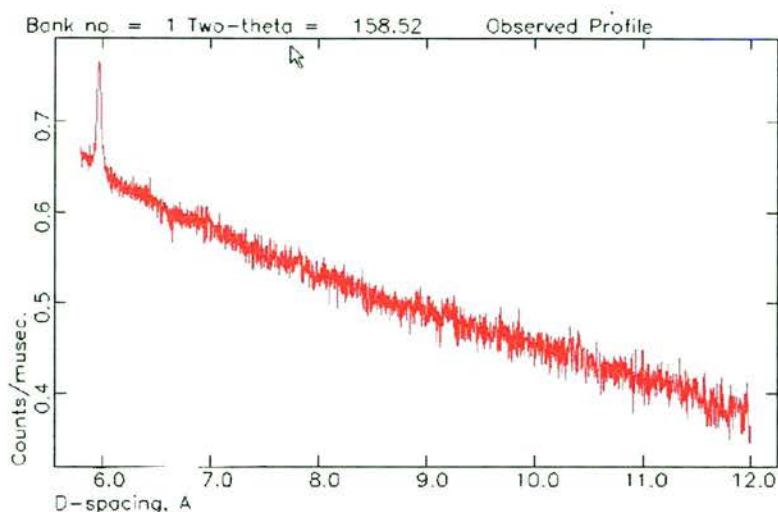


**Figure 10.20** shows the magnetic Bragg peak at c.5.95Å with no further significant peaks above noise out to 12Å.

Less evident in the plots shown above is another magnetic scattering feature found only in the 4K data set. Subtraction of a higher temperature pattern from the 4K data set reveals small features at c.4.3Å and 5.5Å in the 4K data. The feature at 5.5Å is just visible in figure 10.19. Initially, this was thought to be insignificant, perhaps noise, however zooming in on this area in the raw 4K data showed that there were hundreds of data counts describing this small hump-cum-Bragg peak. This feature appears to be real is found only in the 4K dataset. Initially it was unclear whether this was a magnetic Bragg peak or an area of diffuse magnetic scattering. Unfortunately, most of this data was collected around  $T_N$ , below this region data was only collected at 22.5K and 4K, it is not known where this subtle feature first appears other than somewhere between 22.5K and 4K.

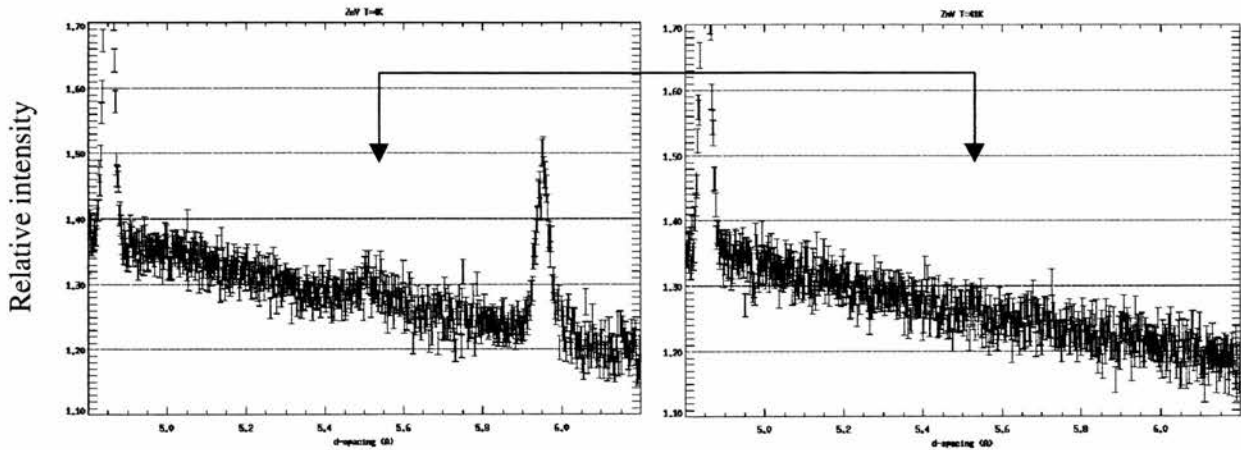


Figure 10. 21 shows the region at  $5.5\text{\AA}$  expanded at 4K(left) and 41K(right), the magnetic Bragg peak at around  $5.95\text{\AA}$  is clearly missing in the 41K data however so is a distinct hump (arrowed) at around  $5.5\text{\AA}$  which is not present at 36K either (when the magnetic reflection at  $5.95\text{\AA}$  is clearly visible at almost its 4K intensity).

A visual estimate suggests that this region of magnetic scattering shows greater width than the other magnetic Bragg peaks. This observation leads one to regard this as diffuse magnetic scattering corresponding to some sort of statistical ordering. It appears that this may be the precursor to a Bragg peak and one might speculate that at even lower temperatures it might become so. Careful examination of what initially appears to be to be background counts reveals several other areas which may be showing hints of still weaker but similar diffuse scattering, the feature at  $4.3\text{\AA}$  is a smaller version of the  $5.5\text{\AA}$  region, whilst possible features are observed at lower d-spacings. This data was latterly inspected by people with some expertise in the area of diffuse scattering, who confirmed this interpretation of these scattering features.<sup>111</sup>

Reference to some of the other plots of the Osiris data below (fig.s 10.22 & 10.25 say) puts the intensity of the magnetic Bragg peaks into some context. These peaks are extremely weak, possibly suggesting that some of the expected moment is missing from the ordered magnetic structure. This may be accounted for by the diffuse magnetic scattering. It is also consistent with the argument that there is more than one magnetic component present in this material. In the paper where they claimed that

there was no Neel type ordering, Buttgen *et al.* reported that their transverse MuSR work suggested the presence of a spin-density wave. However, this interpretation was made on the basis of their incorrect assumption that there was no Neel ordering, it is possible that they were in fact seeing some reflection of incipient Neel Ordering.<sup>112</sup> [It is unclear why that group failed to find the Neel Bragg peaks].

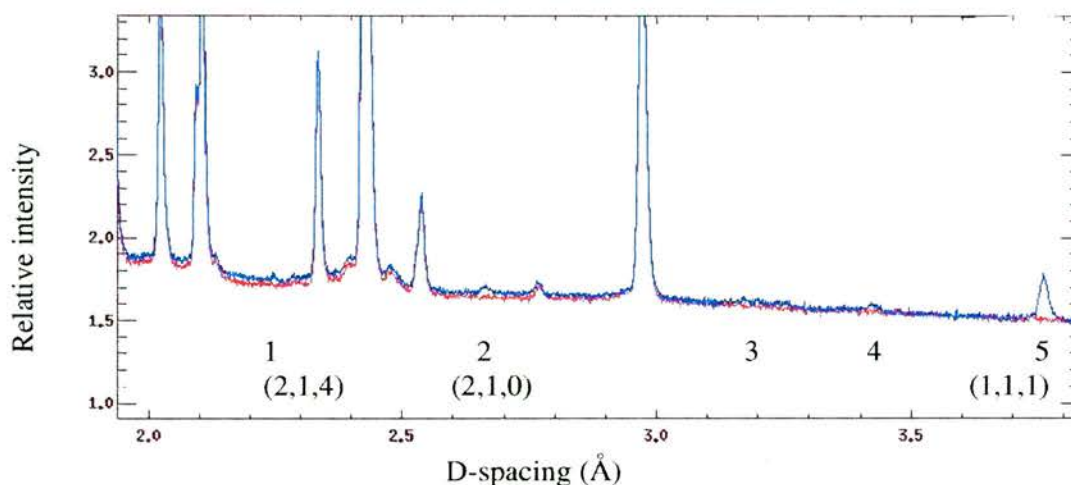


Figure 10.22 shows another plot of 4K and 41K Osiris data : small magnetic Bragg peaks are seen at about 2.25Å (2,1,4) - [1] and 2.65Å (2,1,0) - [2] as well as the 3.75Å (1,1,1) - [5] magnetic peak seen in figure 9.40 above; regions of seemingly diffuse scattering are centred at about 3.2Å(3) and 3.42Å(4). Other peaks are structural.

## 10.10 ZnV<sub>2</sub>O<sub>4</sub> 4K magnetic structure

The magnetic Bragg peaks can be indexed on either the cubic or tetragonal structural unit cells. The tetragonal cell is used as this immediately implies more directionality to the crystal than the cubic equivalent. Niziol and others have tended to use the cubic indexing scheme, presumably on the basis that the tetragonal distortion is very slight.

A combination of HRPD and Osiris data was used in the magnetic structure and moment determination. The HRPD 90° bank data containing primarily chemical structure data whilst the Osiris data held relatively little chemical structure data and most of the elastic magnetic scattering. The Sarah representational analysis software

suite<sup>113</sup> was used to test a number of possible magnetic structures based on probable magnetic propagation vectors ( e.g.; [0,0,0], [1,1,0], [0,0,1], [0.5,0.5,0], [0,0,0.5]). Once likely candidates were thus identified, a second, magnetic only, phase was added to a GSAS refinement containing the above mentioned data sets and the chemical structure model; Sarah then uses a Monté Carlo method to vary the GSAS magnetic phase parameters in order to find the best fitting model for the magnetic data and to extract an effective moment. The structure derived is shown in figure 10.23 below.

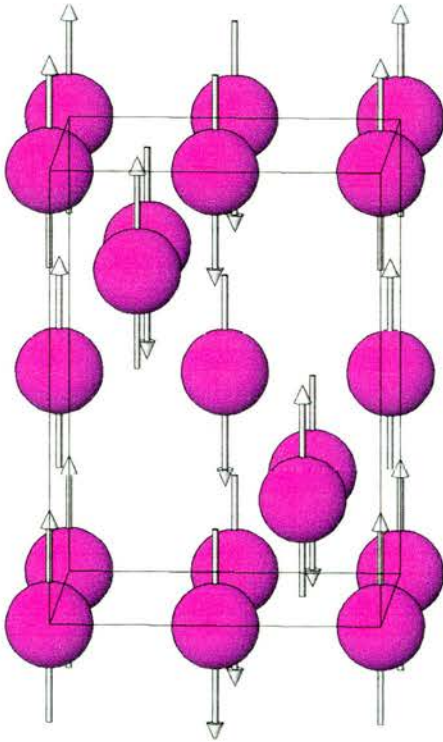


**Figure 10. 23 shows the ordered magnetic structure extracted from the magnetic Bragg peaks.**

Vector [001] was found to propagate the structure, which can be described as ferromagnetically coupled chains in the c direction antiferromagnetically coupled along the b direction. The moment required to give the observed amount of magnetic scattering was determined to be around  $0.72(0.21)\mu\text{B}$ .

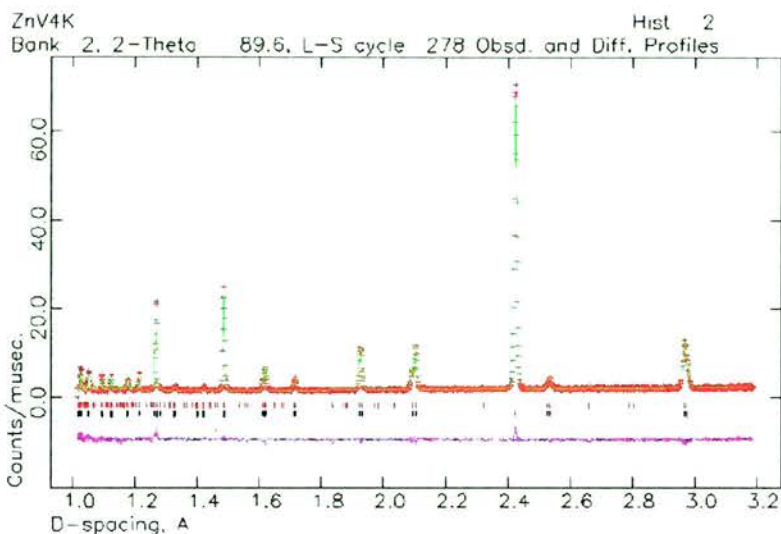


Figure 10. 24 shows the refined model, experimental data from HRPDs 90° banks and difference maps for the structural and magnetic phases.

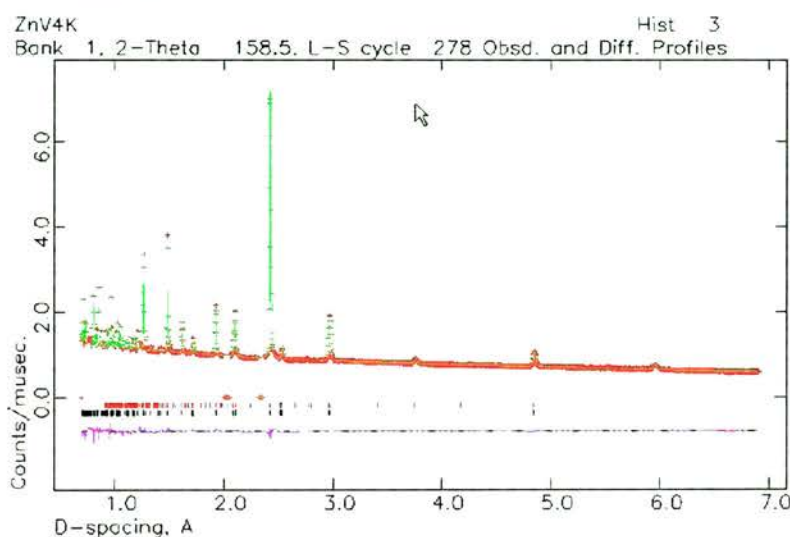


Figure 10. 25 shows the refined model, experimental data from Osiris and difference maps for the structural and magnetic phases.

At low temperature the spin-only moment is expected to be  $c.2\mu_B$  [the total spin value ( $S$ ) times the gyromagnetic ratio ( $g$ ), for the  $3d^2$  cation  $S = 2/2 = 1$ , hence 1 times  $c.2$ ]. From the expected  $g.S$  value of  $2\mu_B$ , we conclude that either  $g$  is 0.72 – which seems extremely unlikely, or that a proportion of the moment is not involved in this ordered magnetic structure.

The derived structure also shows that the observed ordered moment exists only and is collinear in the  $c$  direction (with respect to the crystal unit cell). This is intriguing and very important. It implies that the missing moment can only have  $ab$  dimensionality

*across the crystal*. Any ordering at all of that component, e.g. canting of spin would result in a non zero dot product for the total cation moment and generate additional Bragg reflections. In other words, if there is an ab component it must have continuous rotational symmetry about the c direction *across the crystal as a whole*. The beginning of the loss of that rotational symmetry perhaps being reflected in the diffuse scattering at finite d observed at 4K (as per figure 10.21 above). It may be coincidental however, we note that the c.0.72 $\mu$ B value is c.1/3<sup>rd</sup> of the expected moment value to within experimental and fitting error, almost as if describing the 1/3<sup>rd</sup> directional component of the whole moment distributed equally in all three dimensions. This is intriguing given the possibility of an antiferromagnetic arrangement of spins on a tetrahedral lattice pointing towards or away from the centre of the tetrahedra would give an equal a,b & c distribution of moment. There is perhaps a close proximity to such a state.

Given that the magnetisation data has already shown what appears to be an independent glassy-like magnetic component, moment missing from the ordered magnetic scattering is not entirely unexpected and strongly enhances the latter contention. The presence of diffuse-like scattering at 4K gives us some indication of where that missing moment might be. And the requirement from the determined structure that that moment lie in the ab plane only serves to enhance this view.

This simultaneous coexistence of ordered and disordered magnetic components accords to the physical behaviour expected of the semi-spin-glass state predicted by Villain in 1973.<sup>114</sup> However, his theoretical prediction requires structural cation disorder (multiple magnetic cation types on the same lattice(s) giving mixed magnetic exchange strengths), ZnV<sub>2</sub>O<sub>4</sub> singularly fails to meet that condition. If anything, the

lack of structural disorder in this spinel is worth commenting on as being exceptional. How then can we envisage the pinning of a glassy like component in the absence of that random structural element? And why is there a glassy component in the first place?

### **10.11 Thesis expanded**

From our ligand and spin orbit coupling considerations, we note that one of the 2 d-electrons becomes confined to the former xy orbital in the distorted state, whilst the other has a choice in LS coupling to the former xz or yz orbitals. Once coupled – that electron and orbital lower in energy relative to the unoccupied orbital. This is effectively a quantum well – the electron having to overcome the coupling stabilisation energy to switch to the other of the former orbitals and couple there. The both are potentially degenerate, but the small coupling stabilisation creates an energy barrier. The lack of an observed second cooperative deformation of the structure tells us that there is no orbital ordering of this 2<sup>nd</sup> electron, its location being random from one cation to the next. Within the crystallographic structure both orbitals are equivalent by symmetry, hence there is no reason for either to be occupied in excess of the other – assuming no external forces act on the system.

The spin state of this 2<sup>nd</sup> electron is determined by the orbital it “chooses” to occupy and couple with – Hund’s rule coupling then requires the xy electron, which cannot be LS coupled, to adopt the same spin state. Thus the total spin state of both electrons is determined by which of the former xz and yz orbitals the 2<sup>nd</sup> electron “chooses” to occupy. The x,y and z density components of the xy electron are completely fixed by its wave function. The 2<sup>nd</sup> electron has the z component only of its wave-function fixed, the x and y components vary from one cation to the next, depending on the

actual orbital occupation of each cation. Thus, collectively across the crystal, only the z (or c) component of electron density remains ordered throughout. An **orbital liquid** state is extant in the xy components until  $k_B T$  is reduced to an extent whereby there is insufficient energy to overcome the LS coupling barrier. [This explanation is equivalent to that given in the section on structure – the orbital liquid being equivalent to the dynamic Jahn-Teller effect – a resonance structure]. The orbital liquid state has already been identified and reported in the orthovanadate perovskites, e.g.  $\text{LaVO}_3$ .<sup>115</sup> In the perovskites however, the 2<sup>nd</sup> cooperative deformation is observed, lifting the collective orbital degeneracy.

Reaching that  $k_B T$  limit whilst cooling the extant orbital state of individual cations begins to freeze out resulting in the random *static* xy distribution of electron density and the advent of an **orbital-ice** like state.

Magnetically, only the z component is capable of undergoing Néel ordering as xy exchange strengths will vary according to the local configuration of the orbital ice state. When the Néel temperature of 39K is reached however, spin dynamics have to collapse to maintain the ordered z (or c) component of the moment. The dynamics of one of the moment components cannot collapse while the remainder do not – these are the same electron dynamics for both components. Thus at this temperature, we see Néel order AND the freezing of a disordered magnetic component. In isolation this latter component would be described as a spin glass! This is a qualitative difference between this unreported/unpredicted state and Villain's semi spin-glass state, where two freezing temperatures are anticipated.<sup>116</sup>

We thus use the idea of the orbital/liquid ice condensation and LS coupling to describe both the magnetic and structural properties of this material.

The remaining experimental evidence displayed below is quite consistent with this model. However, it is worth returning to earlier problems at this time. The Pauli-like near temperature independent susceptibility which caused so much difficulty in fitting the magnetisation data, the abnormal amount of magnetisation that could be frozen into to the material via field cooling, etc., These can now be explained in simple terms.

When applying a magnetic cooling or measuring field, the collective orbital degeneracy of the orbital liquid and ice states allows the applied field to split the energy of xy orbital states – those components parallel being lowered in energy and the converse – thus biasing the occupation of the available states. In the orbital liquid state, no divergence between field and zero field cooled data sets would be observed as  $k_B T$  overcomes the energy barrier to inter-conversion of orbital states. This would suggest the condensing of the orbital liquid occurs somewhere just above 100K. When this condensation begins, however, we begin to freeze orbital biasing and hence magnetisation into the sample – the divergence of field and zero field cooled magnetisations is observed. The 2<sup>nd</sup> electron's spin is dragged into this biasing and its Hund's rule coupling drags in the spin of the xy electron. So, a significant proportion of spin moment is added into the orbital biasing that we measure – including that of the xy electron, where that moment is not itself reduced by LS coupling. Hence we see an abnormal amount of divergence between field and zero field cooled magnetisation.

The orbital ice like state also explains the remnant magnetisation that we observe above  $T_N$  – which the experimental evidence suggests is not related to uncompensated antiferromagnetic clusters. Again the Ice like condensation is capable of retaining

field induced magnetisation. Spins may well be fluctuating rapidly in that regime – but their coupling and biased orbital occupation yields a net magnetisation. Below  $T_N$ , we have the same Orbital Ice element, only now compounded with a *static* spin dynamics – both Néel in the  $c$  direction and induced biasing in the  $ab$  – hence the frozen-in magnetisation increases sharply.

The sharp step in magnetisation observed on the structural deformation at 51K – this reflects the partial quenching of LS coupling as one of the electrons drops into the singlet  $xy$  occupation and loses its ability to be LS coupled.

The energy barrier between the two orbital possibilities per cation is not likely to be very high, hence when the sample is cooled and measured in a large magnetic field [ $\approx 1$ +Tesla], it may become possible to tend towards saturating the orbital occupation. With all cations adopting the same induced orbital occupation – it seems likely that a saturation of this induced ordering would result in the second structural deformation becoming apparent – would might suspect that this would occur around  $T_N$ . High resolution x-ray diffraction carried out on a single crystal exposed to large homogenous applied fields across the 30K to 150K temperature range might prove an interesting test of this conjecture. Although the orbital occupation could become saturated in that way, this does not mean that it would necessarily be observed in  $M/H$  sweeps – if the interconversion barrier is low enough, both orbital and spin components would simply follow the field; the spin portion would dominate the data easily masking any subtle change in the orbital contribution. Saturating the spin component would require much larger fields most likely. We may also have an explanation for the “large field” magnetisation measurements and lack of any coercivity or non-linearity in the  $M/H$  data.

One must also suspect that applied field induced orbital ordering throughout a single crystal would also result in a different magnetic structure as the strength of xy interactions becomes ordered. Tentative hints of this possibility are given in section 10.12.

Finally, the apparent Pauli-like almost temperature independent magnetisation component is almost that. It is a quasi-Pauli susceptibility grounded in the field induced biasing of localised orbital occupation rather than that of a collective metallic band – which is in any case simply an extend molecular orbital.

## **10.12 Field-Cooled Magnetic scattering**

Having employed the permanent magnets to field cool the sample as described above, the first thing to note is that the sample appears to have moved slightly from its position in the Field-cooled experiment described above. This is observed in changes to the two aluminium Bragg peaks seen in the previous pattern. A marked change in the relative intensities of these two peaks signifies both considerable preferential orientation of the metal crystallites and a change in the position of the metal relative to the detectors. The position of these peaks does not change. As this assembly element was holding the sample can one must also suspect that a slightly different amount of sample might be in the beam than was the case in the previous experiment. However, a slightly different amount of sample in the beam should affect all of the features and relative intensities in the resultant pattern equally. Thus it is still possible to normalise data from both Field-cooled and Zero field-cooled experiments at equivalent temperatures and carry out subtraction to look for differences. Subtle

differences are observed between zero field-cooled and field-cooled patterns collected at the same temperature.

In figure 10.26 below, collected at 36K, we see there is a slight mismatch between the normalised intensities of the two patterns. An aluminium peaks are seen at c.2.025Å and 2.35Å. At 36K the magnetic Bragg peaks at c.5.95Å, 3.75Å and 3.4Å (subtle on the above scaling) are already evident. Looking at the peak at 2.45Å, we also see a shoulder sitting to the right of this peak.

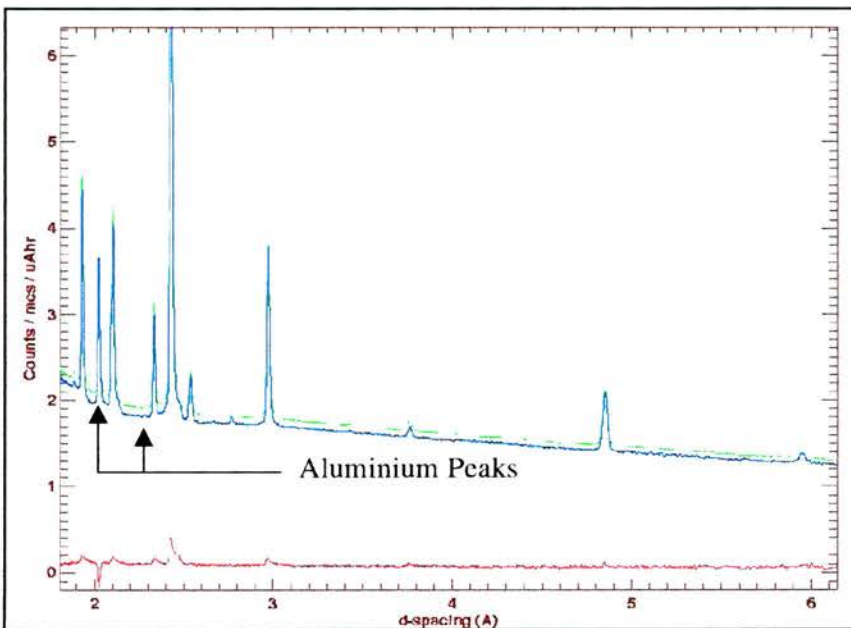
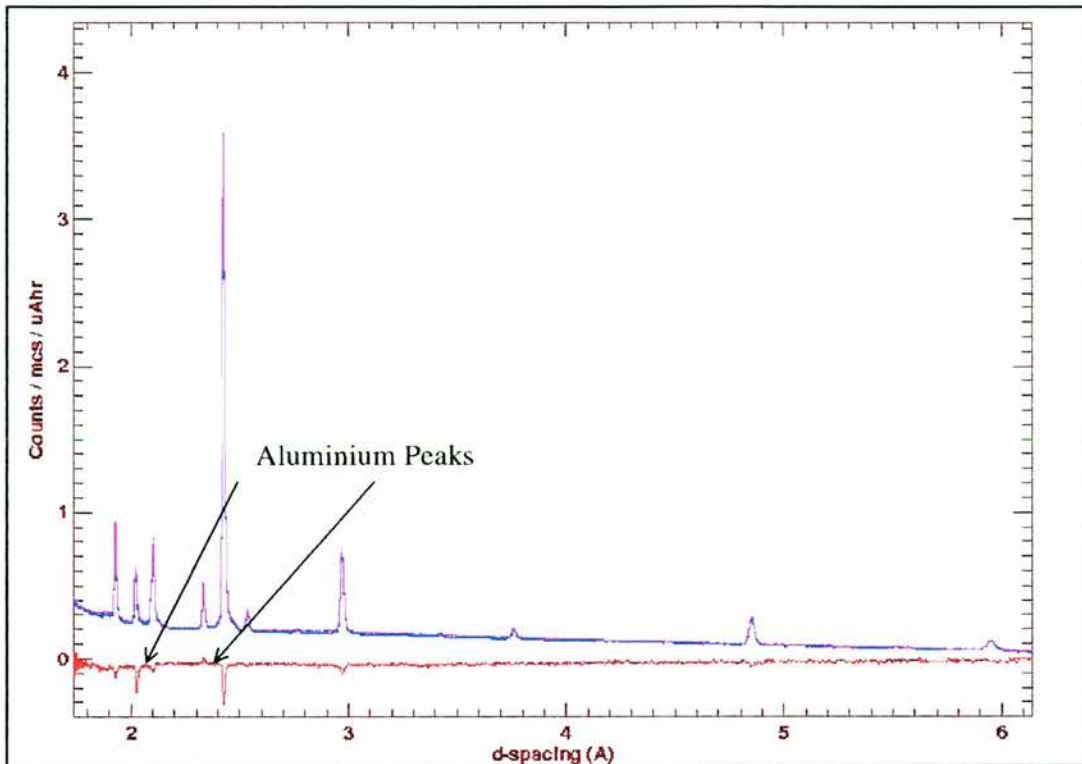


Figure 10. 26 shows field cooled and zero field-cooled patterns collected at 36K. The field-cooled pattern is shown in green, the zero field-cooled in blue, a difference map is in red.

With the exception of the shoulder on the one peak, there appears to be relatively little difference between the two patterns that cannot be accounted for by a slight difference in the normalisation of the two patterns. It is tenuous, but the shoulder might indicate that cooling the sample in an applied field is giving a little more scattering at about 2.45Å. The situation becomes more interesting when we now inspect the 4K data.



**Figure 10. 27** shows field cooled and zero field-cooled patterns collected at 4K. The field-cooled pattern is shown in magenta, the zero field-cooled in blue, a difference map is in red.

The normalisation has scaled the patterns to a lower absolute intensity than in the previous plot. Initially, it may seem that this can account for all of the differences between the two plots, however the aluminium peaks now become extremely useful. One notes that from the difference maps the sense of the change between zero field-cooled and field-cooled remains the same for the aluminium peaks at both 4K and 36K, whilst the sense of the difference between the sample peaks over the two plots changes. Thus the aluminium serves as an internal standard and tells us the changes in the sample peaks cannot be accounted for simply by moving the sample during the change from the zero field-cooled to field-cooled experimental set-ups. Although the sample was moved, the only difference between the zero field-cooled 4K and 36K datasets is temperature and ditto the field-cooled datasets. Visually, it appears that the difference in scaling between the four datasets is insufficient to account for the

changes.

This experiment was planned suspecting it might be possible to *see* a glassy magnetic component in diffraction data by field cooling a  $\text{ZnV}_2\text{O}_4$  sample. It was thought that the field might partially align the glassy moment, this would necessarily occur on the vanadium sub-lattice. Thus it was thought that additional (magnetic) scattering might be observed on the structural Bragg peaks corresponding to the vanadium sub-lattice (similar to that seen in a ferromagnet). Unexpectedly, this experiment appears to have given us the opposite result. At 4K, field cooling the sample appears to have resulted in lower scattering intensities on, at least some of, the structural Bragg peaks. No difference was observed in the intensities of the magnetic *antiferromagnetic* Bragg peaks. The shoulder / extra peak evident in the 36K data at  $2.45\text{\AA}$  has disappeared by 4K. These observations are difficult to interpret, however the large peak at  $2.4\text{\AA}$  whose difference changed sense between 4K and 36K contains both magnetic and chemical structure scattering – as the chemical structure is a constant, we are forced to conclude that the magnetic contribution has changed and to suspect that the small applied field may have influenced this observation!

Given the relatively crude means adopted to attempt this experiment, the complications added by having to move the sample *et sim.*, there is a danger of over-interpretation of this data. What it does suggest however, is that there is some sort magnetic structural property of this sample which can be influenced by the application of a small field (max 60 Gauss) - to an extent whereby it is apparent in neutron diffraction patterns. In larger fields more significant changes might have been observed, however we could not obtain a proper cryomagnet with which to carry out such an experiment.

## 10.13 MuSR

MuSR on oxide materials has a significant difficulty, namely that the models and functions used to fit MuSR data were developed to describe the muon's behaviour in magnetic metals or alloys. As a relatively young science, MuSR is rapidly developing models for other types of material, however, one should bear in mind that fitting functions are not optimised for oxide materials.

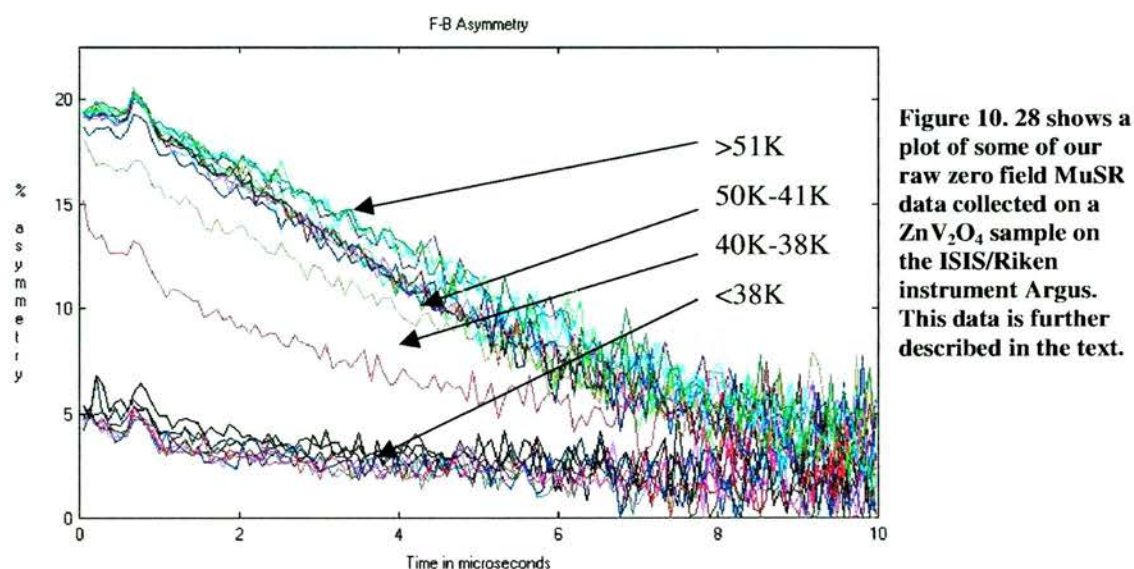
A further problem arises when using pulsed muon sources such as those at ISIS. The nature of the pulse results in a smearing of fine detail often found at very short muon decay times (0-0.2 microseconds). An ordered magnetic phase results in small oscillations at these short times, the convolution of several oscillatory functions signifying the presence of more than one ordered component. This would require a steady state source, rather than pulsed. Modelling such data can be conclusive in determining the nature of the order as observed by muons. Acquiring this data additionally requires that the instrument has high frequency resolution, again unfortunately the ISIS instruments do not have this resolution.

When these experiments were carried out, the long range ordered component and the possibility of a second ordering at lower temperatures were not known to exist. Thus the experiments were of a general nature. In retrospect, the use of a steady state source with high frequency resolution would have been preferable. Nevertheless, these experiments offer insight into, even from inspection of the raw data, certain aspects of the vanadates' magnetic behaviour.

Although the raw data looks to be untidy, not yielding smooth lines or curves, it's quality is not low as it may seem. Each temperature dataset contains at least 5 million

observations (positron counts) [and >10 million for the raw Argus data shown here]. Errors associated with each point in each set are markedly reduced by averaging over the large number of observations, curve fitting of these datasets takes the residual errors into account. Error bars are not shown in the zero field-cooled raw data plots for clarity, (however are shown in a raw field cooled plot later for inspection).

A set of raw zero-field cooled data collected for the  $\text{ZnV}_2\text{O}_4$  sample is shown below.



Given the quantity of raw data shown in figure 10.28 it is impractical to label each temperature set (coloured line) individually and a key would be almost impossible to read. The sharp peak seen in all datasets at about 0.5 micro-seconds is an instrumental problem (kicker noise) and should be ignored. Four regions are noted; above 51K in the cubic phase; between 50K to 40K (Neel temperature at c.39K); two data sets at 38K and 40K through the main change observed; and finally datasets at 37K and below.

A slight change in line shape is seen to occur around the structural transition at 51K. A close up of this region, (using fewer datasets for clarity) is shown below in figure

10.29. This is probably a signature of a change in the muon's preferred site in the material. Logically, one would expect the embedded muon to come to rest in the sample such that its chosen site minimises Coulombic repulsion. As the muon is positively charged, in a spinel the muon probably sits in one of the vacant tetrahedral holes in the oxygen sub-lattice, similar to that occupied by the A-site cation. This would maximise its proximity to negatively charged species. On distortion of the lattice, the geometry of this site will change subtly and it may be that certain of these tetrahedral sites become more favourable than others. Or that more than one electrically equivalent, but magnetically different, muon site is present in the tetragonal form of the spinel. This change is not however seen to be major, such as would signify magnetic ordering or spin freezing.

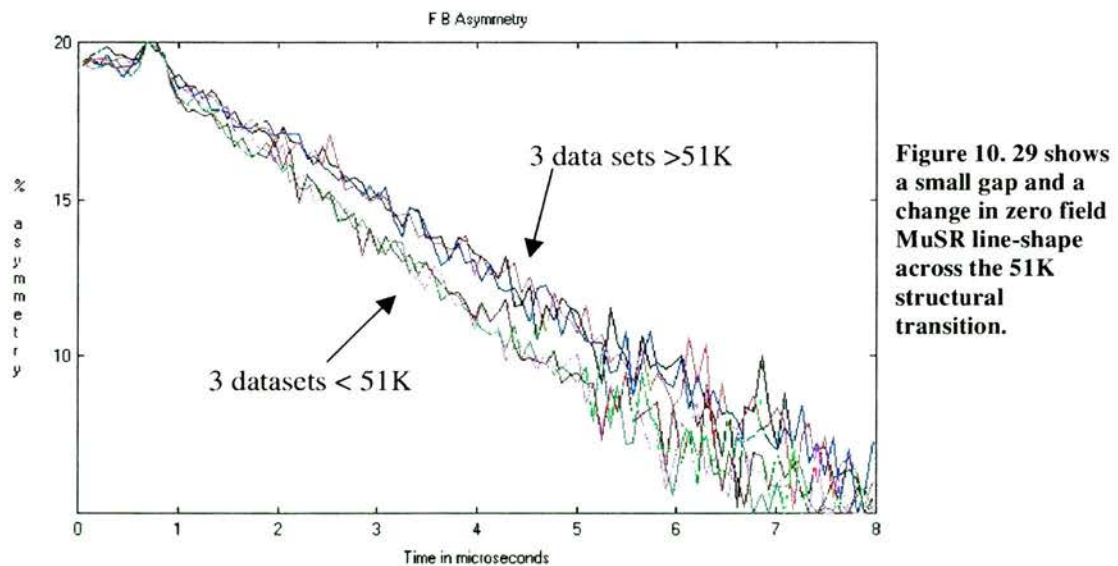


**Figure 10. 29 shows a small gap and a change in zero field MuSR line-shape across the 51K structural transition.**

A second, more striking, change in the muon depolarisation rate is seen to occur at c.39K. [Though some indication of the impending collapse in asymmetry is seen in the 40K dataset]. Below this temperature the muon behaviours is quite different, the initial asymmetry value, if fitted, falls from 18-19% down to around 6%. This signifies the embedded muons are experiencing magnetic fluctuations at a much

reduced rate than was the case above 39K. An apparent reduction to approximately  $1/3^{\text{rd}}$  of the higher temperature initial asymmetry value is known to indicate an effective freezing of spins. This may result from either the appearance of long range order or from a glassy like freezing. This change is seen to occur sharply, over a maximum temperature range of 3K (40K-37K). This implied spin freezing, taken in conjunction with the appearance of antiferromagnetic Bragg peaks at the same temperature, is interpreted as conclusive evidence that 39K is the Neel temperature for  $\text{ZnV}_2\text{O}_4$ . Importantly however, this MuSR data does not tell us that all of each electron's contributed moment has gone into the ordering, merely that that moment is largely static, e.g. it does not preclude the possibility of simultaneous magnetic order and disorder.

Although muon spin relaxation is observed in the above curves, by applying a small longitudinal field this is shown to be largely a nuclear depolarisation effect. Vanadium nuclei carry a  $7/2$  spin, in the absence of a strong external field, these nuclear spins are not ordered and serve to randomly depolarise the muon's spin orientation. The small longitudinal field, parallel to the muon's initial spin polarisation is sufficient to decouple the muon's behaviour from the very weak effects of the nuclei. As shown below, this decoupling removes the bulk of the change in observed asymmetry seen in the zero field-cooled data, leaving much less depolarisation relative to the zero-field case.

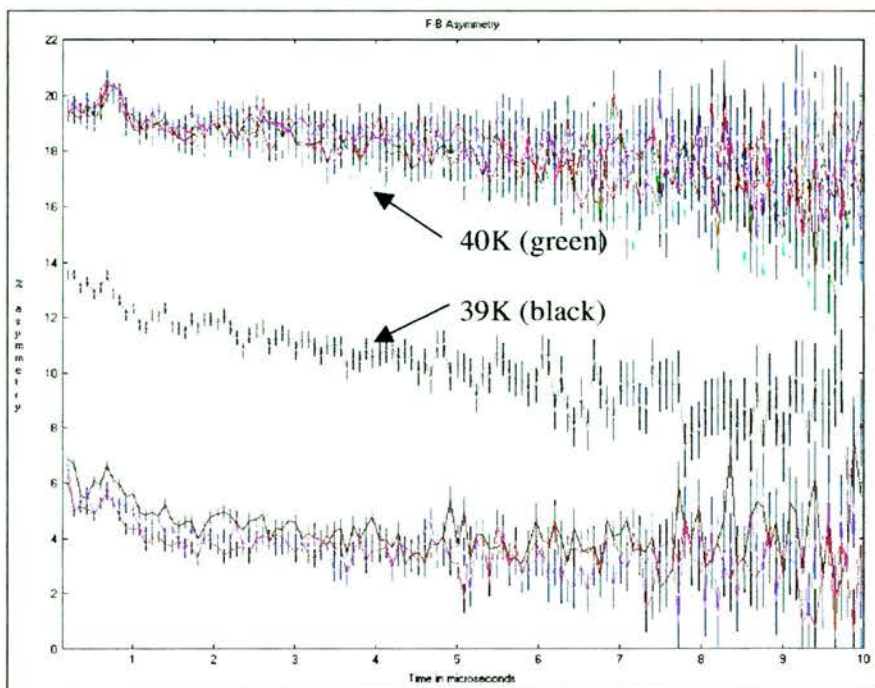


Figure 10.30 shows raw  $\text{ZnV}_2\text{O}_4$  MuSR data collected in an applied field of 30G temperatures 33K-59K, error bars are shown. 39K and 40K datasets marked, sets above 40K at higher temperatures, those below 39K at lower temperatures.

The small applied field has removed the slight change in asymmetry/line-shape associated with the structural transition, this can be rationalised if we assume that the depolarization was due to the vanadium nuclei from which the muons are now decoupled in the small field. There is only one significant change of behaviour observed, that around the Neel temperature at c.39K. Again, this change is seen to occur abruptly over a small temperature range.

#### 10.14 Fitting $\text{ZnV}_2\text{O}_4$ MuSR Data

In the absence of a model specific to this oxide material, the MuSR data was fitted in a simple manner;

Data was examined at the highest temperature to estimate the initial asymmetry value, which, logically should not vary with temperature or applied field during the course of the experiments, this reflecting the initial state of the muons immediately on entering the sample. At the lowest temperature data was then examined to ascertain the

minimum asymmetry value observed. Fitting of the datasets was then carried out within these limits. Having established that the bulk of the depolarisation was arising from vanadium nuclei (via inspection of data collected in a de-coupling field), the highest temperature zero field data was modelled using a Kubo-Toyabe ( $KT_f$ ) function convoluted with a single Lorentzian decay. The  $KT_f$  is intended to account for the nuclear effects that should remain constant throughout, whilst the Lorentzian accounts for relaxation effects which we would expect to vary with electron magnetic changes in the sample. The  $KT_f$  parameters were then fixed along with the initial and final asymmetry values and the Lambda parameter of the Lorentzian allowed to vary.

Fitting the zero field data in this way yielded the plot of Lambda shown in figure 10.31 below. Focusing in on the region above the major change in behaviour at c.39K gives the plot seen below in figure 10.32.

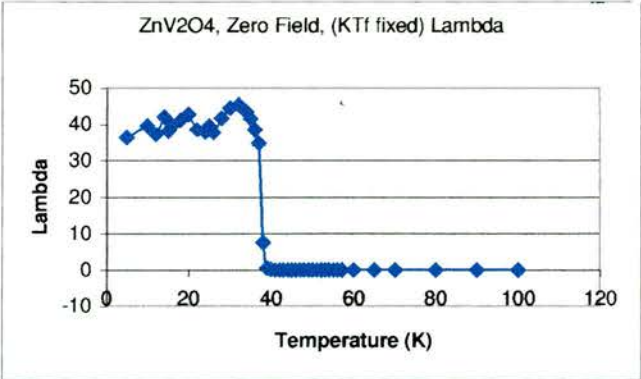


Figure 10. 31 shows Lambda for the zero field MuSR data fitted as described above.

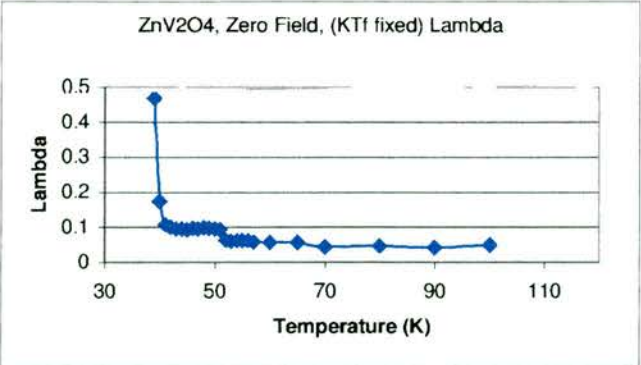
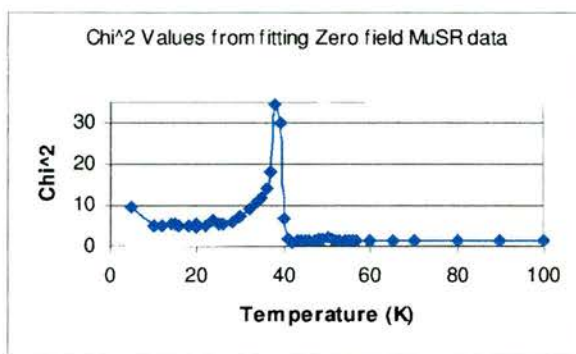


Figure 10. 32 shows data as per figure 10.31, expanding the lambda scale.

From these two plots we note a relatively constant Lambda value between 100K and 52K, a slight jump at 51K from around c.0.05 to c. 0.09 – corresponding to our structural transition – and a large increase in Lambda around 39K, from c.0.09 to c.40 – where the neutron scattering data first observes magnetic Bragg peaks. Fitting errors ranged from +/- 0.0011 to 0.0018 between 40K and 100K, and from +/- 1.1 to 1.8 between 33K and 5K, the two distinct scales making plotting with the data awkward. Chi<sup>2</sup> values on the fits are shown in figure 10.33 below:



**Figure 10. 33 shows Chi<sup>2</sup> for the fits of the data shown above.**

The Chi<sup>2</sup> values show that the model gives a poor fit to the pattern of Muon depolarisation below 39K relative to that above. The change in asymmetry with time in the lower region is extremely fast, too fast for the given function to model effectively. Lambda here then, can only be interpreted as a loose measure of the rate of muon depolarisation and having an inverse relationship to the rate of magnetic fluctuations the muons experience in the sample. Variations to which model parameters were and were not fixed could improve the visual quality of the fits and reduce the relevant Chi<sup>2</sup> values, however what physical meaning variation in said parameters would imply is debatable.

The increase (approximate doubling) in Lambda observed across the structural transition may be caused by the tetragonal spinel variant now being able to support static of magnetically ordered clusters and the appearance of such features. However,

the structural change implies a change in the thermalised muons' environment, there may be two distinct muon sites in the tetragonal variant. Both possibilities may be correct and combine to give this feature. The major change at 39K, (c.500 fold increase on 51K to 39K data, or c.1000 fold relative to above 51K), is the most distinctive feature of this data. As the 39K temperature corresponds to that at which magnetic Bragg peaks are first observed and where we see a shallow maximum in susceptibility data, this change in Lambda is taken to imply a spin freezing at this temperature. Following on from the neutron scattering data, this MuSR data is unequivocal in defining the Neel temperature. The MuSR data implies a freezing of spin fluctuations however and not magnetic order per se. The meaning of variation in Lambda below 39K is entirely debatable and no attempt to interpret it is made here – as noted, the fits were relatively poor in any case.

The fitting of the data obtained in the applied field of 30G (raw data shown 10.35) was also attempted using the same simple model. The model proved to be completely inadequate, it was seen visually that the data and model were incompatible. In this case, the applied field should decouple the implanted muons from the effects of the vanadium nuclei, so there was some justification for modelling using a simple Lorentzian decay function on its own. This yielded results show below:

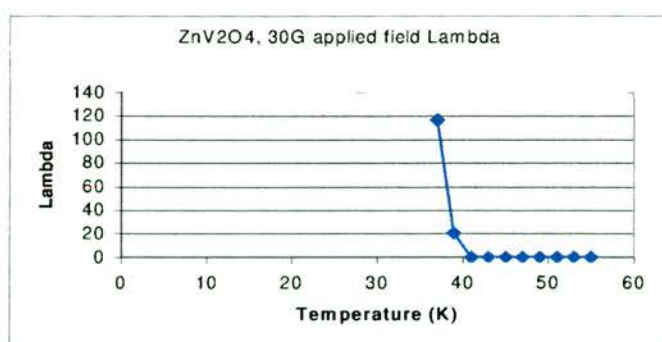


**Figure 10. 34 shows variation in Lambda with temperature for the ZnV<sub>2</sub>O<sub>4</sub> sample in a 30G applied field.**

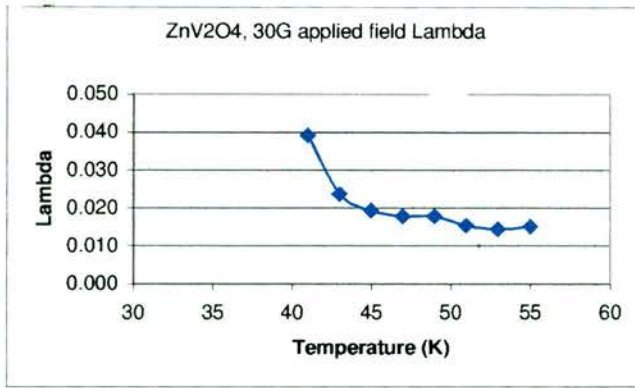


**Figure 10. 35 shows variation in Lambda with temperature for the ZnV<sub>2</sub>O<sub>4</sub> sample in a 30G applied field 39K to 55K (different Lambda scale to previous plot).**

These plots show an increase in Lambda associated with the structural transition at 51K and a very large change occurring around 39K. By 37K a Lambda of 117 was observed, the next temperature down, 33K, gave a meaningless value running to some fourteen figures. This tells us little more than we already knew from the zero field data, though possibly emphasising further the point that the extent of the change in magnetic fluctuations runs to several orders of magnitude. The fitting problem is illustrated below:

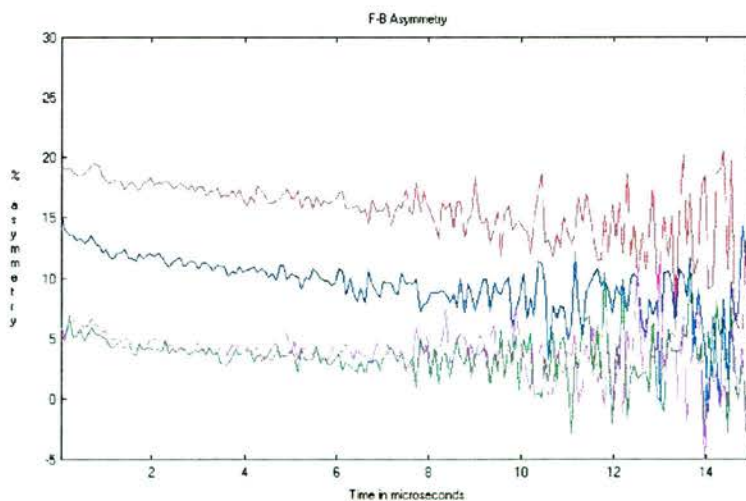


**Figure 10. 36 illustrates the fitting problem, the blue data set in the middle corresponds to 39K, the red above to 41K and the magenta 37K and the green 35K respectively.**

In the figure above, the 39K, 37K and 35K datasets should all begin with their initial asymmetry around 20% as per the 41K set. For those other data sets however, the initial relaxation occurs so quickly that there is no sign of their initial values in this data.

MuSR data collected in a 100G field show the same featureless, almost flat traces that are seen on the 30G data sets. This data was not fitted as the model is inadequate.

In the measurements made using an applied field of 100G, the sample was cooled firstly in zero field and secondly in a cooling field of 100G. The plot below shows raw zero field cooled data. This was done to ascertain whether or not cooling the sample in a field would make a difference to the observed muon behaviour, e.g. can we induce and freeze some measure of moment alignment into the sample via field cooling. As noted, the fitting models are inappropriate for these field-cooled measurements, however inspection of the raw data reveals some change, figure 10.37 below.

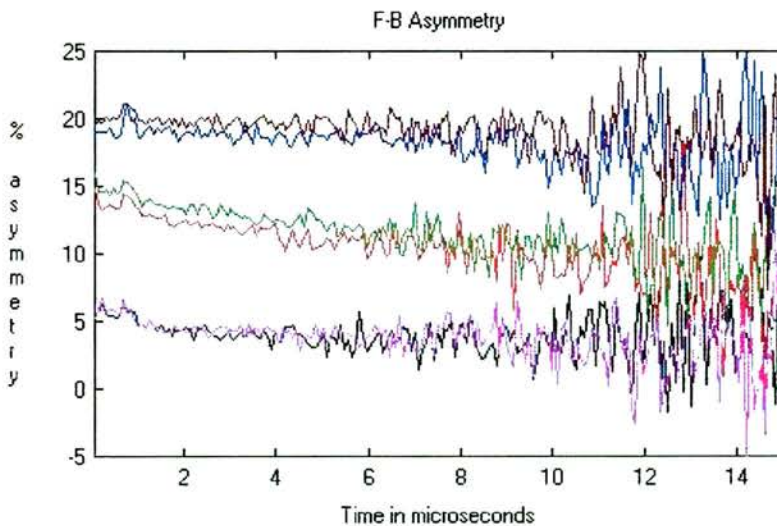


**Figure 10. 37** extracts three distinct pairs of data sets all measured in 100G. Each pairing was collected at the same temperature; 55K, 39K and 33K top to bottom respectively. The brown, green and magenta sets were zero field-cooled whilst the remainder were taken from the sample cooled in 100G.

Differences between the field cooled and zero field cooled data sets can only be attributed to the cooling conditions as the same applied field was used in both measurements and the sample had not been moved or altered in any way. Differences are observed, with the field-cooled data lying a little below that of the zero field-cooled. The implication being that field cooling results in a slightly faster muon depolarisation. Hence, it appears that field cooling has indeed induced some measure

of additional moment alignment within the sample. The applied fields involved are too small to induce alignment of the nuclear moments and this additional alignment can only thus be related to electrons.

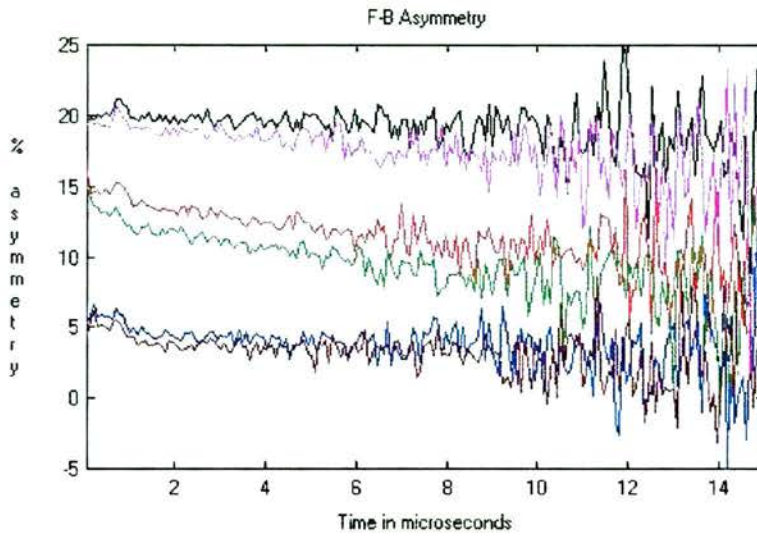


**Figure 10. 38** extracts 3 pairs of zero field cooled raw data sets. Each pairing was collected at the same temperature; 55K, 39K and 33K top to bottom respectively. The black, red and blue were measured in 100G applied, while the magenta, green and brown were measured in 30G.

In the final plot shown in this section, above, we see the zero field cooled sample measured in 100G and 30G applied fields. We note that even these small applied fields induce a discernable difference in the collected data. Here, the smaller applied field appears to be inducing a slightly faster relaxation during the 0 to 12 microsecond region. Lacking an effective model, making sense of this is not possible, however, the samples' sensitivity to applied fields, cooling or measuring is manifest.

In conclusion for the  $ZnV_2O_4$  muon work, it may initially seem that this has yielded few positive results, however, this is not necessarily the case. The data clearly marks out a temperature at which the rate of spin fluctuations in the material changes dramatically. It is consistent with the conclusions tentatively drawn from the magnetisation measurements and from the neutron data and emphasises the materials' sensitivity to applied fields. The muon data also tends to contradict the contention

that antiferromagnetic clusters form in the temperature region 100K to 51K; the zero field MuSR data in that region is relatively flat suggesting spin fluctuations of a relatively constant rate rather than showing a progressive slowing as clusters propagate with decreasing temperature. We do see an apparent slowing of magnetic fluctuations occurring in the tetragonal regime between 51K and the spin freezing temperature at 39K, which may indicate such clusters. This would be logical given that the geometric frustration is partly lifted in the tetragonal regime. However, the question over why we do not see a spin freezing/Neél ordering on, or immediately below, the lifting of that frustration remains poignant. The reported magnetoelastic, and even smaller, structural distortion that occurs in  $\text{ZnCr}_2\text{O}_4$  does result in an immediate Neél ordering. No ordering is observed in the chromite above that temperature(14K).<sup>117</sup>

## **11.0 Doped Vanadate spinels - Introduction**

Lithium doped vanadate spinels and gallium doped vanadate spinels were prepared in order to investigate the effects of introducing disorder on the magnetic behaviour of the parent  $\text{ZnV}_2\text{O}_4$  spinel. Specific reasoning led to the choice of these two dopants: lithium was chosen in order to introduce electronic disorder onto the vanadium site indirectly; whilst gallium was chosen to induce structural disorder onto the (magnetic) vanadium site breaking up the magnetic sub-lattice. Additional samples of compositions towards the lithium end member were also produced to examine the effect of zinc doping on the unusual heavy fermion-like behaviour observed in the lithium parent material.<sup>118</sup>

In  $\text{ZnV}_2\text{O}_4$ , the vanadium is in a formal oxidation state of  $3^+$ , substituting lithium for zinc in the spinel forces the vanadium into a mixed oxidation state of  $3^+/4^+$  introducing the required electronic disorder. All B-sites are seen to be crystallographically equivalent and no evidence of charge ordering has been reported across the series  $\text{Li}_x\text{Zn}_{(1-x)}\text{V}_2\text{O}_4$ . Thus the dopant effect is one of inducing random disorder. Gallium offered a cation known to occupy the B-site in spinel structures (no examples could be found of Ga on the spinel A-site) whilst its oxidation state of III ( $3d^{10}$ ) would ensure that it had no magnetic properties.

Lithium doping of  $\text{ZnV}_2\text{O}_4$  has an interesting and potentially complicated effect on the electronic structure and hence magnetic properties of the vanadium sub-lattice. Although a compositional metal insulator transition is known towards the Li end member ( $\text{Li} = 0.3-0.4$ ), compositions towards the Zn parent are insulating. This implies localisation of the unpaired d-electrons. Thus when lithium doping the zinc end member induces a mixed oxidation state ( $3d^1$  and  $3d^2$ ) on the vanadium site, electrons are expected to be localised. The localised  $3d^1$  cations are still capable of participating in magnetic exchange, however they are not quite the same as the  $3d^2$  cations and maybe thought of as introducing a small local perturbation to the bulk interactions.

Gallium (III) cations formally have no valence electrons to contribute positively to cooperative magnetic or structural behaviour of these materials.

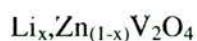
The magnetic and structural disorder introduced by lithium doping might be expected to produce nucleation centres in regions, these could pin either local magnetic order or aid in the formation of a concentrated spin-glass phase. Gallium doping is expected to have a similar effect, however as these cations offer no means of exchanging

magnetic information, their effect is likely to be more pronounced. Generally, one would expect the dopant concentration to suppress the order found in the parent and to produce increasingly spin-glass like materials and one would hope to see some sort of discernible pattern in changes in the magnetic behaviour of these materials as the dopant concentration is increased.

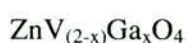
The effect of dopant substitution on the low temperature structure of these spinels is also potentially interesting. It is known that the concentration of Jahn-Teller ions is critical in determining whether or not a bulk JT distortion is observed.<sup>119</sup> In addition to the observation that the direction of the bulk distortion in  $\text{ZnV}_2\text{O}_4$  is counter to that normal J-T arguments would suggest, it has been observed that Li doping rapidly suppresses the distortion.<sup>120</sup> It is shown in this work that this distortion is also rapidly suppressed by the Ga dopants. The dopant concentration at which this occurs is low suggesting that the cooperative nature of the distortion may be more influential than other contributing factors. In this section, the cooperative freezing of a dynamic J-T effect argument presented in the section on the structure of  $\text{ZnV}_2\text{O}_4$  will not be repeated, however doped variants may offer some insight into the role of cooperativity. No reports of gallium doped  $\text{ZnV}_2\text{O}_4$  spinels were found in the literature.

## 11.1 Experimental

Samples were prepared as per the parent material, synthesised in a sealed vessel under a low-pressure argon / helium atmosphere. Samples were then characterised by XRD, PND was also employed for some of the samples. Magnetic susceptibilities were collected on all samples, MuSR data was collected on some of the lithium doped samples.



Lithium doped  $\text{ZnV}_2\text{O}_4$  spinels of compositions  $\text{Li} = 0.01, 0.025, 0.05, 0.10, 0.15, 0.20, 0.85, 0.90$  and  $0.95$  are considered here. In his initial work on the magnetic phase diagram of this series, Ueda had suggested that samples towards the middle of the series adopted the type of concentrate spin or cluster glass behaviour described above.<sup>121</sup> Of particular interest from the literature was the suppression of the low temperature structural distortion towards the zinc end member.



Gallium doped  $\text{ZnV}_2\text{O}_4$  spinels of compositions  $\text{Ga} = 0.0125, 0.025, 0.05, 0.1$  were synthesised in the same manner as the lithium doped variants.

## 11.2 XRD studies at Ambient Temperature

XRD patterns were collected from the samples on a Stoe Stadip diffractometer. X-ray fluorescence proved to be a major problem. Nevertheless, this instrument offered good resolution for determining lattice parameters. The figure 11.1 below illustrates one of the patterns collected.

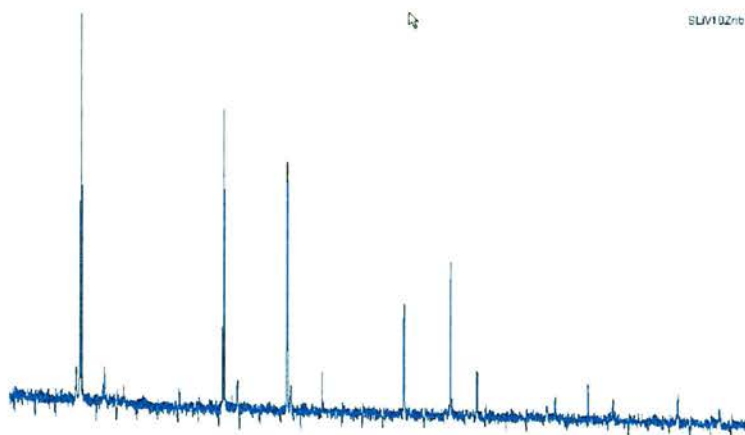


**Figure 11. 1** shows the x-ray pattern collected from the  $\text{Li}_{0.9}\text{Zn}_{0.1}\text{V}_2\text{O}_4$  sample,

Fluorescence is evident, as are spikes, nevertheless the spinel peaks are evident and indexable. The table below gives a typical example of indexing one of these patterns.

D(Å)	2Theta(°)	I(rel)	I(abs)	I(int)	FWHM	H	K	L
4.745914	18.6818	100	897	136.53	0.12	1	1	1
2.914376	30.6519	28.96	260	13.18	0.04	2	2	0
2.486444	36.0943	87.55	785	79.69	0.08	3	1	1
2.380458	37.7607	27.53	247	25.06	0.08	2	2	2
2.062401	43.8628	56.77	509	77.51	0.12	4	0	0
1.588784	58.0034	35.86	322	48.96	0.12	5	1	1
1.459752	63.6992	53.87	483	73.55	0.12	4	4	0
1.396355	66.9605	23.74	213	32.42	0.12	5	3	1
1.259952	75.3775	20.16	181	18.35	0.08	5	3	3

Symmetry : Cubic F, Spacegroup : fd-3m, Cell\_A : 8.2725(12) Å, Cell\_Volume: 566.13(14)Å<sup>3</sup>

Table 11. 1 Shows the indexing of the  $\text{Li}_{0.85}\text{Zn}_{0.15}\text{V}_2\text{O}_4$  sample.

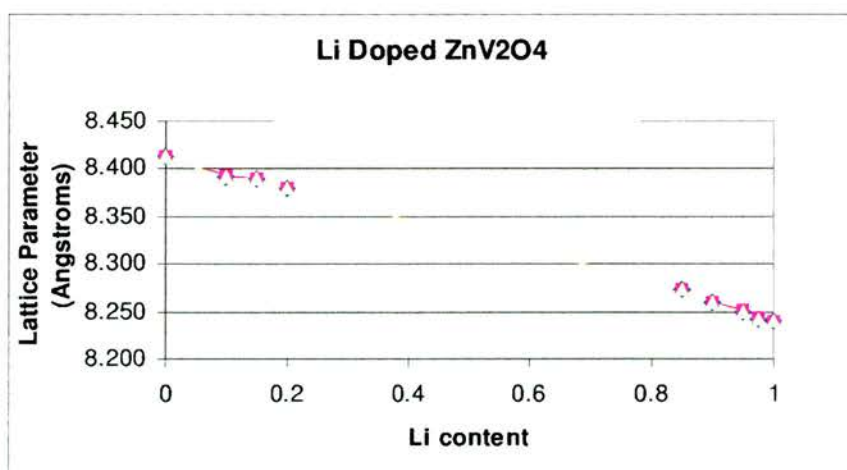


Figure 11. 2 shows a plot of the lithium doped  $\text{ZnV}_2\text{O}_4$  samples' lattice parameters. Plus error bars in pink minus in yellow – error bars obscuring blue data points.

X	Lattice Parameter (Å)
1.000	8.2392(3)
0.975	8.2421(7)
0.950	8.2497(7)
0.900	8.2581(2)
0.850	8.2729(6)
0.200	8.3794(3)
0.150	8.3881(3)
0.100	8.3918(5)
0.000	8.4117(3)

Table 11. 2 shows extracted lattice parameters across the  $\text{Li}_x\text{Zn}_{(x-1)}\text{V}_2\text{O}_4$  series

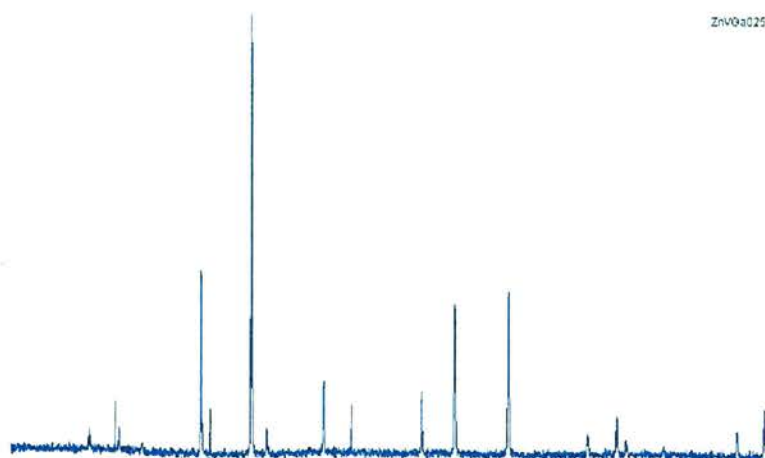


Figure 11. 3 Shows an XRD pattern collected from the  $ZnV_{1.95}Ga_{0.05}O_4$  sample.

$D\text{\AA}$	2Theta( $^{\circ}$ )	I(rel)	I(abs)	I(int)	FWHM	H	K	L
4.861079	18.2353	12.4	418	74.24	0.14	1	1	1
2.974017	30.0226	46.39	1563	198.38	0.1	2	2	0
2.535423	35.3737	100	3370	427.65	0.1	3	1	1
2.427265	37.0058	12.41	418	53.08	0.1	2	2	2
2.101518	43.0053	22.86	770	97.75	0.1	4	0	0
1.715665	53.3565	20.48	690	105.12	0.12	4	2	2
1.617527	56.8776	39.52	1332	236.58	0.14	5	1	1
1.485804	62.4552	41.82	1409	250.41	0.14	4	4	0
1.32879	70.8588	11.11	375	57.03	0.12	6	2	0
1.281693	73.8833	15.08	508	103.15	0.16	5	3	3
1.267157	74.875	9.7	327	49.76	0.12	6	2	2
1.123275	86.5911	11.71	395	70.14	0.14	6	4	2
1.09408	89.5075	16.63	560	127.99	0.18	7	3	1

Symmetry : Cubic F, Spacegroup : fd-3m, Cell\_A : 8.4035(8) $\text{\AA}$ , Cell\_Volume: 593.14(9) $\text{\AA}^3$

Table 11. 3 Shows the indexing of the  $ZnV_{1.95}Ga_{0.05}O_4$  sample whose XRD pattern is shown above.

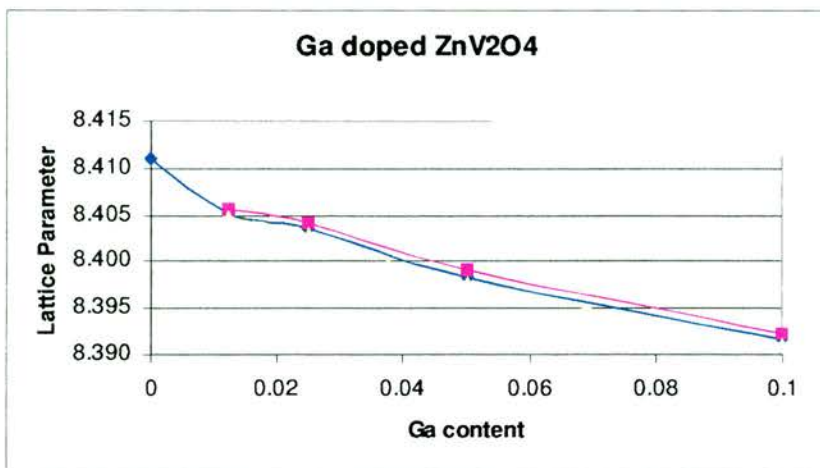


Figure 11. 4 shows a plot of the Gallium doped samples' lattice parameters extracted from XRD. Plus errors bar in pink, minus in yellow, data points in blue.

Ga	Lattice Parameter Å
0.1	8.3916(6)
0.05	8.3983(7)
0.025	8.4035(6)
0.0125	8.4052(4)
0	8.4110

Table 11. 4 shows extracted lattice parameters from the Ga doped  $ZnV_2O_4$  samples.

Both lithium and gallium doped  $ZnV_2O_4$  samples appear to follow Vegard's rule with respect to changes in lattice parameter on doping. While this confirms Ueda's studies<sup>122</sup> on the lithium doped series, the effect of gallium doping is unreported. There appears to be a slight discrepancy with the Ga = 0.0125 sample's lattice parameter. On making this sample, weighing out the amount of gallium required was difficult due to its small quantity, the sample itself might be slightly B-site cation deficient.

### 11.3 Magnetic susceptibility data

The structural distortion feature is seen as a sharp, but small, step in the zfc magnetic susceptibility plot for zinc vanadate. Figure 11.5 below shows a multi-plot of low temperature magnetisation data collected from a number of Li doped zinc vanadates ranging from Li = 0.01 to 0.20. The individual data sets have been off-set on the magnetisation axis to facilitate comparison.

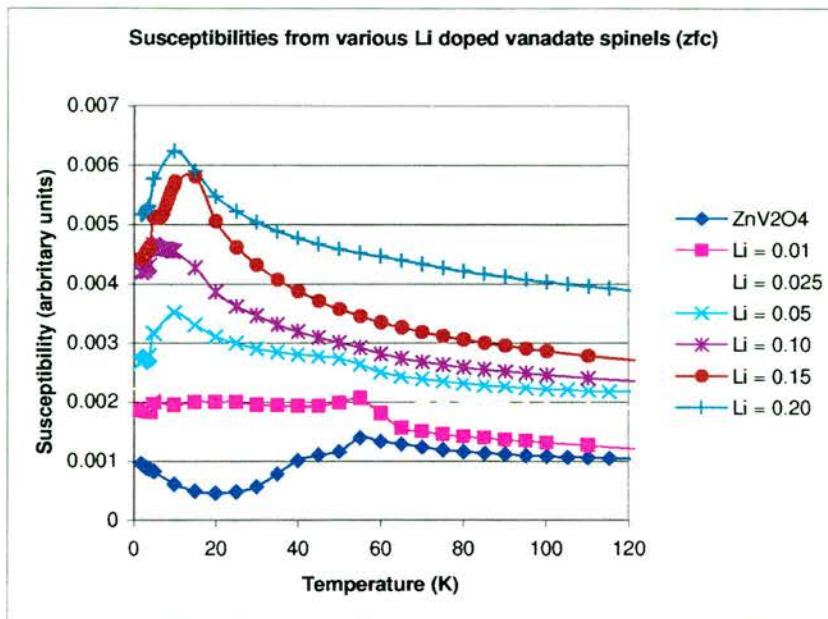


Figure 11. 5 shows zfc magnetic measurements for a range of Li doped ZnV<sub>2</sub>O<sub>4</sub> spinels.

Although these datasets are not collected at close temperature intervals [or particularly good, this data was taken from one of the first set of measurements made], there is still sufficient data to get a general impression of the change in low temperature magnetic behaviour with composition. N.B. the scales are altered in the vertical direction in figure 11.5, to separate the overlapping regions and to allow inspection of the shapes of the curves. The step in magnetisation seen to occur on the structural distortion in the parent ZnV<sub>2</sub>O<sub>4</sub> at c.50K is seen to fade out with increasing Li content. Something is possibly just visible at Li = 0.10, but by Li = 0.15 has disappeared completely. The temperature at which changes in curvature indicating at least some residual of this structural change are seen does not appear to change significantly – it is however hard to estimate this given the relatively wide stepping of the data points.

Broadly, below 50K the form of the magnetisation data is seen to migrate from the parent's peculiar antiferromagnetic/glass like behaviour towards a more spin-glass like behaviour. One might be argue that the magnetic behaviour of Li = 0.15 and 0.20

also looks broadly antiferromagnetic, however this view is contradicted by neutron scattering which shows no indications of long range antiferromagnetic order.

[The data below 4K appears to change for all the doped samples shown above. It seems likely that this is a “4K artefact” caused by liquid helium temperature control issues with respect to the MPMS instrument. Data collected on the MPMS-XL instrument do not show this problem].

Turning to a comparison of the remnant magnetisation measurements on the same Li doped samples is shown in figure 11.6 below.

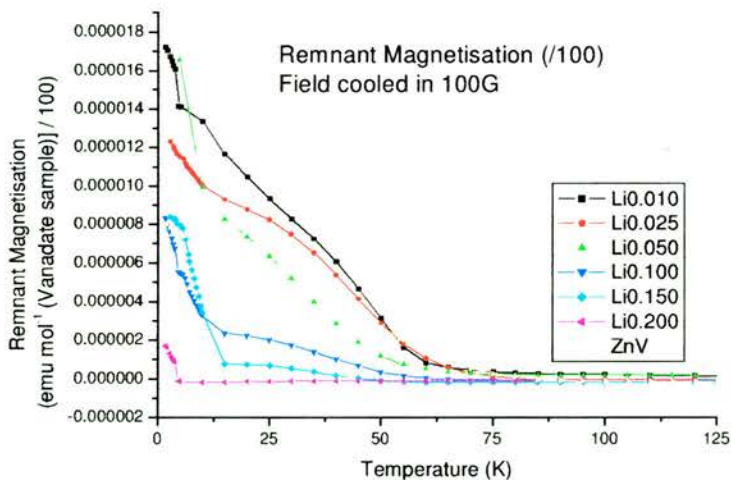


**Figure 11. 6 shows remnant magnetisation (x100) measurements vs. temperature for the Li doped samples.**

Rather than increase the ability of  $ZnV_2O_4$  to sustain remnant magnetisation, the lithium induced electronic disorder has quite the opposite effect. Disorder should increase the stability of local clusters, not decrease their stability, thus one would expect to see a continual increase in the remnant magnetisation with increasing lithium content. At very low doping levels,  $Li = 0.010$  to  $0.025$  some increase is observed, but by  $Li = 0.050$  this effect is reversed. It is as if something is being slightly stabilised by low lithium doping levels but the change over between  $Li = 0.0250$  and  $0.050$  makes simple antiferromagnetic clusters an unlikely candidate. This

observation runs counter to the assertion that cluster ordering is responsible for the divergence in field and zero field cooled susceptibilities in the parent  $\text{ZnV}_2\text{O}_4$ .

Similar data sets collected on the gallium-doped samples show broadly the same type of effect as lithium doping. Figure 11.7 below shows the zero field cooled susceptibilities.

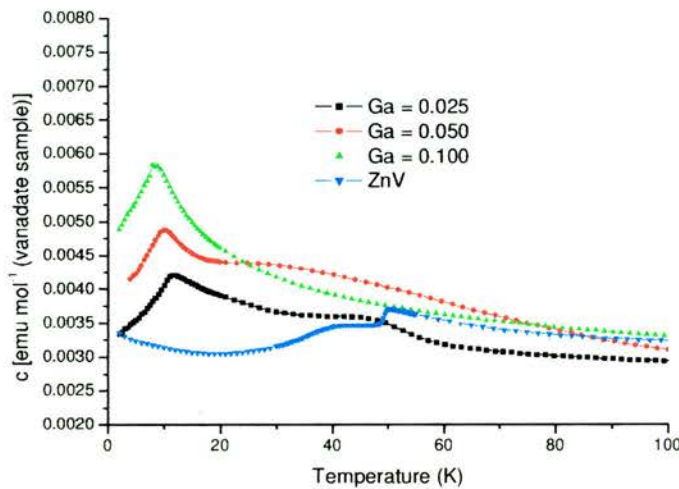


**Figure 11. 7 Shows magnetic susceptibility plots for Ga = 0.025, 0.050 and 0.100 samples.**

The  $\text{ZnV}_{0.975}\text{Ga}_{0.025}\text{O}_4$  sample shows a broadened feature at just below 50K corresponding to the structural transition in the parent material. By  $\text{Ga} = 0.050$ , there is possibly a hint of this in the curvature of the susceptibility at around 32K, but by  $\text{Ga} = 0.100$  it is completely suppressed. Knowing from neutron scattering experiments (section 11.4) that no long range collinear order is found in the  $\text{Ga} = 0.025$  sample, it seems reasonable to presume that all three are showing spin or cluster-glass behaviour. This presumption is then reinforced by the observation that the lower temperature behaviour of all three is markedly different from the parent phase, taking the form of the lithium-doped glass phases. However it is seen that this sharp maximum in susceptibility occurs even in the lowest gallium doped sample

investigated. The individual susceptibility plots for the gallium-doped samples are shown below. As expected, the gallium concentration appears to have a more rapid effect on the parent material's properties than that of lithium.

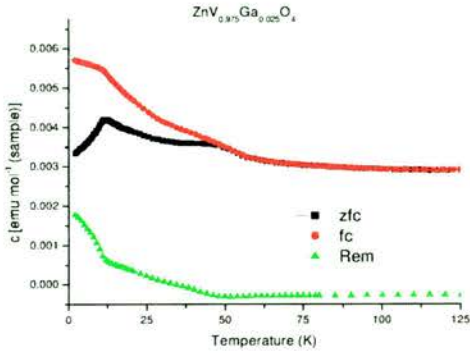


Figure 11. 8 shows the field cooled, zero field cooled and remnant magnetisation data for the  $\text{ZnV}_{0.975}\text{Ga}_{0.025}\text{O}_4$  sample.

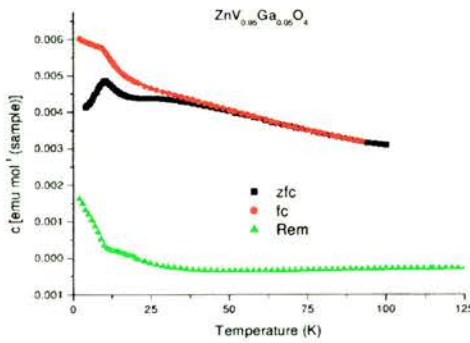


Figure 11. 9 shows the field cooled, zero field cooled and remnant magnetisation data for the  $\text{ZnV}_{0.950}\text{Ga}_{0.050}\text{O}_4$  sample.

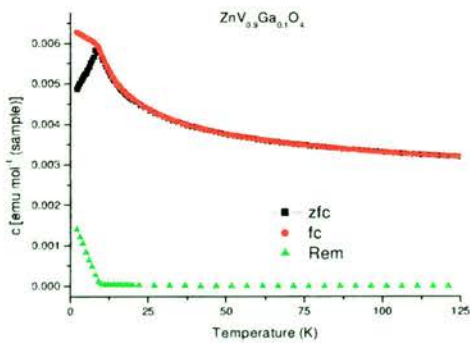


Figure 11. 10 shows the field cooled, zero field cooled and remnant magnetisation data for the  $\text{ZnV}_{0.900}\text{Ga}_{0.100}\text{O}_4$  sample.

It is evident from the above plots is that divergence between field and zero field cooled susceptibilities moves immediately towards the temperature where the

structural distortion was found in the parent spinel, before moving rapidly towards the maximum in susceptibility which we believe to be the glass temperature. This suggests that the residual effects of the parent material's structural distortion are necessary to stabilise clusters in the doped samples above their respective glass temperatures. Once the residual effect is lost, by  $Ga = 0.1$ , this is no longer possible. This observation offers additional strength to the argument that cluster ordering is only possible in the parent  $ZnV_2O_4$  below the structural distortion temperature and reinforces our questioning of the cluster-like ordering argument to explain the divergence in the field and zero field susceptibilities at c.100K in the parent.

## 11.4 Neutron Scattering

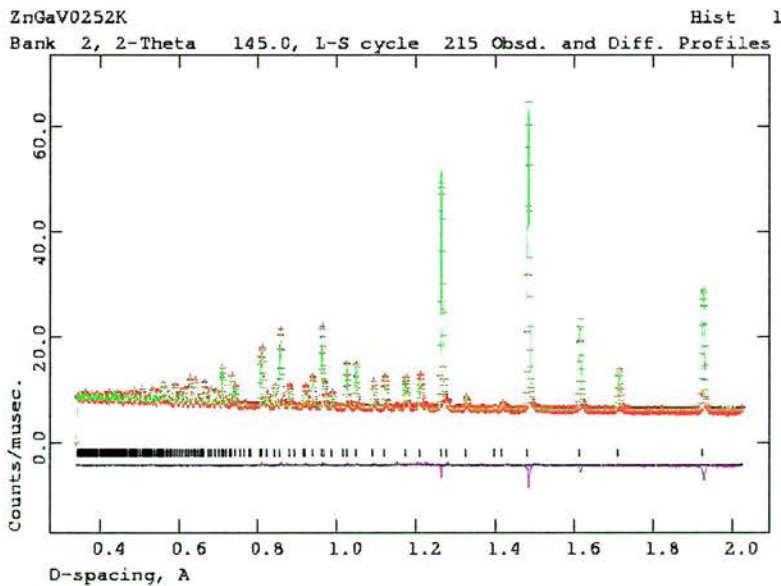
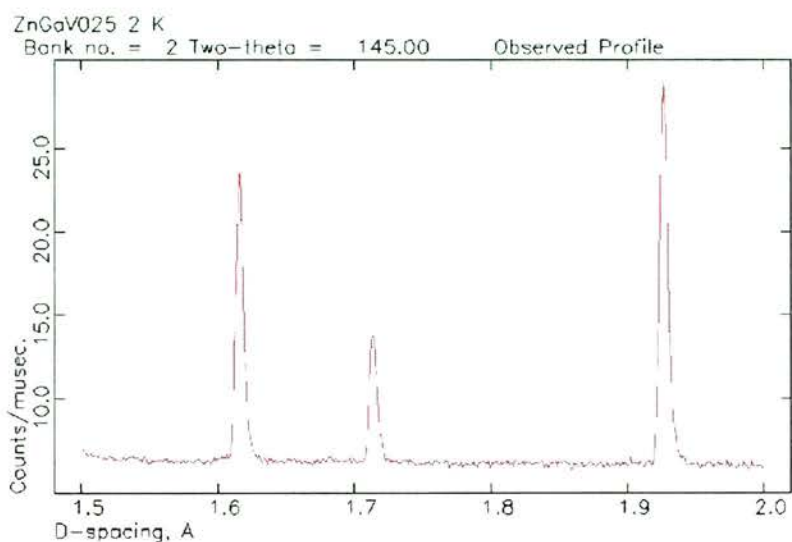


Figure 11. 11 shows a refinement of neutron data collected on the  $Ga = 0.025$  sample at c. 2K

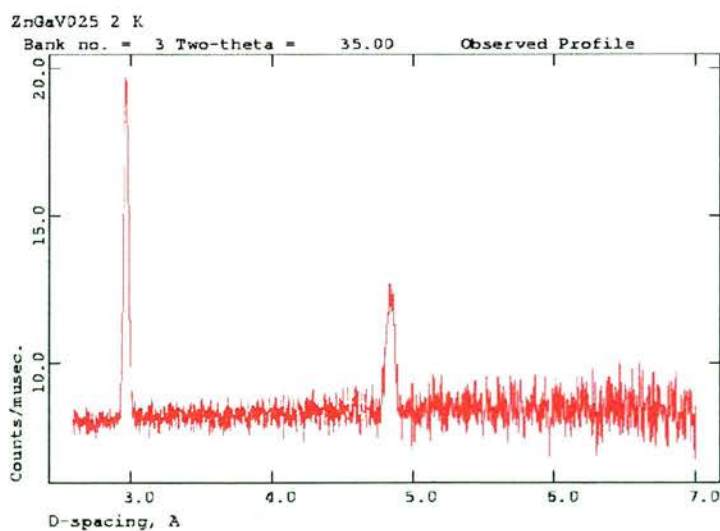
The  $ZnV_{1.95}Ga_{0.05}O_4$  and  $ZnV_{1.975}Ga_{0.025}O_4$  samples were used in low temperature neutron scattering studies to look for evidence of the structural distortion and ordered magnetic phase found in the parent  $ZnV_2O_4$ . These experiments found no evidence of either the tetragonal structural distortion or of long range magnetic order.

Figure 11.11 above shows the plot of a refinement of Polaris neutron data collected on the Ga = 0.025 sample at 2K. This data was easily fitted to the cubic spinel structure as were the datasets from the Ga = 0.05 and 0.1 samples. No evidence of peak splitting was observed to suggest the structural distortion was present.



**Figure 11.13 shows an expanded view of neutron data collected from the Ga = 0.025 sample at 2K. All three peaks would have been expected to split were the tetragonal distortion present.**

Magnetically, at longer d-spacings, there was no sign of any magnetic Bragg peaks as shown in figure 11.13 below. Thus we conclude no long range ordering is present.



**Figure 11.12 shows neutron data collected from the Ga = 0.025 sample at 2K, no evidence is seen of the magnetic Bragg peaks at c.3.7Å and c.5.95Å as found in the parent ZnV<sub>2</sub>O<sub>4</sub>.**

Similarly, the samples containing more gallium show signs of neither the distortion or of magnetic Bragg peaks.

The  $\text{Li}_{0.025}\text{Zn}_{0.975}\text{V}_2\text{O}_4$  sample does however show a structural distortion as per the parent zinc vanadate spinel occurring somewhere between 30K and 35K:

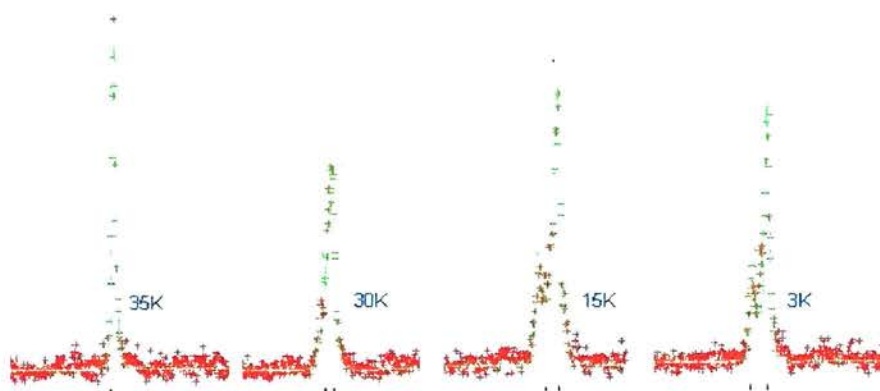


**Figure 11. 14** shows the evolution of the (4,0,0) cubic peak into the (0,0,4) and (2,2,0) tetragonal peaks in the  $\text{Li} = 0.025$  sample with decreasing temperature, (temperatures as marked on figure, y-scaling arbitrary). (HRPD data).

Lattice parameters extracted from fitting data collected at 35K, 30K, 15K and 3K are given in the table below:

Temperature	Lattice Parameter "a" (Angstroms)	Lattice Parameter "c" (Angstroms)	Cell Volume (Angstroms <sup>3</sup> )
35K*	5.93571*	8.39436(4)	295.7555*
30K	5.94127(5)	8.38041(13)	295.818(6)
15K	5.94370(6)	8.37367(12)	295.822(6)
3K	5.94380(5)	8.37323(11)	295.816(5)

**Table 11. 5** gives lattice parameter and cell volume figures extracted from refinements of  $\text{Li}_{0.025}\text{Zn}_{0.975}\text{V}_2\text{O}_4$  HRPD neutron data. \*35K cubic data given in tetragonal equivalents.

Comparing the parent and doped samples in table 11.5, (expressing all dimensions in their “a” tetragonal equivalents ( $\times 1/\sqrt{2}$ ), we note that the distortion of the cell is smaller in the doped sample, the  $c/a$  ratio for the latter being closer to unity. This is also seen visually comparing the peak splitting data shown above in figure 11.14 to the same peak shown in figure 9.5 for the parent material.

Sample	Lattice parameter $a$ (Å)	Lattice parameter $c$ ( $a$ equivalent, Å)	$c / a$ ratio
ZnV <sub>2</sub> O <sub>4</sub> (4K)	5.952045(18)	5.91837(3)	0.9943
Li <sub>0.025</sub> Zn <sub>0.975</sub> V <sub>2</sub> O <sub>4</sub> (3K)	5.94380(5)	5.92077(8)	0.9961

**Table 11. 6 compares the distortions in the parent and Li = 0.025 vanadate spinels.**

Referring back to the magnetisation data in figure 11.14, it is hard to make out any sign of this slight structural transition in that data between 35K and 30K, a change in magnetisation behaviour is observed closer to 50K however. This is intriguing. It is however possible that clusters of distorted material are beginning to form closer to 50K and that the size of these clusters is insufficient to be seen by diffraction until they have grown somewhat with decreasing temperature.

## 11.5 $\mu$ SR doped samples

From Ueda’s published magnetic compositional diagram for the Li<sub>x</sub>Zn<sub>(1-x)</sub>V<sub>2</sub>O<sub>4</sub> series, it was thought that the 15% Zn doped sample would show clearly a spin-glass transition. The 5% Zn doped sample was not expected to show a spin glass transition, and the 10% doped sample we were unsure about. This data set was modelled to a stretched exponential function thought to be suitable for characterising spin-glass systems. The fitting in this case was overseen by Hillier (ISIS) & Stewart (ILL). A transition between the paramagnetic and glassy states would be characterised by a

divergence in Lambda and in marked reductions in the observed Initial Asymmetry and Beta parameters. There is no real physical reduction in the Initial Asymmetry value, this would be illogical, the apparent change reflects an extremely rapid depolarisation occurring too quickly for the instrumentation to register the true initial asymmetry.

The 15% Zn doped sample was examined first. A sharp transition was observed in this sample at 7-8K. Plots of the zero field cooled data obtained for this material are shown below.

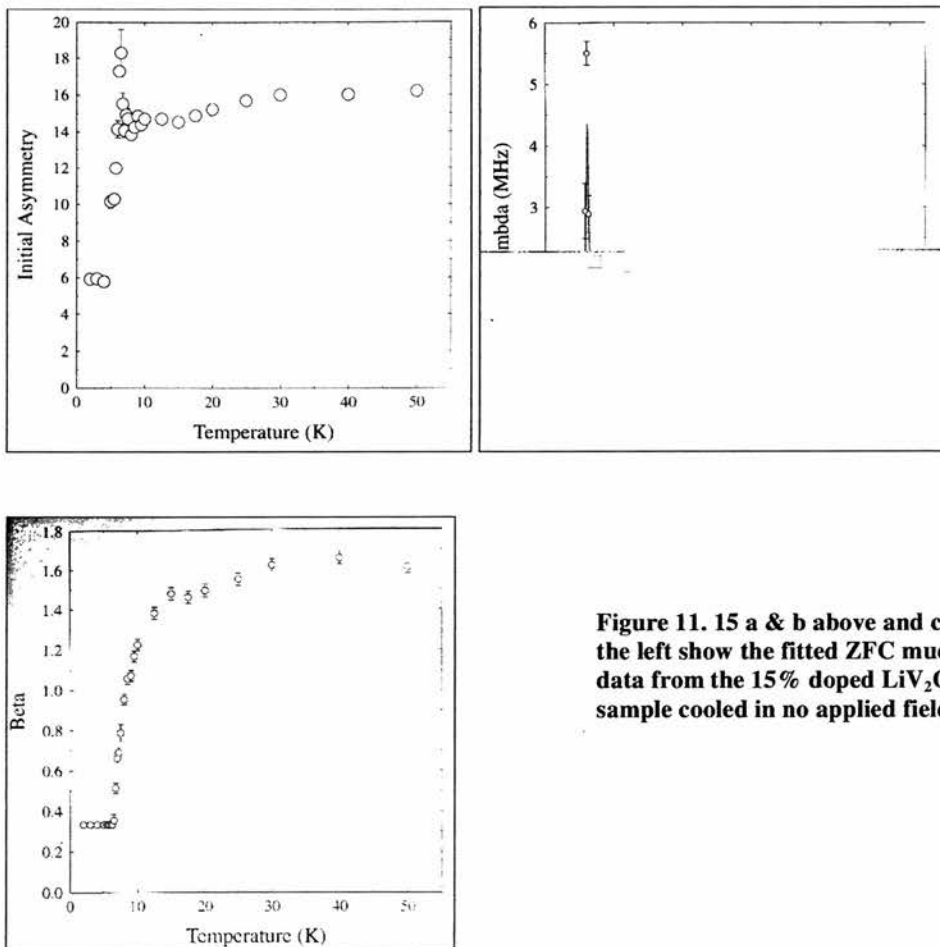


**Figure 11.15 a & b above and c to the left show the fitted ZFC muon data from the 15% doped  $\text{LiV}_2\text{O}_4$  sample cooled in no applied field.**

Given such a sharp transition, it was decided to fully characterise this magnetic behaviour, running the sample over the relevant range of temperatures under a

number of field cooling conditions, viz., 100, 300, 1 000 and 3 000 gauss. The observed data from the 1 000 gauss runs are given in the diagrams below.

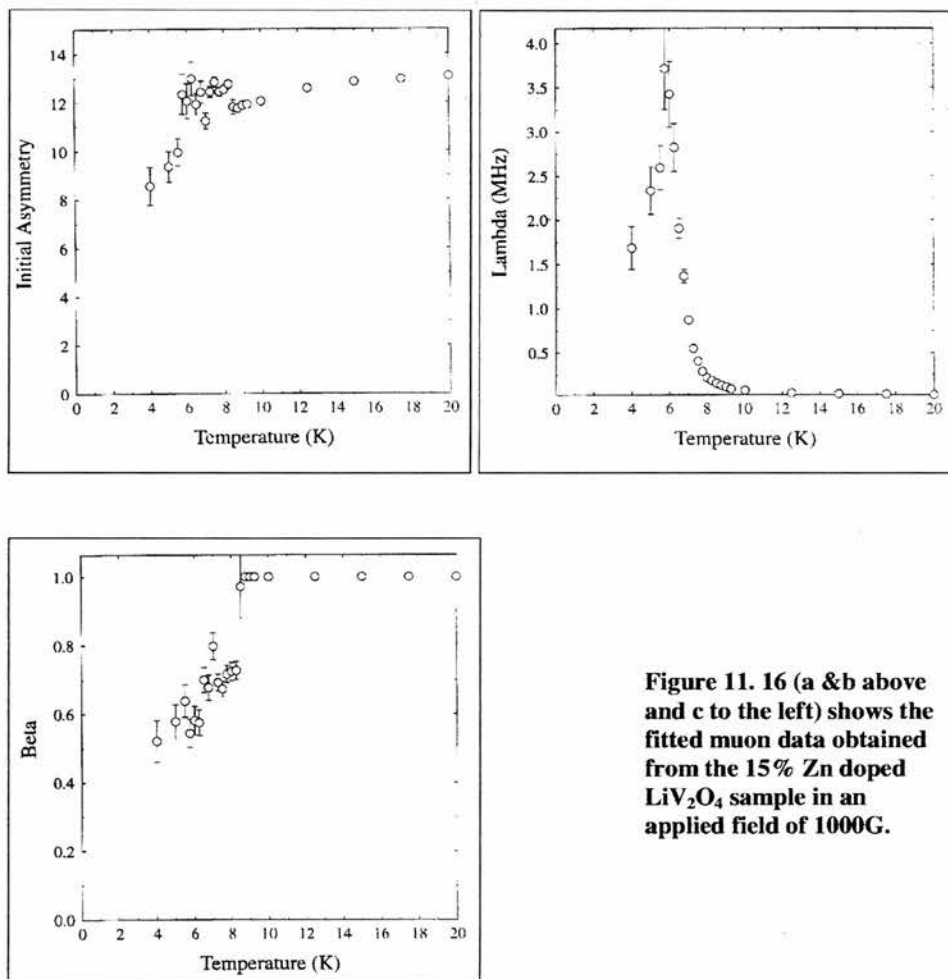


**Figure 11. 16 (a &b above and c to the left) shows the fitted muon data obtained from the 15% Zn doped  $\text{LiV}_2\text{O}_4$  sample in an applied field of 1000G.**

As can be seen, the change in  $\lambda$  is very sharp, indicating the rapid nature of the transition from the spin dynamic to glass state.  $\beta$  fell to a value below that expected – this has not yet been explained.

Comparison of the zero field cooled and 1 000 gauss runs show the field dependency of the behaviour, the spin glass transition temperature being depressed by the applied field, as might be expected. At 1 000 gauss, the transition is about a degree lower, 6-7K, than the zero field cooled measurement. The other field runs show the spin glass transition temperature being depressed in the same fashion by a magnitude of the

field applied.

The 5% doped sample was examined next. Despite expecting to find no transition, one was discovered presently. As previously, a set of zero and field cooled runs were carried out.

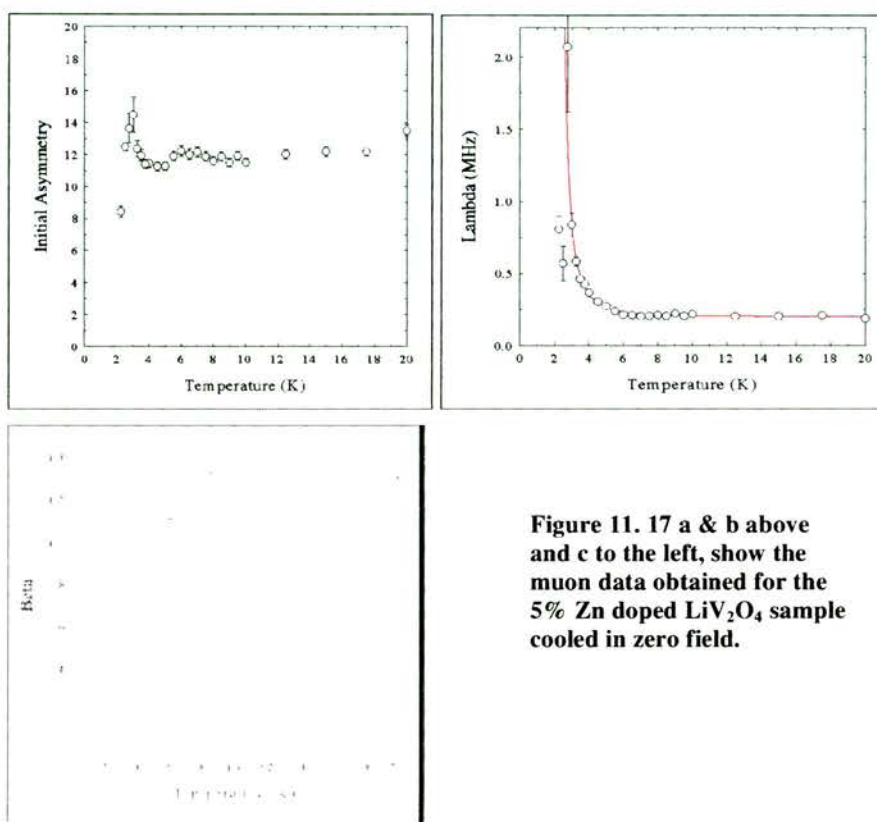


**Figure 11.17 a & b above and c to the left, show the muon data obtained for the 5% Zn doped  $\text{LiV}_2\text{O}_4$  sample cooled in zero field.**

As can be seen in the graphs above, the transition is seen to exhibit a similar sharpness to that of the 15% doped sample. A similar field dependency is observed in this sample as shown for the 15% sample. The zero field cooled transition temperature is in this case around 3-4K. At the time of the experiment the transition has not been observed in magnetic susceptibility measurements.

Contemporary with collecting the MuSR data on the parent  $\text{ZnV}_2\text{O}_4$  spinel, similar data was collected for a sample of composition  $\text{Li}_{0.025}\text{Zn}_{0.975}\text{V}_2\text{O}_4$ . Fitting this data posed more extreme problems than those noted for  $\text{ZnV}_2\text{O}_4$ , arising from the lack of a suitable model. As per the  $\text{ZnV}_2\text{O}_4$  data however, the Initial Asymmetry was fixed to the value obtained from the highest temperature data set, the baseline value from the

lowest temperature data set. It was then attempted to fit changes in this data using a single Lorentzian decay function whilst holding all other parameters constant. This approach failed visually within a few data sets. This approach had to be abandoned and the data fitted to a stretched exponential function – however retaining the logically fixed Initial Asymmetry and baseline parameters.

Lambda shows a sharp divergence at c.24K, not dissimilar to those found for other samples, suggesting a transition. Similarly, Beta shows a marked reduction at the same temperature. Lambda and Beta clearly indicating a transition.

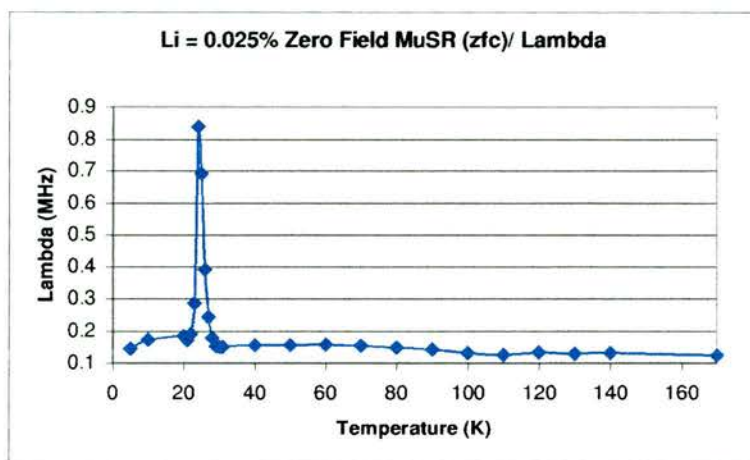


Figure 11. 18 shows Lambda for the zero field MuSR (zfc) data collected on the Li = 0.025% sample.

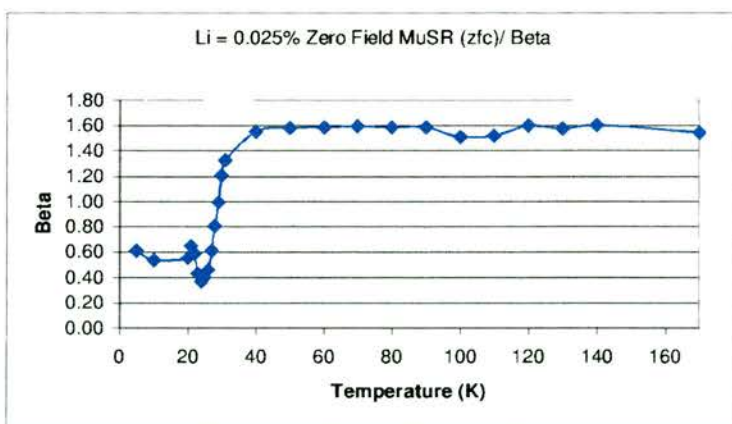
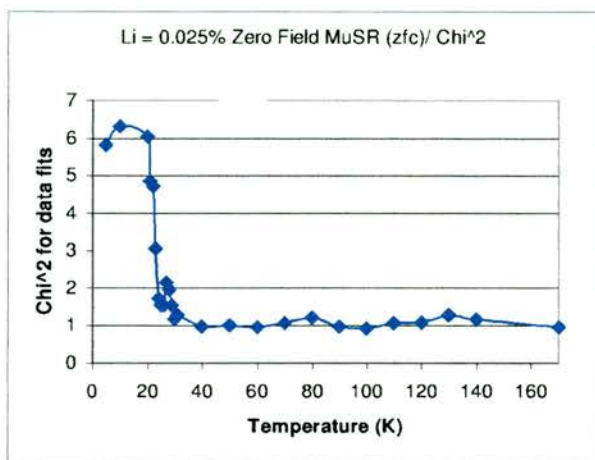


Figure 11. 19 shows Beta for the zero field MuSR (zfc) data collected on the Li = 0.025% sample.

The model used for the samples discussed previous to this allowed the initial asymmetry parameter to vary, these fits do not, so the data is not directly comparable. Below the transition temperature, even this function develops difficulties in modelling the data. This is illustrated in the plot of  $\chi^2$  for the data fits shown below. One can

only conclude that neither the stretched exponential function with fixed initial and baseline asymmetry, nor the single Lorentzian decay function, adequately describe the relaxation behaviour below the transition temperature.



**Figure 11. 20 shows  $\chi^2$  for the fits of the zero field MuSR (zfc) data collected on the Li = 0.025% sample.**

Raw data is shown below in figure 11.21 to emphasise something unseen in the fitted data. From 31K to 25K each data set gets lower than its predecessor, for some reason, the 23K data set is higher than that at 25K, and 21K higher yet again. The reason for this reverse is completely unclear, this is raw experimental data and the observation is independent of subject models etc.. This feature was masked in the plot of *fitted* data by very poor fit quality in this region.

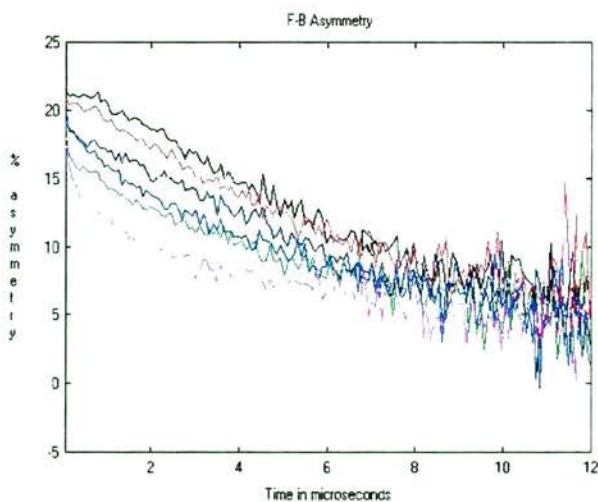


**Figure 11. 21 shows raw zero field MuSR (zfc) data collected on the Li = 0.025% sample.**

**Black = 31K,**

**Red = 29K,**

**Blue = 27K,**

**Magenta = 25K**

**Green = 23K**

An equivalent data set collected in an applied measuring field of 30G is shown in figure 11.22 below.

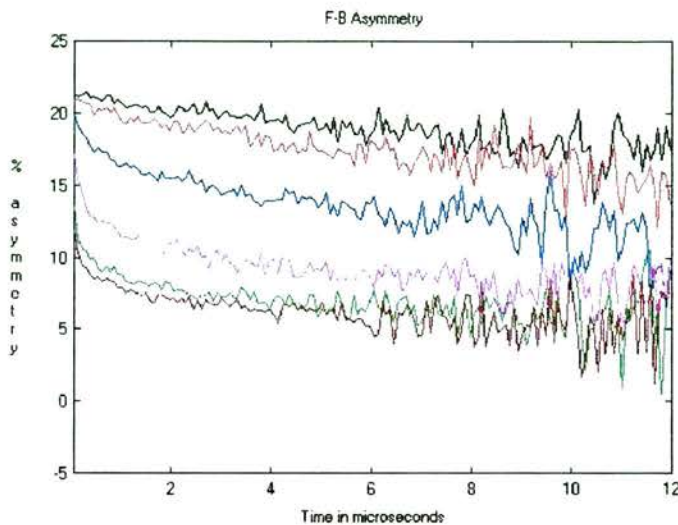


**Figure 11. 22 shows raw MuSR (zfc) data collected in an applied field of 30G for the Li = 0.025% sample.**

**Black = 31K,**

**Red = 29K,**

**Blue = 27K,**

**Magenta = 25K**

Here, this reversal is not seen, suggesting that the Li = 0.025 doped sample is extremely sensitive to applied fields, as per the parent material. Again however, one can only speculate as to what might be happening in the sample to cause these observations, the term anomalous seems very apt.

The nature of this transition in the Li = 0.025 sample is very interesting. Structural disorder could pin regions of antiferromagnetic clusters leading, with decreasing temperature, to long range order (broken to a certain degree by the extent of the structural disorder - contrasting with the parent  $\text{ZnV}_2\text{O}_4$ ), or it could enhance more of a spin glass like magnetic state. Returning momentarily to the magnetisation measurements shown in figures 11.5 and 11.6 we note that those measurements are more reminiscent in form of the parent  $\text{ZnV}_2\text{O}_4$  material than of those with lithium content greater than 0.05.

## **12 Zinc vanadate spinel: Conclusions**

Much data has been presented in this chapter. Without repeating arguments already made in detail, we would contend that there is evidence that  $\text{ZnV}_2\text{O}_4$  is not the *simple* antiferromagnet it was previously believed to be.

Reference to the literature suggests that the octahedral V(III) cation is not only unstable with respect to Jahn-Teller effects but is also likely to exhibit spin-orbit coupling effects, the two phenomena being likely to compete with each other. The  $c < a$  deformation of the octahedra is not expected to entirely quench spin-orbit coupling; however this coupling offers the potential of an additional stabilising energy to compliment the  $c < a$  Jahn-Teller orbital ordering. The total stabilisation of both these features may exceed that of the  $c > a$  Jahn-Teller orbital ordering stabilisation only.

Above the deformation temperature, the octahedral V(III) cation has potential to exhibit dynamic Jahn-Teller effects. Given that competition is predicted between the Jahn-Teller instability and spin-orbit coupling and the dynamics of a frustrated spin system, the formation of a dynamic resonance state reflecting the possible structural arrangements would not be surprising. Experimental evidence is inconclusive, however the  $\text{ZnV}_2\text{O}_4$  lattice parameter and related data are found to behave in an unexpected manner and are not inconsistent with some sort of unusual dynamics being present. It is difficult to account for this data without something akin to a dynamic Jahn-Teller effect being present. Other literature claims the existence of an orbital liquid state in the undistorted V(III) cation – this state can be equated to a dynamic Jahn-Teller effect wherein orbital ordering is frustrated by  $k_B T$  which

exceeds the inter-conversion energy barrier between different structural states.

The pattern of behaviour of remnant magnetisation in the lithium and gallium doped zinc vanadates implies that the peculiar remnant magnetism and divergence between field and zero-field cooled measurements seen in  $\text{ZnV}_2\text{O}_4$  is a property of that parent zinc vanadate; that it appears to be unrelated to defect induced clustering of uncompensated antiferromagnetic regions. Both lithium and gallium doped materials show a rapid suppression of the tetragonal distortion, emphasising the sensitive nature of the cooperative orbital ordering involved in said deformation.

Muon data contradicts the idea that antiferromagnetic clusters are developing in the 100K-51K temperature region, no significant slowing in spin fluctuations is observed until the Néel temperature at c.39K. Spin ordering is not likely anyway given that geometric frustration is maximal in this cubic form. The nature of the time independent remnant magnetisation in this temperature regime is unclear. A statistical orbital ordering of some sort dragging an element of spin moment via an element of spin-orbit coupling might be one idea; spin dynamics continue more or less as per the paramagnetic state, but within the framework of a “sticky” orbital ordering, possibly a slight energy barrier between two states.

Muon and neutron scattering confirm a Néel temperature of 39K, long range magnetic order is undoubtedly present. Small differences observed between field and zero field-cooled neutron patterns suggest the possibility of sticky component of the magnetic moment which can be influenced by an applied field – the zero field-cooled magnetic Bragg peaks seem to be unaffected by this small applied field. These observations plus those from the M/H sweeps and cooling the  $\text{ZnV}_2\text{O}_4$  sample in different applied field strengths, leads to the conclusion that more than one magnetic

component is present. One of which is the Néel type order, the other a glassy component. Diffuse scattering suggests that there may be some tendency for this glassy component to order at the lowest temperatures.

One interesting conjecture concerns the tetragonal form retaining spin-orbit coupling for one of its electrons (the other is in a singlet state). The idea being that an applied field may serve to induce additional orbital ordering into that degenerate electron as the material is cooled; e.g. the field deciding which of the degenerate orbitals that electron will reside in. The slow decay of the remnant magnetisation and M/H sweeps implying that this additional magnetisation is very weakly bound and very sensitive to applied fields.

One could speculate endlessly, however only further experimentation will confirm these or other ideas. One hopes, however, that the case is successfully made that  $\text{ZnV}_2\text{O}_4$  is not a simple antiferromagnet!

---

## References

- <sup>1</sup> K. Range & C. Eglmeier, JALCE 176, 1991, P. L13-16.
- <sup>2</sup> F.F. Weill et al., Eur. J. Solid State Inorg. Chem. t. 30, 1993, p. 1095-1108.
- <sup>3</sup> N. W. Grimes, "The Spinels: Versatile Materials," Phys. Technol., 6, 22-7 (1977).
- <sup>4</sup> J.B. Goodenough Magnetism and the chemical bond, Wiley, 1963, Tables XV, XVI ff.
- <sup>5</sup> Biographical encyclopedia of scientists, 2<sup>nd</sup> Edn, IOP, 1994, P816.
- <sup>6</sup> Wickham *et al.*, Solid state quarterly report, MIT, Mass. US., Jan 1960.
- <sup>7</sup> D. Rogers, Solid state quarterly report, MIT, Mass. US., July 1961.
- <sup>8</sup> K. Matsuno, T. Katsufuji, S. Mori, et al., J Phys Soc JPN 70 (6): 1456-1459, 2001.
- <sup>9</sup> S. Kondo, D.C. Johnston, C.A. Swenson, et al., Phys Rev Lett 78 (19): 3729-3732, 1997.
- <sup>10</sup> B. Reuter, Naturwissenschaften, 54, 164, 1967.
- <sup>11</sup> S. Niziol, Phys Stat Solidi A, 18, K11, 1973.
- <sup>12</sup> S.J. Blundell, Magnetism in condensed matter, OUP, 2001, P95-96.
- <sup>13</sup> S.J. Blundell, Magnetism in condensed matter, OUP, 2001, P178-179.
- <sup>14</sup> Y. Ueda, N. Fujiwara & H. Yasuoka, J Phys Soc JPN 66 (3): 778-783, 1997.
- <sup>15</sup> Y. Yamashita & K. Ueda, Phys Rev Lett 85 (23): 4960-4963, 2000.
- <sup>16</sup> O. Chmaissem, J.D. Jorgensen, S. Kondo, D.C. Johnston, Phys. Rev. Lett, 79, 4866, 1997.
- <sup>17</sup> Our own data consistent with 6, 7 & 8.
- <sup>18</sup> J.B. Goodenough, Private communication, 2002.

- 
- <sup>19</sup> A.S. Wills and A.Harrison, *J.Chem.Soc., Faraday Trans.*, 92, 2161, 1996.
- <sup>20</sup> A.R. Armstrong & P.G. Bruce, *Nature*, 381, 499-500, 1996.
- <sup>21</sup> Y. Ueda, N. Fujiwara & H. Yasuoka, *J Phys Soc JPN* 66 (3): 778-783, 1997.
- <sup>22</sup> V. Massarotti et al., *J. App. Cryst*, 32: 1186-1189, Part 6, 1999.
- <sup>23</sup> B.N. Figgis, *Introduction to Ligand Fields*, Wiley, 1966.
- <sup>24</sup> J. Burdett, *Chemical Bonding in Solids*, 1<sup>st</sup> Edn., OUP, 1995, p246.
- <sup>25</sup> *Introduction to ligand field theory*, C.J. Ballhausen, New York : McGraw-Hill, 1962.
- <sup>26</sup> B.N. Figgis, *Introduction to Ligand Fields*, Wiley, 1966.
- <sup>27</sup> B.N. Figgis, *Introduction to Ligand Fields*, Wiley, 1966.
- <sup>28</sup> *Introduction to ligand field theory*, C.J. Ballhausen, New York : McGraw-Hill, 1962.
- <sup>29</sup> J.K. Burdett, G.J. Miller, J.W. Richardson, J.V. Smith, *J. Am. Chem. Soc.*, (1988).
- <sup>30</sup> C. Ulrich et al., *Phys. Rev. Let.* 9125(25):7202, 2003
- <sup>31</sup> B.N. Figgis, *Introduction to Ligand Fields*, Wiley, 1966, P213.
- <sup>32</sup> J.B. Goodenough, *Magnetism and the chemical bond*, Wiley, 1963.
- <sup>33</sup> J.B. Goodenough, *Magnetism and the chemical bond*, Wiley, 1963, P64.
- <sup>34</sup> M. Hervieu, A. Maignan, et al., *Phys. Rev. B* 67, 045112 (2003)
- <sup>35</sup> H.C Nguyen & J.B. Goodenough, *PRB* 52 324, 1995.
- <sup>36</sup> as 28
- <sup>37</sup> Feynman, Leighton, Sands, *Feynman Lectures on Physics*, Addison Wesley, 1965, Vol 2, Ch1.
- <sup>38</sup> J.B. Goodenough, *Magnetism and the chemical bond*, Wiley, 1963.
- <sup>39</sup> *Biographical Encyclopedia of scientists*, IOP Publishing, Bristol, 1994, P207.
- <sup>40</sup> M. Woolfson, *An introduction to x-ray crystallography*, Cambridge, 2<sup>nd</sup> Edn., 1997, P67.
- <sup>41</sup> Complex numbers, showing link between algebraic functions and geometry - Feynman Leighton Sands, *Feynman lectures on physics*, Addison Wesley, 1965, Vol I 22-7ff.
- <sup>42</sup> C. Kittel, *Introduction to solid state physics*, Wiley, 7<sup>th</sup> Edn., 1996, P34.
- <sup>43</sup> M. Woolfson, *An introduction to x-ray crystallography*, Cambridge, 2<sup>nd</sup> Edn., 1997, P72.
- <sup>44</sup> Kittel, *Introduction to solid state physics*, Wiley, 7<sup>th</sup> Edn., 1996, P34.
- <sup>45</sup> <http://www.ncnr.nist.gov/resources/n-lengths/>
- <sup>46</sup> Equations from M. Woolfson, *An introduction to x-ray crystallography*, Cambridge, 2<sup>nd</sup> Edn., 1997, P175ff.
- <sup>47</sup> GSAS Manual, A.C. Larson and R.B. Von Dreele, "General Structure Analysis System (GSAS)", Los Alamos National Laboratory Report LAUR 86-748 (2000).
- <sup>48</sup> ISIS Neutron Training Course general notes, ISIS, RAL, 2001.
- <sup>49</sup> M. Woolfson, *An introduction to x-ray crystallography*, Cambridge, 2<sup>nd</sup> Edn., 1997, P151.
- <sup>50</sup> Laue Instrument web page at ILL
- <sup>51</sup> M. Woolfson, *An introduction to x-ray crystallography*, Cambridge, 2<sup>nd</sup> Edn., 1997, P149.
- <sup>52</sup> ISIS Neutron Training Course, general notes, ISIS, RAL, 2001.
- <sup>53</sup> R. Cywinski, *Lecture Notes from course given on Structure and Dynamics of Solids*, School of Physics, St. Andrews, 2000.
- <sup>54</sup> ISIS Neutron Training Course, general notes, ISIS, RAL, 2001.
- <sup>55</sup> See instrument D7 web pages at [www.ill.fr](http://www.ill.fr).
- <sup>56</sup> MPMS user's manual, Quantum Design, San Diego, USA, 2000.
- <sup>57</sup> Squid diagram ~ with kind permission of Rod Nave, Georgia State University from <http://hyperphysics.phy-astr.gsu.edu/hbase/hframe.html>.
- <sup>58</sup> Lecture notes, Superconducting Electronics (applications), Mark Colclough (Univ. Birmingham), IRC in Superconductivity Winter School, Cambridge, 2000.
- <sup>59</sup> Kilcoyne & Eaton *Muon Science*, Eds, S.L.Lee, S.H. Kilcoyne, R.Cywinski, SUSSP/IOP, UK, 1999, P11.
- <sup>60</sup> S. Kilcoyne & G.H. Eaton, from *Muon Science*, Eds, S.L.Lee, S.H. Kilcoyne, R.Cywinski, SUSSP/IOP, UK, 1999, Chapter 1.
- <sup>61</sup> Figure from ISIS Muon Group web site ~ [www.isis.rl.ac.uk](http://www.isis.rl.ac.uk)
- <sup>62</sup> Picture from the ISIS Muon Group / Riken web sites at [www.isis.rl.ac.uk](http://www.isis.rl.ac.uk)
- <sup>63</sup> G.H. Eaton, RAL technical report RAL-TR-1998-019, 1998, CLRC P10.
- <sup>64</sup> Y.J. Uemura, from *Muon Science*, Eds, S.L.Lee, S.H. Kilcoyne, R.Cywinski, SUSSP/IOP, UK, 1999, P85-86.
- <sup>65</sup> Private discussions with S. Blundell, Clarendon, Oxford, 2002.

- <sup>66</sup> Y.J. Uemura *et al.*, PRB 31, 1985, P546.
- <sup>67</sup> I. Campbell, from Muons Science, Eds. Lee, Kilcoyne & Cywinski, SUSSP/IOP, 1999, P139.
- <sup>68</sup> Private discussion S. J. Blundell, Clarendon, Oxford, 2002.
- <sup>69</sup> F.L. Pratt, Physica B 289-290 (2000) 710
- <sup>70</sup> S. Blundell, Contemp Phys., **40**, 1999, P175.
- <sup>71</sup> Y. Ueda, N. Fujiwara and H. Yasuoka, *J. Phys. Soc. Japan* **66**, 778-783 (1997)
- <sup>72</sup> D8A Facility provided by J.S.O. Evans and R.G. Gover at Durham.
- <sup>73</sup> S. Kondo, D.C. Johnston, L. Miller, Phys. Rev B, 59, 2609-2626, 1999.
- <sup>74</sup> J. Rodríguez-Carvajal *et al.*, Phys. Rev. Lett. 81, 4660-4663, 1998.
- <sup>75</sup> Y. Yamashita and K. Ueda, *Phys. Rev. Lett.* **85**, 4960 (2000)
- <sup>76</sup> J.K. Burdett, Molecular Shapes, Wiley, 1980, Page 177.
- <sup>77</sup> B.N. Figgis, Introduction to Ligand Fields, Wiley, 1966, P213.
- <sup>78</sup> H.C. Nguyen & J.B. Goodenough, PRB **52** 324, 1995.
- <sup>79</sup> R.J.H. Clark, The Chemistry of Titanium and Vanadium, Elsevier, 1968, Page 181.
- <sup>80</sup> J.B. Goodenough, Magnetism and the chemical bond, Wiley, 1963, chapter 2.
- <sup>81</sup> Private communication, J.B. Goodenough, Austin, Texas, USA, 2004.
- <sup>82</sup> J.K. Burdett, Molecular Shapes, Wiley, 1980.
- <sup>83</sup> H.C. Nguyen & J.B. Goodenough, PRB **52** 324, 1995.
- <sup>84</sup> C. Ulrich *et al.*, Phys. Rev. Lett. 91, 7202, 2003.
- <sup>85</sup> J.K. Burdett, G.J. Miller, J.W. Richardson, J.V. Smith, J. Am. Chem. Soc., (1988).
- <sup>86</sup> J.B. Goodenough, private discussions 2002.
- <sup>87</sup> W. Rudorff & B. Reuter, Z. Anorg. Allgem., 253, 177, 1947.
- <sup>88</sup> Y. Ueda, N. Fujiwara and H. Yasuoka, *J. Phys. Soc. Japan* **66**, 778-783 (1997)
- <sup>89</sup> S. Niziol, *Phys. Stat. Sol. A* **18**, K11 – K13 (1973)
- <sup>90</sup> N. Büttgen *et al.*, *Physica B*, **312-313**, 703 – 705 (2002)
- <sup>91</sup> Y. Ueda, N. Fujiwara and H. Yasuoka, *J. Phys. Soc. Japan* **66**, 778-783 (1997)
- <sup>92</sup> Muhtar *et al.*, J. Phys Soc Japan, 56, 444, 1987.
- <sup>93</sup> W. Rudorff & B. Reuter, Z. Anorg. Allgem., 253, 177, 1947.
- <sup>94</sup> H. Mamiya & M. Onada, Solid State Com., 95, 217, 1995.
- <sup>95</sup> P.K. Baltzer *et al.*, Phys. Rev. Lett., 151, 367, 1966.
- <sup>96</sup> Ashcroft and Mermin, Solid state physics, International Edition 1976, Saunders College Pub., P648.
- <sup>97</sup> M.R. Harrison, P. Edwards & J.B. Goodenough, J. Solid State Chem., **54**, 136, 1984.
- <sup>98</sup> P.M. Lambert, M.R. Harrison & P.P. Edwards, J. Solid State Chem., **75**, 332, 1986.
- <sup>99</sup> H. Mamiya & M. Onada, Solid State Com., 95, 217, 1995.
- <sup>100</sup> J.B. Goodenough, Mat. Res. Bull., **5**, 621, 1970.
- <sup>101</sup> K. Kawakami, Y. Sakai & N. Tsuda, J. Phys. Soc Jpn., **55**, 3174, 1986.
- <sup>102</sup> H. Nguyen & J.B. Goodenough, Phys. Rev. B, **52**, 324, 1995.
- <sup>103</sup> A.F. Orchard, Magnetochemistry, Oxford, 2003, P159
- <sup>104</sup> as 103, P150
- <sup>105</sup> as 103, P168
- <sup>106</sup> as 103, P168
- <sup>107</sup> J.B. Goodenough, Private communication, July 2002.
- <sup>108</sup> H.C. Nguyen & J.B. Goodenough, Phys. Rev. B, **52**, 324, 1995.
- <sup>109</sup> Y. Ueda, N. Fujiwara and H. Yasuoka, *J. Phys. Soc. Japan* **66**, 778-783 (1997)
- <sup>110</sup> N. Büttgen *et al.*, *Physica B*, **312-313**, 703 – 705 (2002)
- <sup>111</sup> Dr. R. Stewart, Instrument Scientist D7 (diffuse scattering neutron instrument), ILL, France; Prof. A. Harrison, School of Chemistry, Edinburgh; Prof. S. Blundell, Clarendon, Oxford.
- <sup>112</sup> N. Büttgen *et al.*, *Physica B*, **312-313**, 703 – 705 (2002)
- <sup>113</sup> A. S. Wills, Phys. Rev. B 63, 064430 (2001)
- <sup>114</sup> J. Villain, Z. Phys. B 33 (1979) 31.
- <sup>115</sup> J. Sirker & G. Khaliullin, Phys. Rev. B 67, 100408 (2003).
- <sup>116</sup> J. Villain, Z. Phys. B 33 (1979) 31.
- <sup>117</sup> My own neutron data, showing magnetic Bragg peaks in ZnCr2O4 below 14K, this is also reported by Goodenough and others.
- <sup>118</sup> S. Kondo, DC Johnston, SA Swenson *et al.*, Phys. Rev. Lett., **78**, 3729, 1997.
- <sup>119</sup> J.B. Goodenough, Magnetism and the Chemical Bond, Wiley, 1963, P67.

---

<sup>120</sup> Y. Ueda, N. Fujiwara, H. Yasuoka, J. Phys. Soc. Jpn., **66**, 778, 1997.  
<sup>121</sup> as 120.  
<sup>122</sup> as 120.

Th 1839

-